ISBN 91-628-4941-7
LUNDFD6/(NFFL-7201)2001

Jet Production and Parton Dynamics in Deep Inelastic Scattering

Thesis submitted for the degree of
Doctor of Philosophy
by

Mattias Davidsson

LUND
UNIVERSITY

DEPARTMENT OF PHYSICS
LUND, 2001

ISBN 91-628-4941-7
LUNDFD6/(NFFL-7201)2001

Jet Production and Parton Dynamics in Deep Inelastic Scattering

Thesis submitted for the degree of
Doctor of Philosophy
by

Mattias Davidsson

LUND
UNIVERSITY

DEPARTMENT OF PHYSICS
LUND, 2001

Abstract

Hard QCD processes have been studied by measuring the di-jet event rate for deep inelastic scattering in the kinematic range $5<Q^2<100$ GeV^2 and $10^{-4}<x<10^{-2}$. The jets were reconstructed using the cone algorithm in the hadronic center-of-mass frame in which the transverse momentum of the jets were required to be greater than 5 GeV. The result of the investigation is that using Leading Order QCD calculations together with pure DGLAP parton showering we can not reproduce the relative rate of hard di-jet events in DIS. To accomplish this the transverse momentum ordering in the parton ladder has to be broken as can be achieved by the inclusion of a component which resolves the photon in the DGLAP picture, or by using the Color Dipole Model for the higher order QCD radiation.

To gain knowledge about the nature of the initial state QCD radiation we investigate the more exclusive properties of the transverse momentum ordering of the propagator gluon, as well as correlations between the emitted partons in the QCD cascade. Hints of the onset of a new type of parton dynamics are seen when selecting a subset of events containing a highly energetic jet in the forward region.

Acknowledgments

I would first like to thank my supervisors; Leif Jönsson and Hannes Jung, for their continuous and invaluable support, discussion, car rides, wine, and more during these four years!

Furthermore I would like to thank:

The people at the department in Lund for help, discussion, lunch, coffee/cake and all the other necessities for a department life. Martin (M.K), Oxana (Miss PAW), just to mention a few.

All the colleagues that I encountered at conferences, schools and elsewhere from the H1 and (do I dare say it?) ZEUS, as well as other collaborations.

The members of the H1 jet and flow groups, recently merged under the name "HaQ" (what was wrong with my suggestion "the flowing jetties"?), especially the PhD students that provided help and support with all those technicalities and got me started, Magnus Lindström, Jürgen Spiekermann, Marcus Wobisch, Roman Poeschl among others.

The people at the theory department in Lund. Especially Leif Lönnblad, Torbjörn Sjöstrand, Gösta Gustavsson and Bo Andersson, for valuable discussion.

All the people from AI in Lund and elsewhere for putting things into perspectives as well as for lots of fun.

To all the ones that at this late hour were forgotten, but that rightfully so, feel that they should have been mentioned.

Last but not least, all my friends and my family, for all the reasons in the world.

Contents

Preface

This thesis comprises my work during the last four years at the H1 experiment at DESY. The topic is the nature of matter and its interactions, especially focusing on the complicated inner structure of the proton.

After an introduction to the physics of Deep Inelastic Scattering and the H1 experiment, the thesis is divided into two parts. The first part covers the work included in the thesis written for my Phil. Licentiate degree, where studies of the relative rate of hard QCD processes were performed. The outcome of these studies was that, to understand the full features of the hadronic final state further studies have to be made on the nature of the higher order QCD processes.

The second part deals with the more exclusive nature of the underlying parton dynamics of the higher order QCD radiation leading to an increased rate of the hard QCD processes studied in part one of this thesis. Since the QCD radiation to all orders in DIS cannot be calculated exactly, different approximations can be made depending on assumptions about the size of higher order terms in the perturbative QCD expansion. These approximations are assumed to be valid in different regions of phase space, resulting in different kinds of parton dynamics. Since the exact borders between the different validity regions are not known, the aim is to identify the signature of the different kinds of parton dynamics by means of measuring correlations between, and properties of, the particles in the hadronic final state.

Chapter 1

Introduction

All matter consists of nucleons (protons and neutrons) and electrons. Much of the knowledge we have today about the structure of matter has been obtained from so called scattering experiments, similar to Rutherford's famous experiment which led to the discovery that the main part of the atomic mass was distinctly localized in a nucleus, with the electrons moving around it. The experiment was carried out in the beginning of the 20'th century, scattering alpha-particles against a thin golden foil. Scattering experiments at higher energies have been used to explore three of the fundamental forces of nature, the electromagnetic, the weak and the strong forces. The development has lead to the use of leptons as projectiles to probe the structure of nucleons. The advantage of using leptons is that they are, to our present knowledge, point-like, particles without structure, and that their interactions with other point like particles are well understood. The research at the H1 detector at HERA is based on the scattering of electrons against protons at high energies.

This thesis is concerned with the revelation of the proton content by the manifestation of its partons, the constituent particles, in so called *jets*. In the quark model, the proton consists of three *quarks*, particles that are so far considered to be point-like, and *gluons* binding them together. These quarks are called valence quarks and they describe the properties, or quantum numbers, of the proton. However, looking at the proton in more detail a more intricate and complex structure is revealed. The strong force acts between quarks since they carry color charge, which is the reason why the strong force might be called the color force. This means that the quarks and gluons interact strongly via the exchange of the strong color force carrier, the gluon. This is equivalent to the electromagnetic force which is mediated by photons exchanged between particles carrying electric charge. Just like the electric force is responsible for the formation of stable atoms, the color force is responsible for the formation of protons, neutrons and other more exotic particle-types of the hadron family. The gluons, themselves carrying color charge, can fluctuate into two gluons or pairs of quarks and anti-quarks, particles that in turn can radiate gluons. Hence the gluons binding the three

valence quarks together produce an intricate mix of quarks and gluons. The quarks produced through these quantum fluctuations are called sea-quarks. The processes of gluon splitting inside the proton are virtual, their extension in time (and space) are limited by the Heisenberg uncertainty principle:

$$\Delta E \cdot \Delta t \sim \frac{h}{2\pi} \tag{1.1}$$

If the proton is probed during this time interval, it is possible to obtain information on the sea-quark properties. Depending on to what accuracy the proton is probed, corresponding to the power of our magnifying glass, particles with different momenta can be probed. A higher resolution provides sensitivity to partons carrying a smaller fraction of the proton momentum. For example, a gluon splitting into a quark anti-quark pair will naturally carry a larger fraction of the proton momentum than either the quark or the anti-quark. The magnifying power of the HERA collider is given by the transferred squared momentum Q^2. At values of Q^2 lower than $\sim$10000 GeV^2 the electron scatters of the proton via the exchange of a photon, and only at higher values ($Q^2 \gtrsim m_{Z_0}^2$) the contribution from the Z_0 boson has to be taken into account. The spectrum of the parton fractional momentum measured at different resolutions is called the proton *structure function.*

What happens when the electron interacts with the proton by the exchange of a photon? Since the photon is the mediator of the electric force it can only interact with objects carrying electric charge, and thus the interaction always takes place with a quark. The gluons have to be probed via the decay into sea-quark pairs. The quark struck by the photon will gain transverse momentum changing its direction of motion with respect to the other partons in the proton. The color force field responsible for the confinement of quarks will stretch out like a rubber band, preventing the parton to escape the proton as a free particle. Recalling the famous relation between energy and matter:

$$E = mc^2$$

it is clear that the energy stored in the color field can be converted into matter. If the energy transferred by the photon is large enough, the force field might thus break at several points, the ends attaching to quarks and anti-quarks created from the virtual sea carrying the correct color charge. Since the quarks at the ends of the force field are moving apart, this is where most of the energy is stored, and thus the new particles produced will mainly follow the direction of the struck quark and the proton remnant. Most of the particles produced in the proton remnant direction will be lost in the beam-pipe of the detector, why the detector will observe mainly a collimated flow of particles from the initially struck quark forming a jet as seen in fig. 1.1. What is interesting is not merely that we are able to detect these particles by building large machines like the HERA accelerator and its detectors, but that

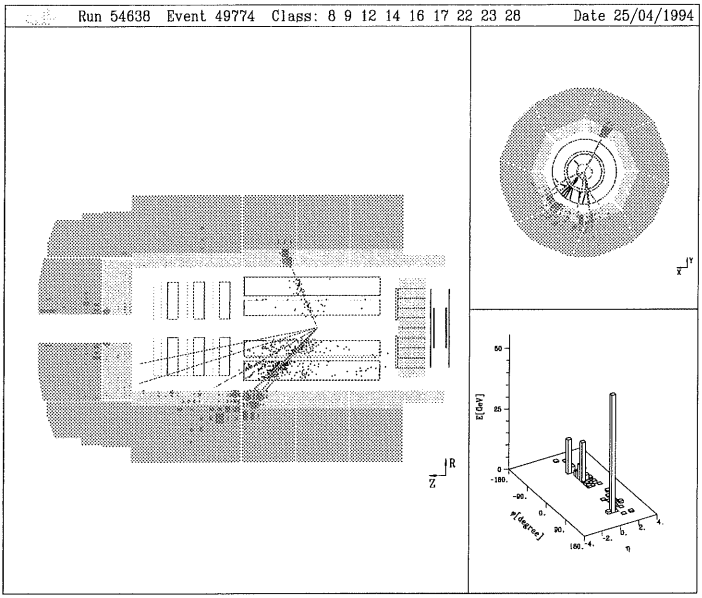

Figure 1.1: A deep inelastic scattering event as seen in a side view of the detector (left) and along the beam direction (upper right). A lego plot (lower right) shows the energy flow in (η, ϕ) space. The proton is split up, and the quark struck by the photon generates a collimated flow of particles, a *jet*, detected as seen in the picture. The electron is deflected and absorbed in the electromagnetic part of the barrel calorimeter.

we can actually describe, and to quite some extent, predict what happens theoretically by comparing data to models describing the dynamics of the proton, using the basic known facts of physics together with fast modern computers.

1.1 Analysis aim

Taking a step up in complexity this is where my analysis takes place. The process where the quark is struck by the photon is a purely electromagnetic interaction. However, if the struck quark radiates a gluon we have to introduce the strong force to describe the situation. This gluon will produce a force field that eventually breaks to form a second flow of collimated particles. A second jet can also be formed by the splitting of an incident gluon

into two quarks, one of which is struck by the photon.

The first main part of this thesis concerns the measurement of the relative rate of the above mentioned processes of 2-jet events at different resolutions, Q^2, and different fractional momentum, x_{Bj}, of the struck parton. To analyse the data with respect to these quantities we often use so called jet reconstruction algorithms. These are assumed to give an approximate picture of the underlying partonic processes. Several different jet algorithms exist, and we have felt the need to investigate the tool of investigation itself. We therefore performed an analysis of some of the most commonly used jet algorithms to check their performance in this aspect.

The second part deals with the question what is actually the type of dynamics that govern the higher order QCD radiation for different types of DIS events. The question is closely related to the question of validity for the different approximations assumed when calculating the higher order QCD cross-sections. In particular the expected onset of a new type of parton dynamics at very small values of fractional momentum is studied in terms of correlations and k_t ordering in the initial state QCD cascade.

Chapter 2

Theoretical Background

In the following chapter the different aspects of deep inelastic scattering of electrons on protons will be introduced. The relevant kinematics of the different processes will be described. The topic of jets will be introduced as well as the basics of event generation using Monte Carlo programs.

2.1 Deep Inelastic Scattering

At HERA two beams of electrons and protons collide with energies of 27.5 GeV and 920(820) GeV[1] respectively, producing a center of mass energy of roughly 300 GeV. Due to the much higher energy of the proton beam, the center of mass system is not at rest in the laboratory frame. If the invariant mass of the hadronic final state created in a collision is much larger than the mass of the proton, $W^2 \gg m_p^2$, the process is called inelastic scattering. If in addition, the wave-length of the probe ($\sim 1/Q$) is much smaller than the size of the proton, or equivalently if $Q^2 \gg m_p^2$, the process is called Deep Inelastic Scattering (DIS). This means that our probe (the photon) has a large resolution power so that we can look deep inside the the proton. The simplest of these reactions described by the Quark Parton Model (QPM) is schematically shown in fig. 2.3a. This is viewed in the laboratory frame where the electron and proton enter the collision from opposite directions. The direction of the incident proton is defined as the positive z direction according to H1 standards. The electron with four-momentum, p_e, is deflected by one of the quarks carrying four-momentum, p_q, inside the proton (P). The transverse momentum of the outgoing electron, carrying four-momentum, p_e', is balanced by the deflected quark, p_q'. The final state hadronic system is then built up by the fragmentation of the escaping quark and the proton remnant with four momentum, P_r, as will be described in section 2.3. Considering the above picture of a photon with four-momentum, q, all the kinematic variables in the event can be calculated from the measurement of two independent ob-

[1] In 1998 the proton energy was upgraded from 820 to 920 GeV

servables like the electron angle and energy (θ_e,E_e):

$$Q^2 \equiv -q^2 = -(p_e - p_e')^2 \approx 4E_e E_e' \cos^2(\theta_{e'}/2) \tag{2.1}$$

$$x_{Bj} \equiv \frac{Q^2}{2P \cdot q} \approx \frac{E_e E_e' \cos^2(\theta_{e'}/2)}{E_p(E_e - E_e' \sin^2(\theta_{e'}/2))} \tag{2.2}$$

$$y \equiv \frac{P \cdot q}{P \cdot p_e} \approx \frac{E_e - E_e' \sin^2(\theta_{e'}/2)}{E_e} \tag{2.3}$$

where Q^2 is the invariant mass (virtuality) of the exchanged photon, and also a measure of the momentum transferred by the photon. The variables x_{Bj} and y are the dimensionless Bjorken-variables both ranging from zero to one. The x_{Bj} variable can be seen as the energy fraction of the proton carried by the struck parton in the lowest order α_s process. In the rest frame of the proton, y, the inelasticity of the interaction, can be interpreted as the energy fraction of the electron carried away by the exchanged photon.

Introducing the total invariant mass of the colliding electron and proton $\sqrt{s}$, the following relations can be found.

$$s \equiv (p_e + P)^2 \approx 4E_e E_p \tag{2.4}$$

$$W^2 \equiv (P + q)^2 \approx Q^2 \frac{1 - x_{Bj}}{x_{Bj}} \tag{2.5}$$

$$Q^2 \approx x_{Bj} y s \tag{2.6}$$

The interrelations of these variables can be seen in the phase space picture of fig. 2.1. There are other ways of calculating the kinematic variables by also using the information from the measured hadronic final system. The method described above, the *electron method*, is used throughout my analysis.

2.1.1 Frames of Reference

The laboratory frame is not always the one best suited for physics analysis. Ideally, since we study the collision between a photon and a parton in the proton we would like to work in their mutual frame of rest. However, a boost to this reference-frame requires the knowledge of the fractional momentum carried by the parton inside the proton. This value is not known to sufficient accuracy, and hence a boost to this system would be inaccurate. The next best thing is to work in the rest-frame of the proton and the photon, equivalent to the rest-frame of the hadronic final state, the *Hadronic Center of Mass frame*. As can be seen in fig. 2.3b, in the hadronic center of mass frame the photon and parton collide head on[2], providing us with a natural direction of reference. Differing from the Hadronic Center of Mass frame only by a boost in the proton-direction is the *Breit frame*, where the virtual photon is at rest.

[2]assuming we can neglect the intrinsic motion of the parton.

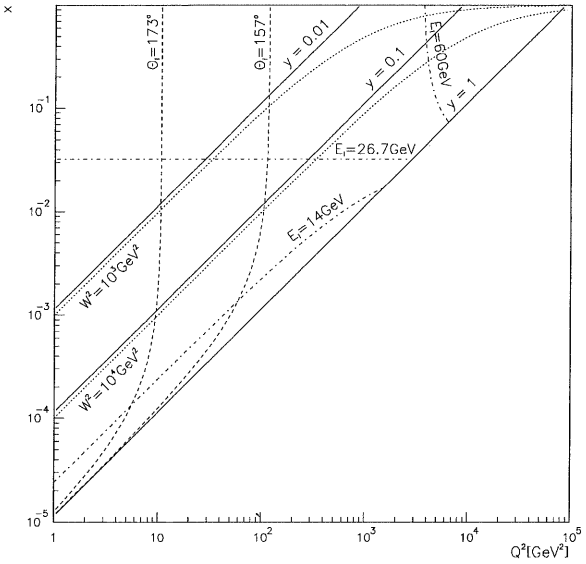

Figure 2.1: The phase space of DIS for center of mass energies of 296 GeV. The stated electron angles roughly marks the area covered by the backward electron detector in H1.

2.2 Basics of QCD

QCD, or *Quantum-Chromo-Dynamics* is the theory for essentially all interactions discussed in this thesis. Similar to the description of interactions between particles with electric charge by the theory of QED (Quantum Electro Dynamics), QCD describes the strong interaction between particles carrying a different type of charge called color (chromo). Partons can carry either 'red', 'green' or 'blue' color.

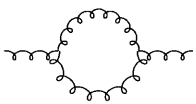

Figure 2.2: Self-interaction of the gluon.

A particle carrying all three of these colors (or the combination of color anti-color) will be colorless and hence blind to the force. The mediators of color force, analogous to the photon in QED, are called gluons. In contrast to the

photon the gluons themselves carry the charge they mediate, why self-interactions between gluons are possible as illustrated in fig. 2.2. In the mathematical representation of QCD this feature leads to an increased strength, α_s, of the strong force with increasing length between the interacting particles[3]. This of course means that real particles in nature separated by large distances cannot interact with each other via the color force, since this would obviously violate energy conservation. All real particles thus have to be colorless. If we try to separate the colored components in a colorless physical particle the energy in the field associated with the strong force will increase until it is high enough to create quark anti-quark pairs from the vacuum. The created quarks will join the partons initially separated to form colorless and thus physical particles.

2.2.1 Lowest order DIS process in QCD

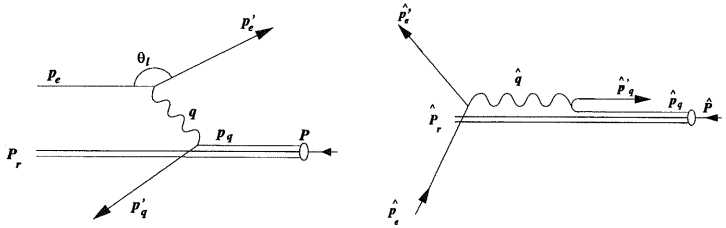

(a) (b)

Figure 2.3: Deep inelastic scattering of lowest order according to the quark parton model shown in the laboratory frame (a) and in the hadronic center of mass frame (b).

The probability of different reactions in QCD can be calculated using a perturbative approach for the relevant Feynman-diagrams. The calculations include the summation of terms in different powers of the strong coupling constant α_s, the power corresponding to the number of gluon vertices in the reaction. In the lowest (zeroth) order process in α_s, as seen in fig.2.3, a quark in the proton is given a kick by the exchanged boson producing a jet of particles balancing the p_t of the electron. For pure photon exchange we can write the (differential) cross section of the pure electromagnetic process

[3]This statement can be converted into the statement that the strength of the strong force increases with decreasing energy scale via the Heisenberg uncertainty principle 1.1

in the (x, z) plane as follows [1]:

$$\frac{d^2\hat{\sigma}_i}{dx_{Bj}dy} = y\frac{2\pi\alpha^2 q_i^2}{Q^2}\frac{\frac{1}{2}\{(\hat{p_e}\cdot\hat{p_q})^2 + (\hat{p_e'}\cdot\hat{p_q'})^2 + (\hat{p_e}\cdot\hat{p_q'})^2\}}{(\hat{p_q}\cdot\hat{p_q'})^2} \tag{2.7}$$

where α is the electromagnetic coupling constant, q_i is the charge of the scattered quark, and $\hat{p_e}$, $\hat{p_e}'$, $\hat{p_q}$ and $\hat{p_q}'$ are the four momenta of the electron, the scattered electron, the incident quark and the scattered quark, respectively, in the hadronic center of mass frame as noted in fig. 2.3b, and written out in eq. 2.8[4]. This formula is valid if we disregard the intrinsic motion of the quark inside the proton.

$$\begin{aligned}
\hat{P} &= \frac{2yE_eE_p}{\sqrt{4yE_eE_p - Q^2}}(1,0,0,1) \qquad (2.8)\\
\hat{p_e} &= \left(\frac{4E_eE_p - Q^2}{2\sqrt{4yE_eE_p - Q^2}}, \frac{\sqrt{Q^2(1-y)}}{y}, 0, \frac{Q^2(2-y) - 4yE_eE_p}{2y\sqrt{4E_eE_p - Q^2}}\right)\\
\hat{p_e}' &= \left(\frac{4E_eE_p(10y) + Q^2}{2\sqrt{4yE_eE_p - Q^2}}, \frac{\sqrt{Q^2(1-y)}}{y}, 0, \frac{Q^2(2-y) - 4yE_eE_p(1-y)}{2y\sqrt{4E_eE_p - Q^2}}\right)\\
\hat{q} &= \frac{2yE_eE_p}{\sqrt{4yE_eE_p - Q^2}}\left(1 - \frac{Q^2}{2yE_eE_p}, 0, 0, -1\right)\\
\hat{p_q} &= x_{Bj}\hat{P}\\
\hat{p_q}' &= \frac{2yE_eE_p}{\sqrt{4yE_eE_p - Q^2}}\left(1 - \frac{Q^2}{4yE_eE_p}, 0, 0, -(1 - \frac{Q^2}{4yE_eE_p})\right)
\end{aligned}$$

By expressing the four-vectors in terms of the kinematic variables [1] defined above (see eq. 2.8), equation (2.7) can be written as [1]:

$$\frac{d^2\hat{\sigma}_i}{dx_{Bj}dy} = \frac{2\pi\alpha^2 q_i^2}{yQ^2}(1 + (1-y)^2) \tag{2.9}$$

The parton densities, f_i, describing the density of the different partons in the proton, are not included here since (2.7) only considers electron-quark scattering.

2.2.2 First order QCD processes in DIS

In first, or *leading* order (LO) in α_s, there are two main different types of processes possible. These are called QCD-Compton and Boson-Gluon fusion (BGF) events, both resulting in two partons and the proton remnant in the (partonic) final state. Schematic figures of the processes can be seen in fig. 2.4. The first order processes all include one gluon vertex, why the probability of the reaction is governed by the strong coupling constant α_s. The traditional way of calculating the cross-section of any fixed order pro-

[4] where the four-vector convention is: (E, p_x, p_y, p_z)

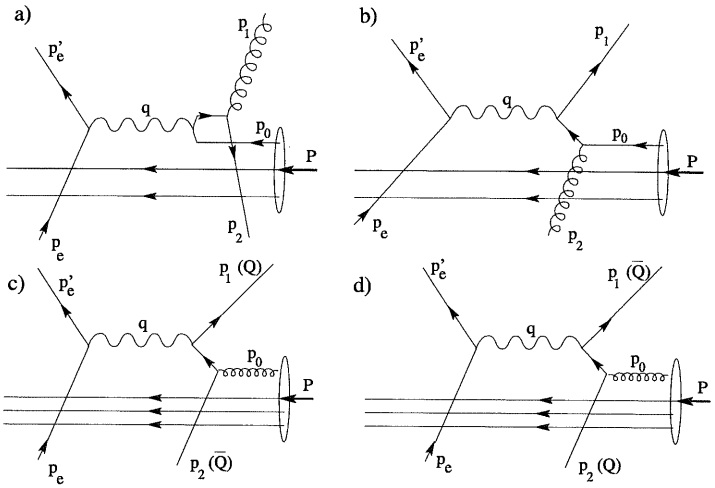

Figure 2.4: The different processes of first order in α_s. In a) and b) we see the quark initiated QCD-Compton processes. In c) and d) we see the gluon initiated Boson-Gluon fusion processes. The outgoing partons with four momenta p_1, p_2 are either a quark/anti-quark or a quark/gluon. In c) and d) the the two different ways of numerating the outgoing partons is shown.

cess is by that of matrix elements in the perturbative expansion of QCD. In principle this concept can be used to calculate the cross-section of any final state. However, with increasing order the calculations becomes more and more difficult as the multitude of diagrams rapidly increase with the increasing number of partons involved in the reactions. In practice the calculations have only been carried out and implemented in Monte Carlo programs to second, or Next to Leading order in α_s.

In leading order QCD processes the Lorentz invariant partonic scaling variables x_p and z are useful when describing the kinematic properties:

$$x_p \equiv \frac{Q^2}{2p_0 \cdot q} = \frac{Q^2}{2\xi P \cdot q} = \frac{x_{Bj}}{\xi} \tag{2.10}$$

$$z \equiv \frac{p_0 \cdot p_1}{p_0 \cdot q} \tag{2.11}$$

where x_p is the fraction of the initial parton momenta carried by the struck parton and ξ is (in leading order) the fraction of the proton momentum carried by the initial parton $p_0 = \xi P$.

In the lowest order process seen in fig. 2.3b the transverse momenta p_t of the outgoing parton with respect to the virtual photon direction is always

zero in the hadronic center of mass system[5]. In first order the outgoing parton transverse momenta can be expressed as:

$$p_t^2 = \frac{(1-x_p)z(1-z)}{x_p}Q^2 \tag{2.12}$$

The parton cross-section for the first order processes can now be written as [1]:

$$\frac{d^5\sigma}{dx_p dy dz dp_t^2} = \frac{\alpha^2 q_q^2}{6\pi^2 Q^4} y\delta(p_t^2 - \frac{(1-x_p)z(1-z)Q^2}{x_p}) L_{\mu\nu} M_{ij}^{\mu\nu} \tag{2.13}$$

Where $L_{\mu\nu}$ is a tensor describing how the lepton couples to the photon, the tensor $M_{ij}^{\mu\nu}$ describes how the photon couples to the parton side of the process and $dp_t^2 = p_t dp_t d\phi$. We get three expressions [1] for the different processes[6].

$$\begin{aligned}
L_{\mu\nu}M_{qg}^{\mu\nu} &= \frac{64\pi}{3}\alpha_s Q^2 \frac{(p_e\cdot p_0)^2 + (p_e'\cdot p_1)^2 + (p_e'\cdot p_0)^2 + (p_e\cdot p_1)^2}{p_0\cdot p_2 \;\; p_1\cdot p_2} \\
L_{\mu\nu}M_{gq}^{\mu\nu} &= \frac{64\pi}{3}\alpha_s Q^2 \frac{(p_e\cdot p_0)^2 + (p_e'\cdot p_2)^2 + (p_e'\cdot p_0)^2 + (p_e\cdot p_2)^2}{p_0\cdot p_1 \;\; p_1\cdot p_2} \\
L_{\mu\nu}M_{q\bar{q}}^{\mu\nu} &= 8\pi\alpha_s Q^2 \frac{(p_e\cdot p_2)^2 + (p_e'\cdot p_1)^2 + (p_e'\cdot p_2)^2 + (p_e\cdot p_1)^2}{p_0\cdot p_1 \;\; p_0\cdot p_2}
\end{aligned} \tag{2.14}$$

Using the relations in eq. (2.10, 2.12) it can be shown that the expression in eq. (2.14) and hence the cross-sections for the corresponding processes diverge due to singularities as $x_p \to 1$, $z \to 1$ or $z \to 0$. Hence these calculations are not safe in the regions of emission of very soft or collinear gluons[7]. This is an effect of neglecting higher order diagrams that ultimately would ensure the cancellation of all of these divergences. Requiring a minimum value of the p_t of the partons, as seen in eq. (2.12), ensures that these divergent region are avoided.

2.2.3 Higher order QCD emissions

Since at the present stage, only the matrix elements up to Next To Leading order (NLO) have been calculated, an alternative approach has to be used to take the non-negligible higher order gluon emissions into account.

The full perturbative expansion of the DIS cross section can be approximated using a technique called *resummation* [2] adding up a subset of the full number of infinite terms. In the so called leading-log approximation considered here, the basic processes are the direct splittings of a parton into two daughter partons as seen in figure 2.5a.

[5] neglecting the intrinsic motion of the partons inside the proton

[6] The two diagrams for the BGF process gives the same expression since nature does not distinguish quarks from anti-quarks in this respect.

[7] Or in case of BGF, the splitting of a gluon into two quarks collinear to the initial gluon, or having non-finite energy.

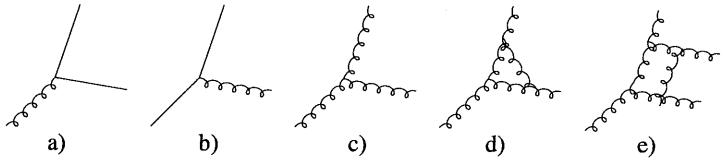

Figure 2.5: To leading α_s only the three direct $1 \rightarrow 2$ QCD processes seen in (a-c) are taken into account. In (d-e) examples of higher order kernels can be seen.

The DGLAP Parton Evolution Equation

One group of terms in the full perturbative QCD expansion are of the form $(\alpha_s \ln Q^2)^n$. These are large at large values of Q^2 where they are expected to dominate the cross section. After resummation one arrives at the famous DGLAP evolution equation [3, 4, 5, 6]:

$$\frac{df_i(x,t)}{d\ln t} = \frac{\alpha_s(t)}{2\pi} \sum_j \int_x^1 \frac{dx'}{x'} f_j(x',t) P_{i/j}(z) \tag{2.15}$$

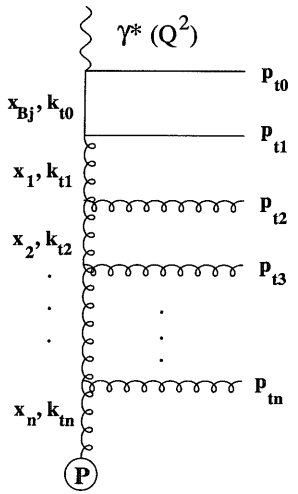

Figure 2.6: Higher order emissions as modeled by a parton shower.

Where $f(x,t)$ is describing the density of partons carrying a momentum fraction, x, probed at a scale t. The splitting functions, $P_{i/j}$, describe the probability of a parton j, either a quark, anti-quark or a gluon, transforming into a parton of type i with a fraction, $z = x/x'$, of the original parton momentum. To interpret the equation it is relevant to discuss the fast moving proton as a container of a number of more or less virtual partons. Any parton found may be the result of radiation from another parton with a larger fraction of energy, x. In each splitting the virtuality of at least one parton has to increase why the time scale allowed for these partons to exist decreases. Remembering that resolving an object demands the probe to have a smaller wavelength than the target, the gluon cascade (ladder diagram) in fig. 2.7 can be seen as a succession of probes resolving partons with decreasing virtuality, going from the photon towards the proton side of the ladder. Hence, changing the scale (virtuality) t of the probe used we

expect a change in the number of partons found with a certain value of of x. The equation thus describes the probability change of finding a parton of type i, with momentum fraction x inside the proton. At small-x_{Bj} the DIS cross-section is dominated by the large gluon-density. The gluon splitting function [7] is given by:

$$P_{gg}(z_i, k^2) = \overline{\alpha}_s \left(\frac{1}{z_i} - 2 + z_i(1 - z_i) + \frac{1}{1 - z_i} \right) \frac{1}{k^2} \tag{2.16}$$

In the DGLAP formalism the increasing $|k^2| \sim t$ in the gluon chain is interpreted as an increased transverse momentum[8] of the gluon: $|k_{tn}^2| \ll .. \ll |k_{t2}^2| \ll |k_{t1}^2|$, where $k_{ti} = (0, k_{xi}, k_{yi}, 0)$ is the transverse component of the propagator gluon four momentum k_i.

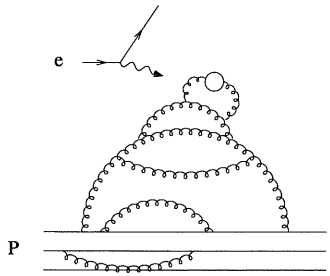

Figure 2.7: The proton as a source of gluon radiation in a DIS event. In case of an interaction between the photon and one of the quarks, the "ancestor" gluons in the chain will not recombine which results in a cascade of real emissions as seen in fig. 2.2.

The branching in DGLAP (as for the Monte Carlo implementation of any parton evolution equation) starts at a low scale Q_0 where a measured parton distribution function (pdf) is needed. According to the *factorization theorem*, non-interfering processes (e.g waves of different wavelengths) can be treated independent of each other. When generating events (see section 2.5), using the DGLAP approach for the higher order QCD emissions, this is utilized dividing the event into a sub-process at the hardest scale in the event, and a parton shower ladder. The probability distribution for the hard sub-process is taken from the LO matrix elements (see eq. 2.13), while the parton shower is generated iteratively using the DGLAP evolution equation.

The BFKL Parton Evolution Equation

Another subset of terms in the perturbative expansion is of the form $(\alpha_s ln(1/x))^n$. At very small values of x these terms are expected to become larger than the $(\alpha_s \ln Q^2)^n$ terms (at least if Q^2 is not very large) why they will dominate the DIS cross section. After resummation one arrives at the BFKL equation

[8] $k_n^2 = \frac{k_{tn}^2}{1-x_n}$, $x \ll 1.$, see Appendix B.

[8, 9, 10]:

$$\frac{d\mathcal{F}(x,k_t^2)}{d\ln(1/x)} = \frac{3\alpha_s(t)}{\pi} k_t^2 \int_0^\infty \frac{dk_t'^2}{k_t'^2} \left[\frac{\mathcal{F}(x,k_t'^2) - \mathcal{F}(x,k_t^2)}{|k_t'^2 - k_t^2|} + \frac{\mathcal{F}(x,k_t^2)}{\sqrt{4k_t'^4 + k_t^4}} \right] \quad (2.17)$$

defined for gluons which are dominant at small x. The equation describes the change of the gluon density $\mathcal{F}(x,k_t^2)$ with respect to a change in the gluon fractional momentum. The BFKL equation implies strong ordering in x: $x_1 \ll x_2 \ll .. \ll x_n$ while the propagator gluon k_t is allowed to walk randomly in the k_t plane in contrast to the DGLAP equation where the $|k_t|$ is strictly ordered. The derivation of the BFKL equation is such that for the final state properties it cannot guarantee the correctness of the small-x logarithms. This leads to problems implementing it into a Monte-Carlo generator.

The CCFM Parton Evolution Equation

The higher order problems with the BFKL equation are absent in the so called CCFM equation [11, 12, 13, 14]

$$\overline{q}^2 \frac{d}{d\overline{q}^2} \frac{x\mathcal{A}(x,k_t,\overline{q})}{\Delta_s(\overline{q},Q_0)} = \int dz \frac{d\phi}{2\pi} \frac{\tilde{P}(z,\overline{q}/z,k_t)}{\Delta_s(\overline{q}Q_0)} x'\mathcal{A}(x',k_t',\overline{q}/z) \quad (2.18)$$

which takes these effects into account by requiring angular ordering in the emitted chain of gluons, corresponding to a suppression of gluon emissions from color coherence arguments. The equation is valid for gluons at low-x and effectively resums the large $(\alpha_s ln(1/x))^n$ terms avoiding the BFKL problem of energy conservation by the inclusion of collinear emissions in the splitting kernel [15]. In (2.18) $\mathcal{A}$ is the CCFM *unintegrated gluon density*, a function of the three independent variables x, k_t and the angular limit for emission, $\overline{q}$. In DGLAP, $f(x,t)$ integrates over k_t, whereas CCFM gives the full kinematics.

The Color Dipole Model

Another concept used for higher order QCD emission is the Color Dipole Model (CDM) [16, 17]. In this model the emissions take place from a color dipole spanned by a quark and an anti-quark. A gluon emitted carries color charge itself why it will act as a kink on the color string between the quark and anti quark as seen in fig. 2.8a, thus leaving us with two new dipoles. These dipoles can subsequently radiate new gluons in an iterative manner independent of each other, with the constraint that at every new emission the k_t is smaller than in the preceding one[9]. The CDM concept does not distinguish between initial and final state radiation as is done in the parton

[9]Not to be confused with the ordering in transverse momentum of the initial state radiation in the DGLAP equations.

shower concept, instead the subsequent emissions of gluons takes place between the struck quark and the proton remnant. A schematic picture of a diagram can be seen in fig. 2.9c. The phase-space for the CDM radiation of

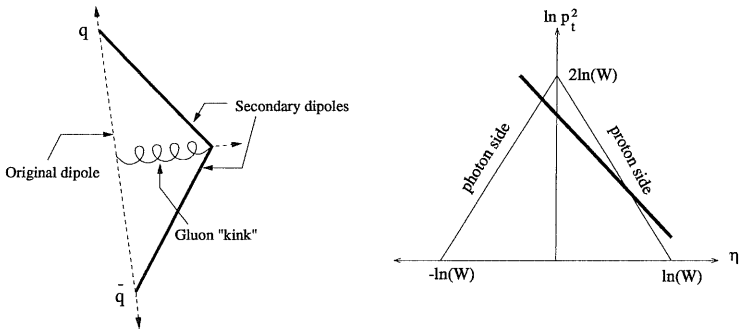

a) b)

Figure 2.8: a) A schematic picture of the iterative radiation of gluons from color-dipoles, creating secondary dipoles. b) The phase-space available for emission of a gluon, from a dipole of mass W, with transverse momentum p_t and pseudo-rapidity η with respect to the original axis in the dipole center of mass system. The thick line shows the reduction in phase space on the proton side (positive rapidities) due to the extension of the proton remnant.

gluons of transverse momenta p_t and pseudo-rapidity η with respect to the original axis in the dipole center of mass system for a dipole of energy W is defined by the constraint:

$$p_t \cdot \cosh \eta < \frac{W}{2} \tag{2.19}$$

can be seen in fig. 2.8b. The constraint is a result of energy and momentum conservation [18]. Since in CDM the proton remnant is treated as an extended object, and emissions corresponding to small wavelengths from an extended source are suppressed, this introduces a parameter, redefining the phase space available for gluon emission (see fig. 2.8b). Treating the photon as an extended object a similar suppression enters on the photon side. In CDM there is no natural description of the BGF process.

2.2.4 Resolving the photon

As described in section 2.2.3 the DGLAP parton emissions are strongly ordered in transverse momentum k_t. However, at virtualities of the photon

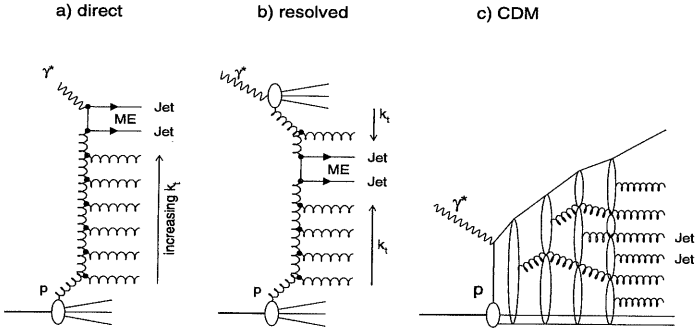

Figure 2.9: Generic diagram of initial state parton emission (a,b). In the direct process the hardest emission given by the QCD matrix element occurs at the top of the ladder. Emissions down the ladder are ordered with decreasing transverse momenta k_t. In the resolved process (b) the hardest emission given by the QCD matrix element may occur anywhere in the ladder with increasingly soft emission along the ladder towards the proton and the photon. In the color dipole model (c) gluon emissions are not ordered in transverse momentum k_t.

comparable in size, or smaller than the k_t in the matrix element, there is a possibility of resolving the parton content of the photon, thus allowing a parton shower to develop on both sides of the hard sub-process, as seen in fig. 2.9b. Since the matrix element need no longer to be placed on top of the ladder diagram, the strong ordering in k_t is broken.

2.3 Hadronisation and Jet production

At the smallest time scales[10] the partons in the matrix element of the hard sub-process define the basic properties of the distribution of final state particles. The additional parton shower emissions in the individual events are associated with a smaller momentum transfer compared to the one in the matrix element. The main effect of the emitted partons is thus a broadening of the energy flow around the jets. Only in some occasions the partons from the shower will be energetic enough and sufficiently separated in phase space to form a separate jet. The partons after parton showering are all colored objects. The quarks even carry fractional electric charges. Since no colored objects, nor fractional charges have been observed in nature, a process that

[10]Corresponding to the highest virtuality in the process

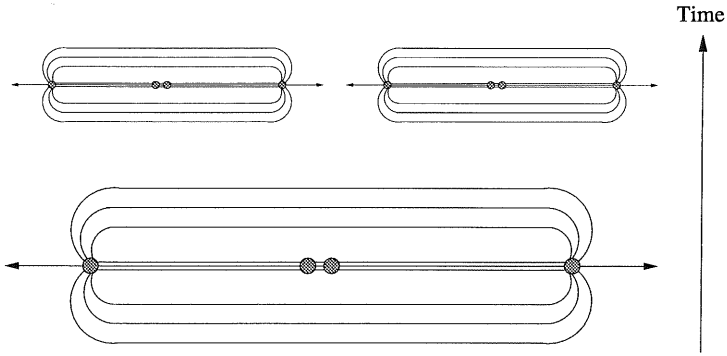

Figure 2.10: The string stretched between two quarks is split in two when a pair of quarks emanates from the virtual sea of particle-antiparticles. The process will go on in an iterative manner until the resulting string pieces are of the form of on-shell mesons. The production of baryons is similar but somewhat more complicated.

transforms the partons into colorless particles of integer charge (hadrons) is needed in our description of the process. The process is generally called hadronisation, or fragmentation. The machinery of partons transforming into final state hadrons is not known from first principles. Instead we have to use phenomenological models such as the Lund string fragmentation model [19], where the above discussed self interactions of the gluons will contract the strong force-field to a tube-like structure (see fig. 2.10) keeping the energy density per unit of length constant. As the quarks move apart their initial kinetic-energy will be transferred to the flux-tube, referred to as a *string* in the Lund model. When the quarks are separated by approximately 1 fm the energy carried by the string will be high enough to create pairs of quark anti-quarks, breaking the string as seen in fig. 2.10. The process continues until the energy of the remaining string pieces is lower than the typical hadron mass. Since the string is moving faster near the ends, in these regions the string breaking will be more frequent, why the directions of the original quarks from the hard scattering and the proton remnant will be densely populated by particles. These collimated flows of particles (see fig. 1.1) are generally referred to as *jets*. The boson gluon fusion and QCD-compton processes discussed in section 2.2.2 will both result in a final state of 2+1 jets, with two jets from the hard sub-process plus one jet from the proton remnant. These events are sometimes referred to as di-jet events. The different processes have different string configurations as seen in fig. 2.11, effecting the distribution of particles in the final state.

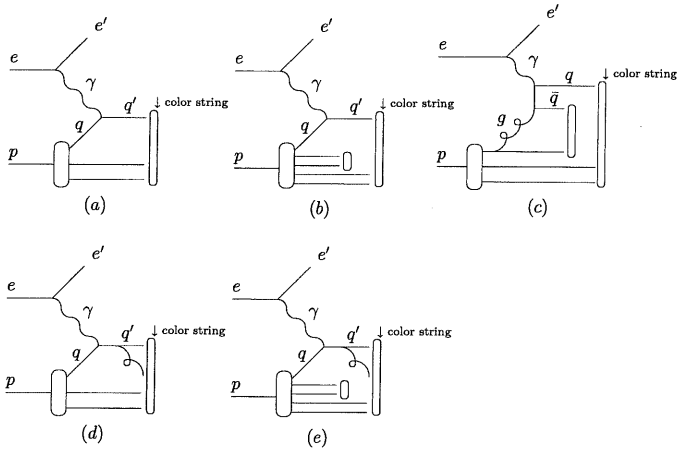

Figure 2.11: Basic processes of deep inelastic scattering. (a) lowest order scattering on a valence quark. (b) lowest order scattering of a sea quark. (c) first order Boson Gluon Fusion process. (d) first order QCD-compton event. (e) QCD-compton process where the scattering takes place against a sea-quark. Note that for processes (c)-(e) there also exist diagrams where the hard parton legs are crossed.

2.4 Cross Sections and Structure Functions

The total cross section, or probability of an electron to scatter deeply inelastic on a proton at low or medium Q^2 is most often expressed as function of the kinematic variables x_{Bj} and Q^2. The cross-section as a function of x_{Bj} is related to the parton density in the proton. In the naive QPM the proton consist only of three point-like valence quarks, why the distribution would be peaked at $x_{Bj} = 1/3$ independent of the resolution $\sim Q$, a behaviour called *scaling*. Taking the intrinsic motion of the quarks into account the delta-function at $x_{Bj} = 1/3$ is replaced by a distribution around 1/3. When the gluons are taken into account as QCD is added, we include the existence of sea-quarks, as gluons split in pairs of quarks and anti-quarks. These sea-quarks can in turn radiate gluons thus producing a chain of partons with decreasing x_{Bj} at each step of emission. By increasing the resolution in our measurement we become sensitive to partons carrying smaller fractions of momentum, and what seemed like a quark at one value of Q^2, will appear as a quark with a radiated gluon at a higher value of Q^2. Thus we expect the cross section to depend on Q^2, an effect called *scaling violation* which has been observed in experiments and is described by a Q^2 dependent structure

function $F_2(x, Q^2)$.

$$\frac{d^2\sigma}{dxdQ^2} = \frac{4\pi\alpha^2}{xQ^4}\left[\left(1 - y + \frac{y^2}{2}\right) \cdot F_2(x, Q^2) - \frac{y^2}{2} \cdot F_L(x, Q^2)\right] \tag{2.20}$$

The differential cross section as seen in eq. (2.20) is most often parametrized using the concept of structure functions F_2 and F_L, with F_2 representing the density of quarks for transverse polarized photons. The structure function for longitudinally polarized photons F_L is negligible compared to F_2 in a first approximation.

$$F_2(x, Q^2) = x \sum_i e_{q_i}^2 \left[q_i(x, Q^2) + \overline{q}_i(x, Q^2)\right] \tag{2.21}$$

Eq. (2.21) sums over all quark flavors, with $q_i(x, Q^2)$ and $\overline{q}_i(x, Q^2)$ being the individual quark and anti-quark densities for the different flavors.

2.5 Event Generation and Simulation

In a typical final state of deep inelastic scattering at HERA energies, there are around 20-50 charged and neutral particles. To make an exact calculation of the distribution of particles, we would need the matrix element calculation to all orders, and a description of the fragmentation process being more than a phenomenological model. Since this is not the case, another approach has to be used. Therefore, in comparisons between the experimental results and theoretical predictions, we generally use Monte Carlo generators, producing complete final state events. The event generators link together the, essentially independent, different sub-processes of DIS described above namely the matrix element, the parton shower and the hadronisation. The final states of particles can be passed through a detector simulation program, acting as an emulator (in the ideal case) of the experimental situation as seen by the particles passing through the detector. In this way one can follow the history of particles from the initial generation of pure partons from the matrix element through to the final state hits of energy-clusters in the detector.

The Monte Carlo generator chooses the underlying process and randomly generates the values of all kinematic and other relevant variables from the appropriate theoretical probability-distributions, adds the higher order QCD activity and hadronises the partons creating the final state of particles. This means that one can impose cuts on variables right from the generation of the matrix element partons up to the corresponding quantities at the detector level. Hence it is possible to convert a measured signal or distribution in the detector to the corresponding signal or distribution at the level of hadrons, where the results can be more easily compared to theoretical predictions independent of the experimental facility. The simulation of events is also useful at the planning stages of experiments where the expected final states of an experiment can be simulated and the detectors can be designed to best measure the quantities necessary for the analysis to be performed.

Chapter 3

The Experimental facility

The construction of the Hadron-Elektron-Ring-Anlage "HERA", was finished in 1991 at the DESY laboratory in the outskirts of Hamburg, Germany. The collider is the first of its kind, accelerating protons and electrons in two separate rings in opposite directions to highly relativistic energies. The particles are then brought to collide at two oppositely situated interaction regions housing the H1 and ZEUS detectors. This work has been performed with the H1 detector described below, but first some words on the system of accelerators.

3.1 HERA

The HERA accelerator complex is a huge system of accelerators. The acceleration and production of particles is done in several steps before they are inserted in the two 6.3 km circumference HERA rings and finally accelerated to their colliding energies of around 27.5 GeV (e^-) and 820 GeV[1] (p^+) respectively. The collision center of mass energy is $\sqrt{s} \approx 300$ GeV. The basic facility setup can be seen in fig. 3.1.

The electrons are injected into the DESY-II ring after gaining the energy of 450 MeV in the linear accelerator LINACII. After being accelerated to the energy of 7 GeV they are injected into the larger PETRA-II ring where the acceleration ends at an energy of 13 GeV and the electrons are transferred to the HERA-e ring.

The protons are produced by stripping negatively charged hydrogen ions from their electrons. They are accelerated to 50 MeV in the linear accelerator LINACIII, and injected into the DESYIII ring. The protons are then accelerated to 7.5 GeV, injected into the PETRAII ring, accelerated to 40 GeV and in the final step they are injected into the HERA-p ring.

The protons and electrons are accelerated by radio-frequency (rf) cavities. In order to keep the protons in a circular orbit at the highest energies, helium cooled super-conducting magnets are needed to produce a magnetic field of

[1] In the end of 1998 the proton energy was upgraded from 820 GeV to 920 GeV.

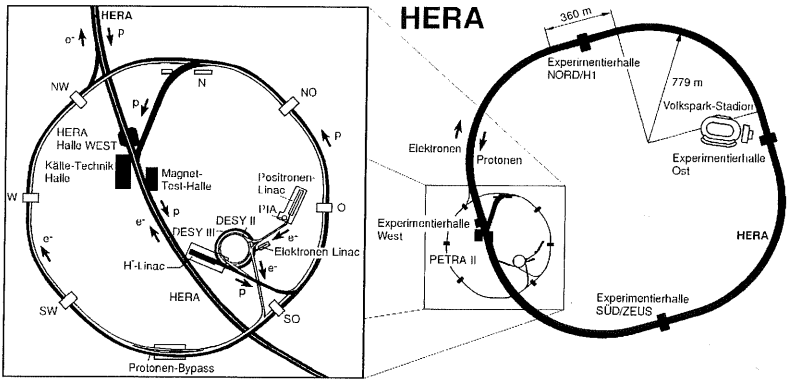

Figure 3.1: *Overview of the HERA complex.*

4.7 T. In the end, 210 bunches of electrons and protons circle the HERA ring, containing around 10^{10} $(e^+)^2$ and 10^{11} (p^+) each. At the speed of light this means that the time between two bunches (bunch crossing time) is 96 ns, which puts high requirements on the resolution of all the four dimensions (time and space) measured by any detector.

The tasks of HERA

The HERA facility provides the opportunity to perform a multitude of physics investigations. The two main experiments H1 and ZEUS are built around the beam-pipe where the particles are brought to collide. The topics to be studied at these detectors are of fundamental importance for the understanding of the nature of matter. They are among others:

- Measurements of the proton inner structure, including:
  - The quark densities.
  - The gluon density.
  - Diffraction.
- Measurement of the strong coupling constant α_s.

[2]HERA has been running with both electrons and positrons.

- Tests of QCD by measurements of the hadronic final states as particle jets.
- Studies of the confinement nature of quarks and gluons inside the nucleons.
- Measurements of the hadronic structure of the (virtual) photon.
- Search for physics beyond the standard model.

3.2 The H1 detector

As can be seen in fig. 3.2 the H1 detector [20] is a major[3] structure of subdetectors arranged like the shells of an onion around the beam-pipe. This is typical for a multi-purpose detector in which different kinds of particles have to be detected, and their energy and momenta have to be measured. Since the particles collide with highly asymmetric energies, the center of mass of the electron and proton in the collisions is boosted along the proton direction with a $\gamma_{cm} \approx 2.9$. Most particles are therefore expected to be produced in the proton direction. This is taken into account in the design of the detector which is much more massive in the forward region. This is evident in fig. 3.3 where the upper half of the Liquid Argon barrel (LAr) is seen in profile.

Starting from the point of interaction, the main parts of the detector are the silicon micro-vertex detector, the central and forward tracking system surrounded by the liquid argon and backward calorimeters, the superconducting coil providing the 1.15 T magnetic field for momentum measurements, the iron yoke, sometimes referred to as the *instrumented iron*, built up in three layers of iron separated by air-gaps accommodating detectors with the purpose of estimating the energy leaking out of the detector and detecting muons. Some of the more important parts of the detector like the electron detection system, and the hadronic calorimeter will be described in the next section.

3.2.1 The electron detection system

The information from the scattered electron is essential for the reconstruction of the kinematics of the event. Thus much effort has been put into the construction of the electron detection system. In most DIS events the electron path is only slightly shifted by the interaction with a proton. The backward region, the exit region of the electron, is therefore hosted by a very precise electron detection system. The original detector [21] consisting of lead-scintillator sandwich stacks, the Backward ElectroMagnetic Calorimeter (BEMC), was replaced in the end of 1994 by a SPAghetti (or fiber)

[3] 10x10x12 m^3 (x,y,z)

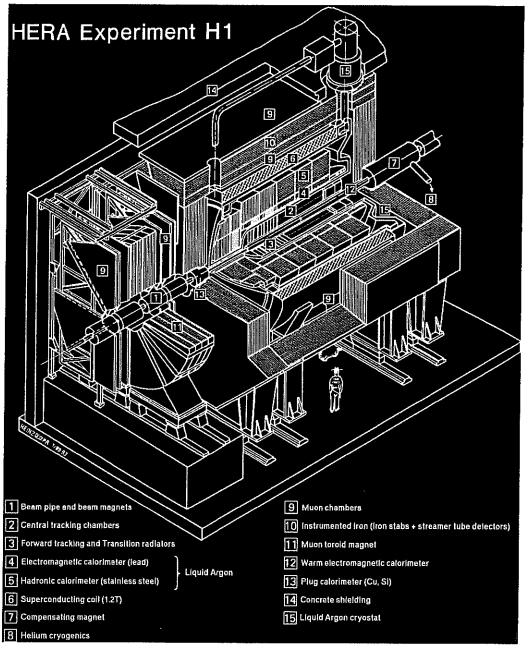

Figure 3.2: The H1 detector.

CALorimeter, the so called SPACAL detector, which increased the acceptance of the scattered electron to smaller angles with respect to the beampipe, and thereby extended the region of Q^2 to lower values, as can be seen in fig. 3.5. The upgrade also improved the energy and angle resolution. To improve the separation of electromagnetic and hadronic showers the new calorimeter was built with both an electromagnetic and a hadronic segment. Up to 1994 a backward proportional chamber (BPC) was placed in front of the BEMC. Its four wire planes measured the position of the scattered electron to an accuracy of 1.5 mm. The BPC is now replaced with a Backward Drift Chamber (BDC) with a resolution better than 1 mm. At scattering angles larger than 26 degrees with respect to the incoming electron direction the LAr calorimeter is used for the electron identification. The energy resolution of electrons in the LAr calorimeter is around $12\%/\sqrt{E}$, the resolution in the BEMC and SPACAL can be seen in table 3.1. The SPACAL now covers the region $1< Q^2 <100$ GeV^2, and the designed two layer structure makes it possible to identify one of the main sources of background, the photoproduction events, even better. In a photo-production event the deflection

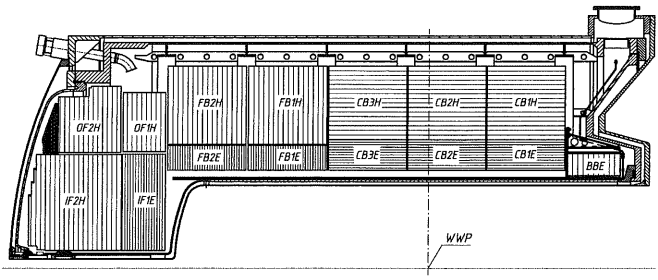

Figure 3.3: One half of the liquid argon barrel calorimeter.

of the electron is too small for it to hit the BEMC, but a hadron entering the BEMC can be misidentified as the electron. By requiring little activity in the hadronic segment as well as requiring a signal in the tracking chamber matching the shower position in the BEMC, these events can be identified and discarded. More on background reduction can be found in section 4.1. The increased resolution in energy and angle of the new detector is important in order to minimize the systematic errors in the determination of the kinematic variables x_{Bj}, y and Q^2. Some basic facts about the two backward calorimeters used can be found in table 3.1

3.2.2 Calorimetry

Apart from the backward calorimeter described above, the calorimetric system of H1 consists of the LAr calorimeter as seen in fig. 3.3, the PLUG calorimeter in the very forward region, the instrumented iron, and the backward electron calorimeter. The calorimetric system was designed to provide precise measurements of particle energies and momenta, as well as a high capability of jet measurements including large numbers of particles. The main

	BEMC	SPACAL
Usage	1992 - 1994	1995 - 1999
Acceptance	$151° < 176°$	$153° < 177.5°$
σ / E (e.m.)	10% / $\sqrt{E}$	7% / $\sqrt{E}$
Energy-scale known to:	2%	1%
Position accuracy	$\mathcal{O}(1mm)$	$\mathcal{O}(1mm)$

Table 3.1: Some basic properties of the old (BEMC) and new (SPACAL) backward calorimeters measuring the scattered electron.

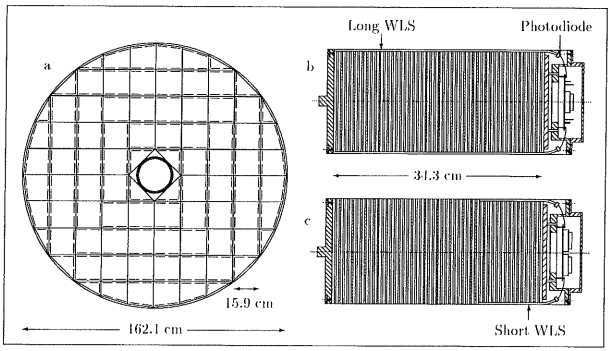

Figure 3.4: Transverse view of the old backward electromagnetic calorimeter together with a cross section of two of its 88 modules, called *stacks*.

calorimetric barrel consist of one electromagnetic and one hadronic part, situated inside the large coil to minimize the amount of dead material in front of it. The LAr calorimeter covering angles of $4° < \theta < 154°$ together with the BEMC/SPACAL in the backward region and the PLUG, closing the gap to the beam pipe in the very forward region, gives an almost hermetic calorimetric coverage. However, sometimes highly energetic particles punch through the LAr calorimeter why the surrounding instrumented iron-yoke is needed to estimate the amount of energy escaping the calorimetric system. The absorber material in the barrel calorimeter is stainless steel for the hadronic part and lead in the inner electromagnetic section. The plates are separated by regions of liquid argon. The choice of liquid Argon as active medium is for the fine granularity one can achieve with a high density of read-out pads needed for π/e separation, and ease of calibration, among other factors.

3.2.3 Tracking

The tracking system in the innermost part of the H1 detector consists of a central and a forward part, as seen in fig. 3.6, to take into account the asymmetry in the collisions. The particles produced in the forward direction have larger momenta than the ones produced in the direction of the electron. The purpose of the tracking detectors is mainly to provide position information along the tracks of charged particles. Some of the chambers delivering fast read-out signals can also be used in the trigger system (see section 3.2.4). The momentum and angular resolutions are $\sigma_p/p^2 \approx 3 \times 10^{-1}$ GeV^{-1} and $\sigma_\theta \approx 1$ mrad respectively. The central tracking device consist of two cylindrical jet chambers, proportional chambers and z-chambers, covering polar

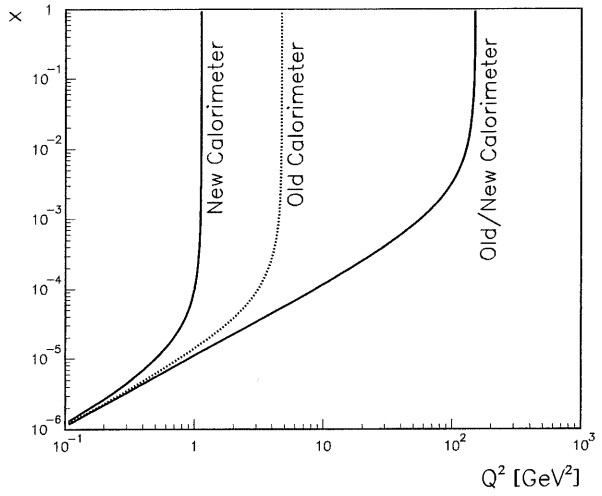

Figure 3.5: The acceptance of the old and new backward calorimeters.

angles between 25° - 155°. The forward tracking system covering the angular range 5° - 30° consists of planar chambers which provide high resolution in θ for charged particles, and radial forward tracking chambers that give a high ϕ resolution. The silicon micro-vertex detector installed in the end of 1995 now measures, together with the inner and outer central z-chambers, the vertex z coordinate to an accuracy of better than 100 μm. This makes it possible to reconstruct secondary vertices in heavy quark decays.

3.2.4 Triggering

A Bunch Crossing time of 96 ns requires a decision to be made more than 10 million times every second whether or not to store data from the detector. If all the information was to be fully processed, the amount of data would grow out of proportion. Only a fraction of the events detected is the result of a true interesting e-p collision. The task of the triggering system is to select these events, reducing the signal frequency from $\sim$ 100 kHz (far from all bunch crossings produce a trigger signal to start reading out data) to the order of 10 Hz. In the selection process, the requirements put on the events by the trigger system lead to a suppression of the various background contributions coming from synchrotron radiation produced by the electron beam, beam-gas interactions and beam-wall interactions of the proton beam. The selection of potentially interesting physics events is done in four steps,

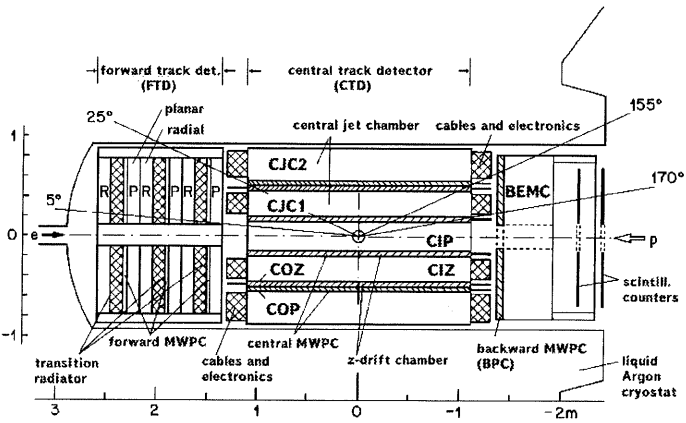

Figure 3.6: The central and forward tracking system of H1.

also called *trigger levels*. The first step (L1) is to decide if the particles can be traced back to the interaction region of the proton and electron beams. By comparing the arrival time of the particles in the various sub-detectors it can be established whether the particles originate from the interaction region or if they are coming from outside the detector volume. The central tracking system gives a fast estimate of the vertex position, and the full L1 triggering system consist of a larger number of sub-triggers each based on the information from the various sub-detectors. Trigger level two (L2) is based on neural networks recognizing the typical patterns of interesting physics events in the detector. The acceptance rate of the L2 trigger is less than 200 Hz. In level three (L3) the information gathered in the processing of L1 and L2 together with a partial set of data from the sub-detectors is used, mainly to reduce the dead time of the detector by sending a signal to stop the relatively time consuming process of reading the entire information of an event into the buffer. The output rate of L3 is less than 50 Hz. In level four (L4) the relatively low signal frequency allows for more information to be processed. The decision to keep or reject an even at this level is based on the L1 trigger information, the total raw data from the event, and reconstructed event quantities. In the L4, sub-trigger information from L1 is combined to classify the events according to the type of physics in the interaction. The final output rate is around 10 Hz.

Part I

The Nature of Hard Processes in Deep Inelastic Scattering

Chapter 4

Jet Rate Measurement

The basics of this analysis was first presented in a PhD thesis [22]. There, some problems in the theoretical understanding of the results were pointed out. This work contains the confirmation and extension of the di-jet rate measurement R_2 in deep inelastic scattering in order to get agreement with the NLO calculations which was obtained by including an additional cut on the jet p_t's as explained in section 4.2 and 4.3. The extension led to a further understanding of perturbative QCD and the results were published in [23] (see also appendix A).

The data analysed are from the 1994 data taking period. The aim is to measure the production probability of events leading to 2+1 jets as a result of the BGF and QCD-compton processes. These processes (see section 2.2.2) both include a gluon vertex, and the probability for the production of such events is hence governed by the strong coupling constant α_s. In the kinematic region where enough statistics was available, $5 < Q^2 < 100$ GeV^2, the transverse momenta, p_t, of the hard jets in the hadronic center of mass frame, is of the same order as the virtuality of the photon (Q^2), as the jets are required to have a p_t of more than 5 GeV to be accepted by the jet algorithm. The demand of a minimum p_t is needed since perturbative calculations are reliable only at scales significantly higher than some minimum scale in QCD, roughly the mass of the lightest hadrons. The results are corrected to the hadron level using generated and detector-simulated events from Monte Carlo generators.

4.1 Event selection

The DIS events were chosen from events identified as having an electron in the backward electro-magnetic calorimeter, and the cuts were designed for an efficient event selection as well as suppression of the background sources and minimization of the radiative QED correction. Furthermore the cuts ensure that the electron is reconstructed well within the acceptance region of the BEMC, and that the kinematic variables are well reconstructed. More on the

selection of data than presented here can be found in [22]. The selected runs from the 1994 data taking period correspond to an integrated luminosity of 1.97 pb^{-1}. The overall trigger-efficiency for the low-x_{Bj}, low-Q^2 trigger can be seen in fig. 4.1. The purpose of this trigger is to identify scattered electrons from DIS processes in the angular acceptance region of the BEMC. The efficiency in selecting electrons of higher energies is nearly 100% using this trigger, as seen in fig. 4.1. Except for the photo-production background

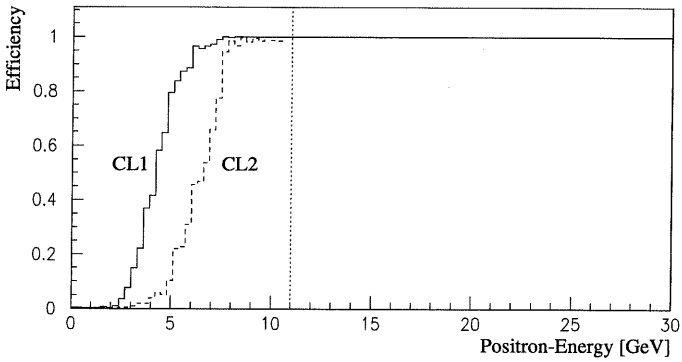

Figure 4.1: Trigger efficiency of the two level one trigger CL1 and CL2 thresholds as a function of the energy of the scattered electron. CL2 corresponds to the S_0 standard low-Q^2 trigger. The vertical dashed line shows the electron energy cut imposed on the data. The efficiency in the remaining sample is close to 100%.

described in section 3.2.1 the other sources of background are interactions with gas-atoms in the vacuum tube, as well as protons and electrons hitting the walls of the beam pipe. Many of these can be disregarded using Time-Of-Flight (TOF) windows[1] and vertex requirements. The full set of cuts imposed to suppress the background and ensure good quality data in the selected runs is presented below.

4.1.1 Electron energy cut

The effect of making a cut on the scattered electron-energy is manifold. Cutting out the low energetic region will reduce the Photo-production background substantially as seen in fig 4.2, at the same time as it ensures a high

[1]Particles from the actual event cannot hit the detector outside certain time-of-flight windows decided by the knowledge of bunch-crossing times in the detector and the speed of light.

efficiency of the S_0 sub-trigger of the BEMC as described in fig. 4.1. The imposed cut on the scattered electron energy was:

$$E' > 11 \text{ GeV}$$

4.1.2 Electron cluster radius cut

The footprint of an electron, and a hadron in a photo-production event, is quite different in the radial dispersion of activity in the different stacks of the BEMC. Hadrons generally create much broader showers. An energy-

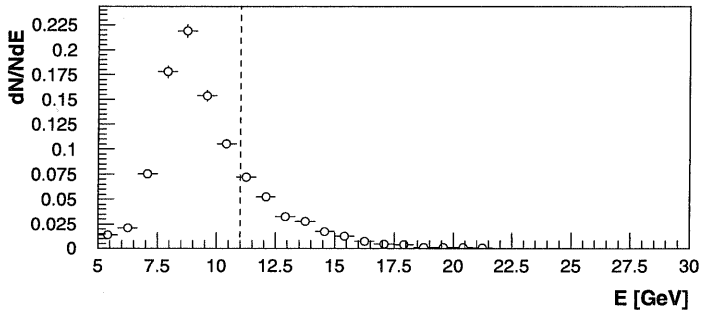

Figure 4.2: The energy-spectrum of the remaining electron candidates in the Photo-production background sample as generated by the PHOJET Monte-Carlo program after applying all DIS cuts except the electron energy cut indicated by the hatched vertical line.

weighted cluster radius, describing the broadness of the cluster can be defined as:

$$R_{cl} = \frac{1}{E} \sum_{i=1}^{n} E_i \times |r_i - r_{cl}| \tag{4.1}$$

where r_i is the position of the module in the BEMC detecting the energy E_i, and r_{cl} is the position of the electron cluster in the BEMC. We can now compare this quantity for the photo-production Monte-Carlo sample and the scattered electron in DIS as is done in fig. 4.3. The selected cut of:

$$R_{cl} < 5 \text{ cm}$$

effectively reduces the photo-production background at the same time as it rejects less than 1% of the DIS sample.

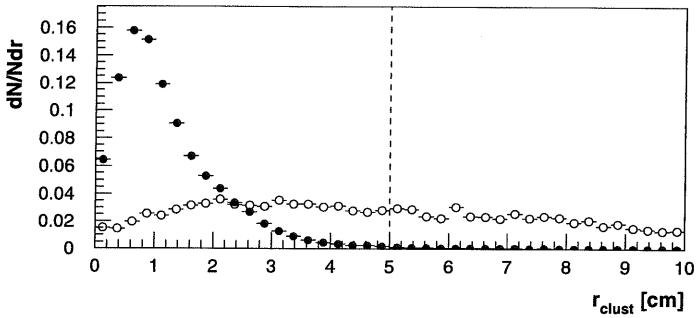

Figure 4.3: The dispersion of the cluster induced in the BEMC by hadrons (open circles) and from the H1 DIS data. The hatched line indicate the selected cut-value.

4.1.3 The BPC signal cut

When the electron passes through the BPC in front of the BEMC it is likely to give a signal. The track connecting the event vertex and the center of gravity of the cluster in the BEMC is compared to the measured position in the BPC. By applying a cut on this distance, d_{bpc}, it is possible to further discriminate between the hadrons of photo-production and the electrons of DIS as seen in fig. 4.4. Neutral hadrons giving fake electron signals in the BEMC, are not very likely to produce a signal in the BPC. However, when a π_0 close to a charged hadron enters the backward region, the charged hadron can give a signal in the BPC at the same time as the π_0 decays to two photons producing an electromagnetic shower in the BEMC. These events will produce a flat d_{BPC} distribution as seen in fig. 4.4. The selected cut in d_{BPC}:

$$\mathrm{d}_{BPC} < 5 \text{ cm}$$

will efficiently reduce the photo-production background but leave the DIS sample intact.

4.1.4 The Vertex requirement

The length of a proton bunch circulating the HERA ring is 44 cm and the length of an electron bunch is only 2.5 cm. The distance between two bunches is a bit less than 30 meters. The finite time spread of the bunches and the zero degree crossing angle leads to a total interaction length of $\approx \pm$ 50 cm around the nominal interaction point. The probability of beam-gas interactions, or beam-pipe wall interaction with the electron and proton beam is constant

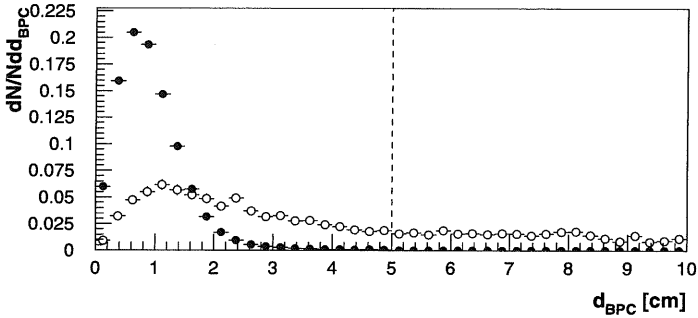

Figure 4.4: The spectrum of distance from the BPC signal and the track, from the event vertex and the cluster center of gravity in the BEMC. The DIS events (black) have been simulated using he DJANGO Monte Carlo, and the photo-production background have been simulated using the PHOJET Monte Carlo.

along the beam-pipe. The absence of a vertex close to the nominal interaction point is thus good evidence of background. Therefore the imposed cut of:

$$-25 \text{ cm} < z_{vtx} < 35 \text{ cm}$$

will effectively reduce this kind of background. The asymmetric cut reflects the fact that the vertex peak position in the 94 data taking period was displaced some 5 cm from the nominal value.

4.1.5 The cut in $\sum_i (E_i - p_{z,i})$

A calculation of four-momentum conservation yield the following relation where the sum runs over the calorimetric energies in the detector:

$$\sum_i (E_i - p_{z,i}) = 2E_{el.}$$

In eq. (4.2) the calculation is shown in the simple case of a lowest order process:

$$\sum_i (E_i - p_{z,i}) = p'_{e_0} + p'_{q_0} - p'_{e_3} - p'_{q_3} = E'_e + (xE_p + E_e - E'_e) \qquad (4.2)$$
$$- \cos\theta_{e'} E_{e'} - (xE_p - E_e - \cos\theta_{e'} E_{e'}) = 2E_e$$

with the four-vectors, having the components (E,p_x,p_y,p_z), as seen in fig. 2.3a. The relation is based on energy and momentum conservation and is therefore valid for processes to all orders. Due to the finite detector resolution

and limited acceptance, we expect the distribution to have certain spread. The effect of initial state QED radiation will contribute to the tail of the distribution at lower $\sum_i (E_i - p_{z,i})$. For deep inelastic scattering events the

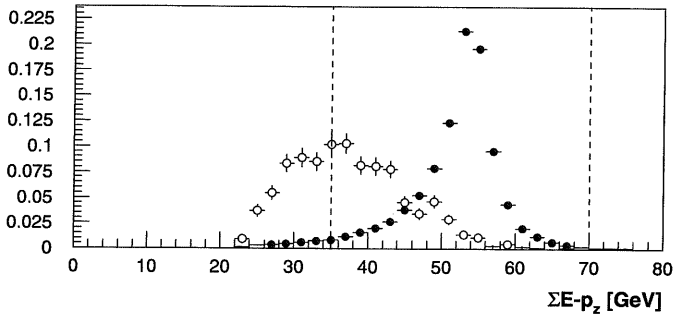

Figure 4.5: The spectrum of $\sum_i (E_i - p_{z,i})$ for photo-production events (open circles) simulated using PHOJET, and DIS as simulated with DJANGO. The distributions are normalized to unity. The vertical hatched lines indicate the cuts imposed to reduce background.

distribution is thus peaked at twice the electron beam energy, in our case $\approx$ 55 GeV. In photo-production, an electron escaping detection will decrease the sum and result in the distribution seen in 4.5 (open circles). The imposed cut of:

$$35 < \sum_i (E_i - p_{z,i}) < 70 \text{ GeV}$$

will thus effectively reduce the photo-production background, as well as reducing the number of events with initial state QED radiation.

4.1.6 The BEMC module cut

The inner modules of the BEMC (see fig. 4.6) suffer from difficulties reconstructing the energy of the scattered electron since in this region energy can leak out through the edge of the detector. The events with an electron hitting the BPC corresponding to a cluster center of gravity in the inner part of the BEMC seen in fig. 4.6, are therefore removed from the sample. The cut applied is defined by:

$$\min(|x_{BPC}|, |y_{BPC}|) > 16 \text{ cm}, \sqrt{x_{BPC}^2 + y_{BPC}^2} > 18 \text{ cm}$$

4.1.7 Further requirements, phase space definition

The phase space of deep inelastic scattering studied in this analysis is basically given by the acceptance of the BEMC and the cuts on the scattered

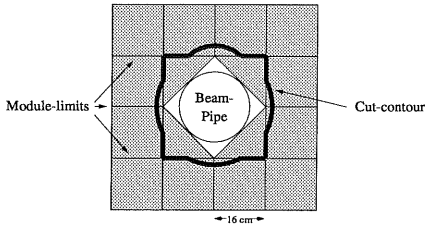

Figure 4.6: The inner region of the BEMC is a difficult region when it comes to reconstructing the energy of the electron, why a cut on the position of the electron in the BPC, as indicated by the black line, is imposed.

x–Bin	Bin limits
1	$10^{-4} < x < 2,5 \times 10^{-4}$
2	$2,5 \times 10^{-4} < x < 5 \times 10^{-4}$
3	$5 \times 10^{-4} < x < 10^{-3}$
4	$10^{-3} < x < 2,5 \times 10^{-3}$
5	$2,5 \times 10^{-3} < x < 5 \times 10^{-3}$
6	$5 \times 10^{-3} < x < 10^{-2}$

Q^2–Bin	Bin limits
1	$5\ \mathrm{GeV}^2 < Q^2 < 11\ \mathrm{GeV}^2$
2	$11\ \mathrm{GeV}^2 < Q^2 < 15\ \mathrm{GeV}^2$
3	$15\ \mathrm{GeV}^2 < Q^2 < 20\ \mathrm{GeV}^2$
4	$20\ \mathrm{GeV}^2 < Q^2 < 30\ \mathrm{GeV}^2$
5	$30\ \mathrm{GeV}^2 < Q^2 < 50\ \mathrm{GeV}^2$
6	$50\ \mathrm{GeV}^2 < Q^2 < 100\ \mathrm{GeV}^2$

Table 4.1: *The binning of the kinematic plane in x and Q^2.*

electron which defines the ranges for the kinematic variables in eq. (2.1-2.3). The final cuts imposed on the electron variables are:

$$156^o < \theta_e < 173^o$$

$$\mathrm{y} > 0.05$$

The angular cut slightly reduces the ϕ-asymmetry (see fig. 4.6) of the cut introduced in the last section for electrons stemming from the nominal vertex position. The cut in y, where y is the Bjorken scaling variable of eq. (2.3), is imposed to ensure a reasonable resolution in the measurement of the electron energy and hence a good reconstruction of the kinematic variables. The resulting phase space of this analysis can be seen in fig. 4.7.

4.2 Jet finding and selection

The jet reconstruction algorithm used was the CDF-Cone algorithm [24] (a more detailed description can be found in section 5.1.1). The experimental finding of a jet starts with the search for hadronic clusters in the calorimeter. Such a cluster serves as a *seed* for a jet, defining the direction in of a *protojet* in the pseudo-rapidity and phi space, where the pseudo-rapidity is calculated from the polar angle of the protojet according to:

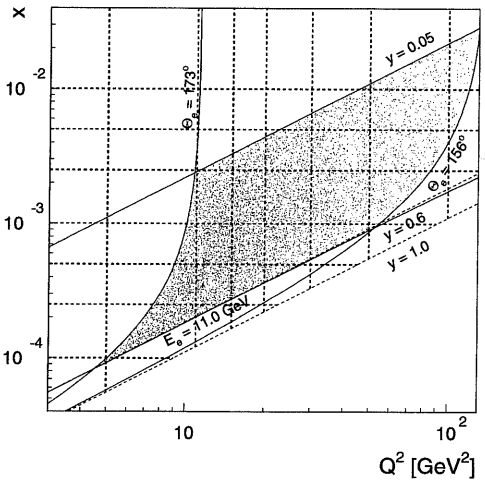

Figure 4.7: The limits of the kinematic plane as defined by the cuts imposed on the scattered electron. The dashed lines define the bins in x_{Bj} and Q^2 (see table 4.1).

$$\eta = - \ln(\tan(\theta/2))$$

In the hadronic center of mass system, the pseudo-rapidity is written; η^*. Around each seed (protojet) a cone of a specified radius R in (η, ϕ) space is defined, and the sum of the transverse momenta from all clusters inside this cone is calculated. Now a new protojet direction is defined by the momentum center of gravity of the clusters in the cone, and a new cone is defined around this direction. The procedure continues until the direction of the protojet does not change between two steps in the iteration. The list of stable protojets is then reduced by applying a cut on the minimum transverse momenta inside of the jet-cone. If any of the jets overlap, the maximum allowed overlap fraction of transverse momenta in order to define two separate jets is 75%. If the overlap is greater, the jet with the least transverse momentum is removed. The jet finding was performed in the hadronic center of mass frame using three different scenarios for the minimum value of the transverse momenta, p_t, of the jets. In the so called *symmetric* scenario, the minimum value of the p_t of both jets was 5 GeV. For reasons explained in section 4.3 two other cut-scenarios were studied:

$$\mathrm{p}_{t,max} > 7 \text{ GeV}, \ \mathrm{p}_{t,min} > 5 \text{ GeV}.$$

$$\Sigma_{jets} \ \mathrm{p}_t > 13 \text{ GeV}, \ \mathrm{p}_{t,min} > 5 \text{ GeV}.$$

referred to as the *asymmetric* and *sum* scenarios. The objects that the algorithm used as input was for data combined objects, consisting of a combination of hadronic clusters from the calorimeters and the corresponding tracks from the tracking system. When run over Monte Carlo events, the input was hadrons at hadron level, and combined objects at detector level. The electron was excluded in the jet finding procedure.

The 2-jet sample

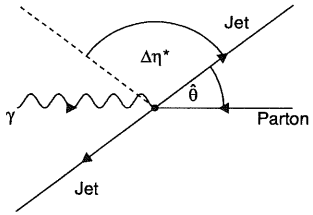

Figure 4.8: The cut in pseudo-rapidity separates the outgoing partons from the proton remnant direction.

In order to avoid the region in the forward direction where initial state QCD radiation might cause problems for the jet reconstruction, a cut on the pseudo-rapidity of the jets in the events, passing the criteria of the last section, was applied as seen in fig. 4.8:

$$|\Delta\eta^*| < 2$$

In a first order approximation this corresponds to an angular cut $|\cos\theta| < 0.76$ where θ is the angle between the incoming and outgoing partons in the photon-parton rest frame.

4.3 Next To Leading Order Calculations

In next to leading order in α_s the process includes two gluon vertices, and the number of diagrams possible is much larger than in leading order. The calculation of the matrix elements is therefore a bigger task than in LO. The NLO calculation programs like DISENT [25] and JETVIP [26] provide us with the inclusive as well as the di-jet cross sections on parton level. The generated partons define the final state as they are not hadronized. A first comparisons between the NLO calculations and the measured di-jet rate does not look very satisfying as the di-jet rate in data overshoot the NLO predictions well outside the errors. As it turns out this is the expected result

of a NLO calculation where the phase space of two jets having almost the same transverse momentum is included. The calculations in this part of phase space suffer from infrared sensitivity when there is no phase space for the emission of a third real parton. Hence, the cancellation between real and virtual corrections in this region is incomplete, and could lead to negative cross sections as seen in fig. 4.10. The problem is illustrated in fig. 4.9. If

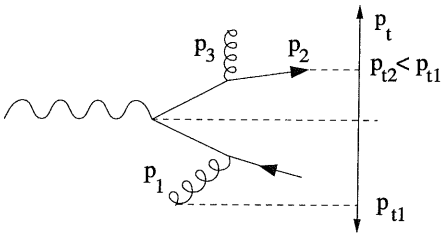

Figure 4.9: In the NLO region of phase space where the p_t of the two hardest partons is balanced, the emission of a third parton can decrease the p_t of the emitting parton below the cut-off value used to define a di-jet event.

the cut on the jet p_t is equal to p_{t_1} then the emission of a second soft gluon can bring down the p_t of the second parton that would balance the p_t of p_1 in leading order. If the angle between the soft gluon p_3 and p_2 is large, it will not be covered by the cone defining the jet of p_2, hence the event will not fulfill the requirement of having two jets with $p_t > p_{t_1}$. Reliable calculations would have to include the resummation to all orders in α_s to get rid of the residual effect of the negative contributions from the virtual corrections of higher orders. The solution when comparing data to NLO calculations is to make a phase space cut, excluding most part of the problematic region. This was done in two slightly different ways. In the first, a cut on the jet with the highest p_t was added, now requiring the jets to have $p_t > 5$ and 7 GeV respectively. In the other scenario the sum of the jet p_t was required to be larger than 13 GeV, with a minimum p_t of 5 GeV. The two scenarios effectively cuts out most of the problematic phase space as seen in fig. 4.10, and fulfills the recommendation in [27].

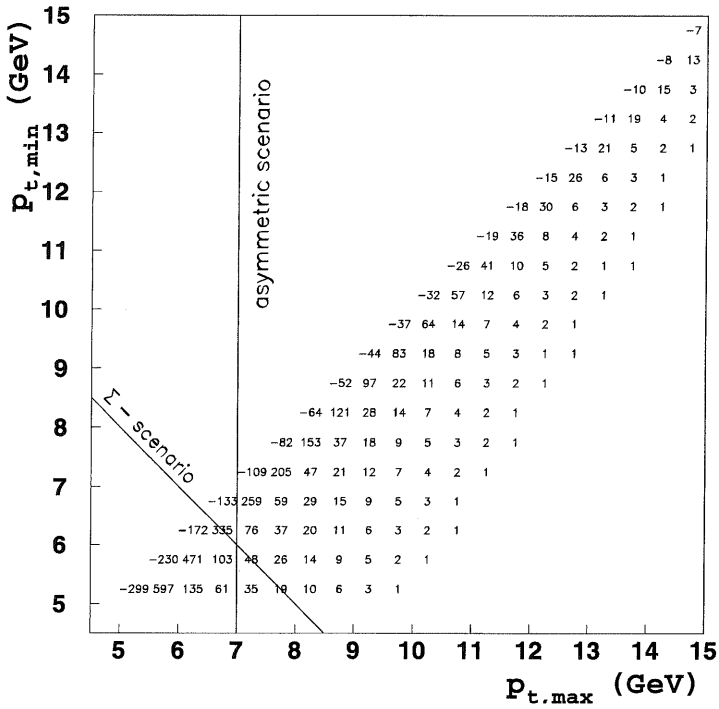

Figure 4.10: The cross section of di-jet events calculated in NLO with DISENT, as a function of the p_t of the jets reconstructed using the CONE algorithm. A minimum p_t cut of 5 GeV was applied. The lines shows the cuts imposed to remove the main part of the infrared sensitive region having large negative contributions. The overall normalization is not relevant.

4.4 The 2-jet rate

The rate of di-jet events is measured in six bins of x_{Bj} and Q^2 as seen in table 4.1 and fig. 4.7. The binning ensures enough statistics to limit the statistical error to $\lesssim 5\%$ in each bin from the di-jet sample. The raw jet rate, R_2^{raw}, in

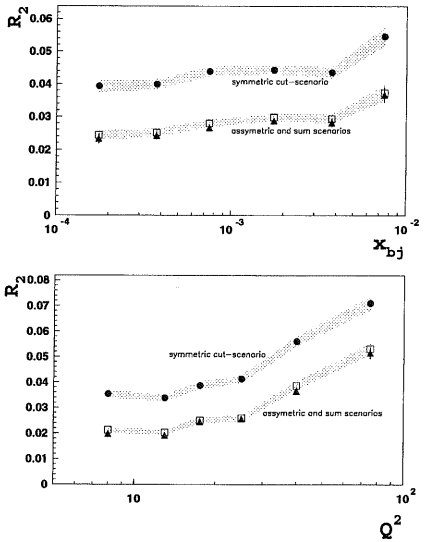

Figure 4.11: The uncorrected di-jet rate at as a function of x_{Bj} and Q^2 for the three different cut-scenarios defined in section 4.2. Black circles are the data points for the symmetric scenario, while the squares are the asymmetric scenario data, and the triangles are the sum scenario data points. The shaded band shows the statistical error for the symmetric and asymmetric scenarios.

a certain bin i on detector level, is defined as the rate between the number of di-jet events found, N_{2,x_i}^{raw}, and the total number of events in the DIS sample, N_{o,x_i}^{raw}, in this bin.

$$R_2^{raw}(x_i) = \frac{N_{2,x_i}^{raw}}{N_{o,x_i}^{raw}}, \quad R_2^{raw}(Q_i^2) = \frac{N_{2,Q_i^2}^{raw}}{N_{o,Q_i^2}^{raw}} \tag{4.3}$$

The results for the three different cut-scenarios in bins of x_{Bj} and Q^2 can be seen in fig. 4.11.

4.5 Data corrections

The raw data result is heavily dependent on the limited acceptance and efficiency of the detector, and the effects from QED radiation. The value of the jet rate as defined by our selection criteria would be directly obtained from the measurements provided the detector would have 4π coverage and would be 100% efficient. The data thus has to be corrected for the detector effects and the QED radiation in order to compare it with the predictions of the theory at the hadron level. The corrections are made using Monte Carlo generated events passing through the H1 detector simulation and event reconstruction. The full correctional formula is defined as follows:

$$R_2 = \frac{N_2^{raw} - N_2^{\gamma p}}{N_0^{raw} - N_0^{\gamma p}} C_{eff/acc} C_{rad} C_{add} \tag{4.4}$$

where N_2^{raw} and N_0^{raw} are the numbers of di-jet events found and the total number of DIS events, while $N_2^{\gamma p}$ and $N_0^{\gamma p}$ are the corresponding quantities for the photo-production sample. The number of photo-production background events corresponding to the same luminosity as the data, $N_2^{\gamma p}$,$N_0^{\gamma p}$ is estimated and subtracted using the Monte Carlo generator PHOJET [28]. The effect of the photo-production background on the di-jet rate is insignificant except in the lowest Q^2 bin and the two lowest x_{Bj} bins where the rate is increased by $\approx$10% in the symmetric scenario. The other correction factors are: $C_{eff/acc}$, which takes the non-perfect acceptance and efficiency of the detector into account, C_{rad}, the correction for the effect of QED radiation, and C_{add}, which takes into account the non-perfect description of the jet pseudo-rapidity by the Monte Carlo. In the following sections these factors will be described in more detail.

4.5.1 The acceptance and efficiency correction

The correction factor which takes the non-perfect acceptance and efficiency of the detector into account, is calculated using detector-simulated Monte Carlo generated events from the LEPTO [29], ARIADNE [30] and DJANGO [31] MC models without QED radiation. LEPTO uses parton showers for the higher order QCD emissions, while ARIADNE uses color dipole emission (CDM). ARIADNE uses LEPTO to calculate the kinematic variables. DJANGO provides an interface between the programs LEPTO and HERACLES, providing final states in e-p collisions including both QED and QCD radiative effects. The use of HERACLES allows us to take into account the complete one-loop electro-weak radiative corrections and radiative scattering. DJANGO was used with ARIADNE providing higher order color dipole QCD emissions. The definition of the correction factor is as follows:

$$C_{eff/acc} = \frac{R_2^{Had}}{R_2^{Det}} = \frac{N_2^{Had}}{N_2^{Det}} \frac{N_0^{Det}}{N_0^{Had}} \tag{4.5}$$

where N_2^{Had} is the number of di-jet events found on hadron level, and N_0^{Det} is the total number of DIS events found at detector level etc. The correction factors for the five Monte Carlo samples can be seen in fig. 4.12. The final

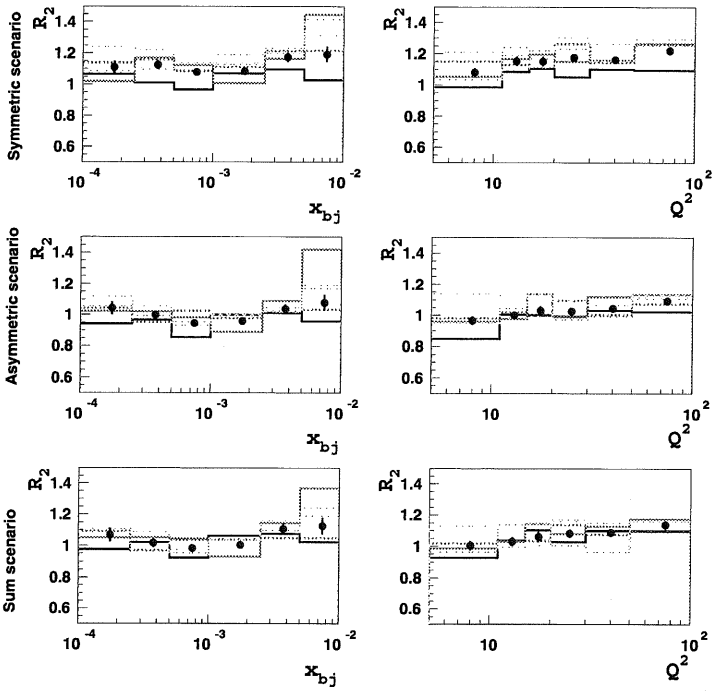

Figure 4.12: Acceptance/efficiency correction factors from the different Monte Carlo samples. Full black line - LEPTO 6.4, full gray (red) line - LEPTO 6.5, dashed line - ARIADNE (LEPTO 6.4), dotted line - ARIADNE (LEPTO 6.5), dash-dotted - DJANGO 6.2 (ARIADNE). The black dots show the resulting weighted mean correction factors.

correction factor is the mean value of the individual Monte Carlo program correction factors in each bin, weighted according to the statistical significance of the samples. The corrections generally increase the jet rate by some 10-20% for the symmetric scenario while for the asymmetric and sum scenarios the corrections are in the order of a few percents. A comment on the statistical error resulting from this correction can be found in app. B.

4.5.2 The correction for QED radiation

Initial state QED radiation will proceed in the direction of the incoming electron, and will thus escape detection. The radiation will reduce the energy of the electron. Hence the values of the kinematic variables in equations 2.1-2.3 will be shifted since they are determined from the energy of the incident electron, and the energy and angle of the scattered electron. To correct for this we apply a correction factor obtained from MC samples using DJANGO with and without QED initial and final state radiation. A photon radiated collinear to the electron in the final state will be detected together with the scattered electron in the BEMC and will not decrease the energy of the final state electron as measured by our detector. Since the collinear direction of radiation is favored, the effect on the kinematic variables from the final state QED radiation is smaller, but still corrected for. The correction factor is defined as follows:

$$C_{rad} = \frac{R_{2,Det}^{Non-rad}}{R_{2,Det}^{Rad}} \tag{4.6}$$

The resulting corrections for the different bins can be seen in fig. 4.13. Since, within the statistical errors, there is no dependence on x_{Bj} or Q^2, the mean value in the six bins was applied as a global correction. For the symmetric scenario the correction applied was 1.06 for both the x_{Bj} and Q^2 dependencies. For the asymmetric and sum scenarios the corresponding correction factor applied was ≈ 1.08. If we multiply the correction factors for acceptance/efficiency and QED radiation with the photo-production subtracted raw data we now get the following jet rate:

$$R_{2,DIS}^{raw} \cdot C_{rad} \cdot C_{acc/eff} = R_{2,DIS}^{raw} \frac{R_{2,Det}^{Non-rad}}{R_{2,Det}^{Rad}} \frac{R_{2,Had}^{Non-rad}}{R_{2,Det}^{Non-rad}} = \tag{4.7}$$

$$R_{2,DIS}^{raw} \cdot \frac{R_{2,Had}^{Non-rad}}{R_{2,Det}^{Rad}} = R_{2,Had}^{Corr,Non-rad}$$

which is the corrected jet rate at hadron level.

4.5.3 The Pseudorapidity Correction

The bin-wise correction procedure is only justified if the relevant jet properties, sensitive to detector effects, are well described by the simulated Monte Carlo events. As seen in fig. 4.14 the description by MC simulated events of the basic jet-observables is good except when it comes to the pseudo-rapidity η^*. The jets in the data sample are generally more forward than what is seen in the simulated events. Since the efficiency of the jet reconstruction is lower in the backward region this will lead to an overestimated value of the $C_{acc/eff}$ correction factor defined in eq. 4.5 as the denominator decreases. To account for this effect an additional correction factor C_{add} is applied. This correction, as calculated by DJANGO and LEPTO MC models, decreases the di-jet rate

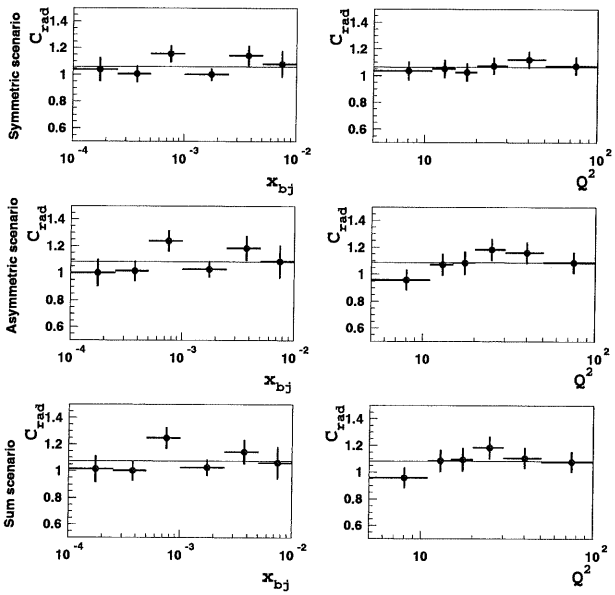

Figure 4.13: The radiative corrections for the different p_t-cut scenarios. As there is no real dependence on x_{Bj} or Q^2, and since in most bins the mean value of the correction, marked by a solid line, lies within the errors, the mean value of the correction was used as a global correction.

in the symmetric scenario by some 10%, in the lowest x_{Bj} and Q^2 bins, and around 1% for the highest bins. In the asymmetric and sum scenario the correction is about half of that applied for the symmetric scenario.

4.6 Systematic Errors

There are several sources of systematic errors. The largest systematic error comes from the uncertainty in the calibration of the hadronic liquid argon calorimeter, which corresponds to an energy uncertainty of $\pm 4\%$. By changing the energy-scale of the liquid argon calorimeter by $\pm 4\%$ we take this uncertainty into account in the estimation of the systematic error. Since there is no dependence on x_{Bj} or Q^2, the mean values fitted over x_{Bj} and Q^2 are taken as the global systematic errors seen in table 4.2. The systematic error

Systematic Errors from LAr energy scale ±4%

	symmetric scenario		asymmetric scenario		sum scenario	
scale	x	Q^2	x	Q^2	x	Q^2
+4%	+10%	+9%	+11%	+11%	+11%	+10%
-4%	-7%	-8%	-7%	-7%	-7%	-8%

Table 4.2: The change in the di-jet rate as an effect of the uncertainty in the energy-scale of the liquid argon calorimeter by ±4%. The numbers are added as global systematic errors.

from the 1% uncertainty of the energy scale of the BEMC has a dependence on x_{Bj} why it was decided to add this systematic error bin by bin as seen in fig. 4.15. The values of the errors are quite similar in all three scenarios. The statistical uncertainty of the correction for QED radiation is also taken as a systematic error that amounts to 3% in all scenarios for both x_{Bj} and Q^2.

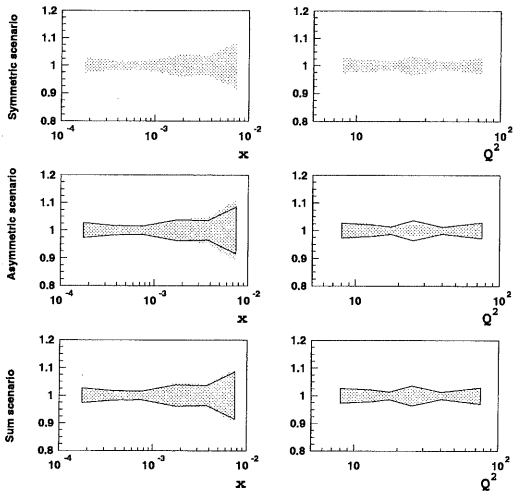

Figure 4.15: The systematic errors from the ±1% uncertainty of the BEMC energy scale. The solid line is the symmetric scenario errors as reference.

The acceptance and efficiency correction factors obtained using different MC generators are shown in fig. 4.12. Its variation is an estimate of how the result depends on the MC model used, and is included into the systematic error. The difference in the calculation of the C_{add} using the two different MC samples is also added as a systematic error that amounts to 1-2% for the symmetric scenario, and significantly less for the asymmetric and sum scenarios. The final values of the bin-to-bin systematic errors can be found in table 1 in appendix A.

4.7 Results

The di-jet rate corrected for detector effects and QED radiation can be seen in fig. 4.16. The ARIADNE program with its Color Dipole concept describes data very well. However, the model dependence of this result is relatively large, since a variation of the parameters describing the photon and proton size (see section 2.2.3) within reasonable limits will lead to rather large changes of the resulting di-jet rate. We also conclude that the simple matrix element with added parton showers (RAPGAP "DIR") which corresponds to the interaction with a point-like photon, does not describe data in any of the three scenarios. However, when we include the possibility of resolving the partons in the photon (RAPGAP "DIR+RES"), as described in section 2.2.4, we open up a new region of phase space, resulting in an increased di-jet rate now describing the data. These results are relatively stable when it comes to changing internal parameters of the model. It should be noted that the resolved photon picture is similar to the CDM picture with only one breaking of the k_t ladder. In figure 4.17 the data is compared to the NLO calculations with a point-like photon (NLO "DIR"), for the asymmetric and sum scenarios. Since the calculation of the NLO di-jet cross section in the symmetric scenario is not safe, the results of these calculations are not included. However we conclude that the NLO calculation of the di-jet rate in the asymmetric and sum scenarios describes data both as a function of x_{Bj} and Q^2. In the JETVIP program there is an additional possibility of calculating the NLO cross section contribution of resolved photons (NLO "DIR+RES"). In this case the virtual photon structure is parametrized and the direct splitting of the photon into a quark and anti-quark (PSP) is included in the virtual photon structure function, why this has to be subtracted in the NLO calculation to avoid double counting. The real resolved component is then added (NLO "DIR-PSP+RES"). The theoretical uncertainties of the NLO calculations stem from the uncertainty of the in principle unknown factorization and renormalization scales μ_f and μ_r. As seen in section 5.5.4 a change of a factor four of these parameters yield a change of the di-jet rate around 20%, compared to the nominal scale (Q^2+50 GeV^2) for JETVIP. As shown in [32] the uncertainties are decreased by choosing the renormalization scale μ_r=p_t^2 (in DISENT) instead of using Q^2. The effect of hadronization, as estimated from ME+PS and CDM studies, is expected to be ~10-20%, the di-jet rate being slightly higher on the parton level compared to that on the hadron level.

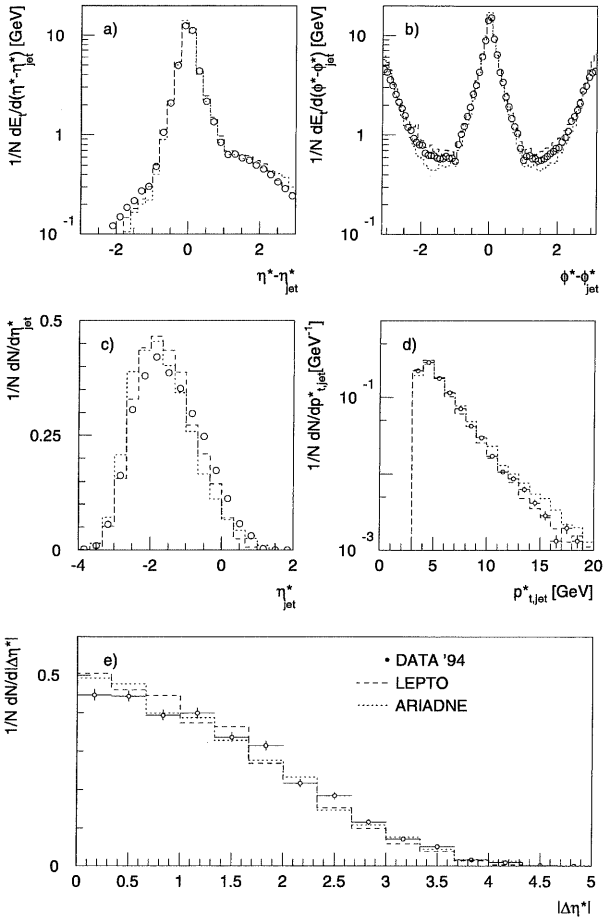

Figure 4.14: Comparisons between data and MC predictions from LEPTO (dashed) and ARIADNE (dotted), for some basic jet properties. The transverse flow of energy, as a function of: a) the pseudo-rapidity distance from the jet, $\eta^* - \eta^*_{jet}$, b) the azimuthal angle difference from the jet, $\phi^* - \phi^*_{jet}$. In fig. c) and d) the pseudo-rapidity and p_t spectra are shown. In e) the absolute difference in η^* between the two jets is shown.

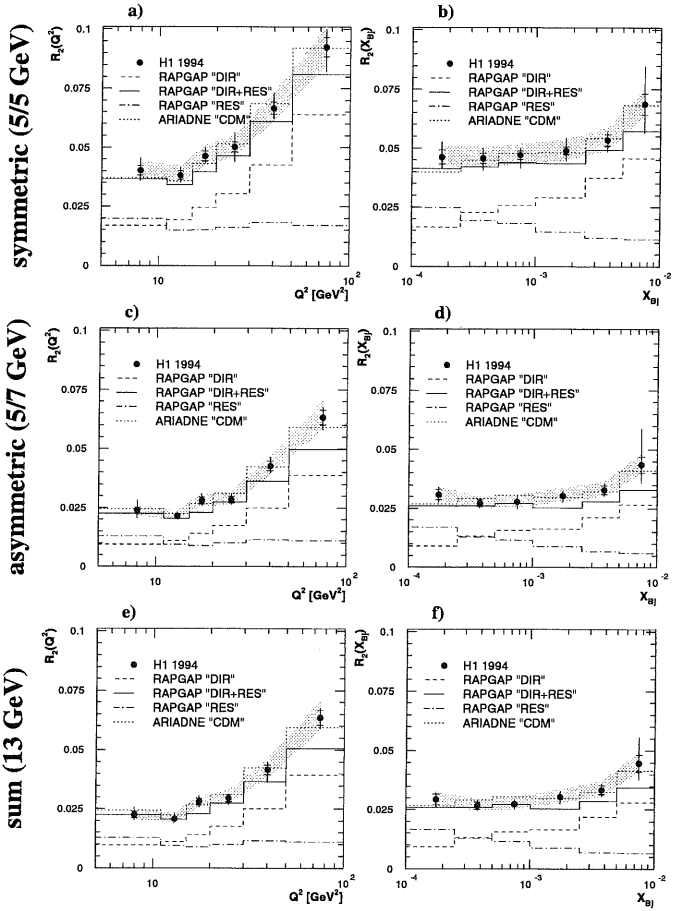

Figure 4.16: The di-jet rate as a function of Q^2 (a,c,e) and x_{Bj} (b,d,f) compared to various MC predictions. The inner error bars mark the statistical errors only, while the full error bars mark the quadratic sum of the statistic and systematic errors discussed in section 4.6. The shaded area shows the global systematic errors from the uncertainties of the energy scale of the hadronic calorimeter and the uncertainty in the radiative correction. The statistical errors of the MC predictions are smaller than for the data.

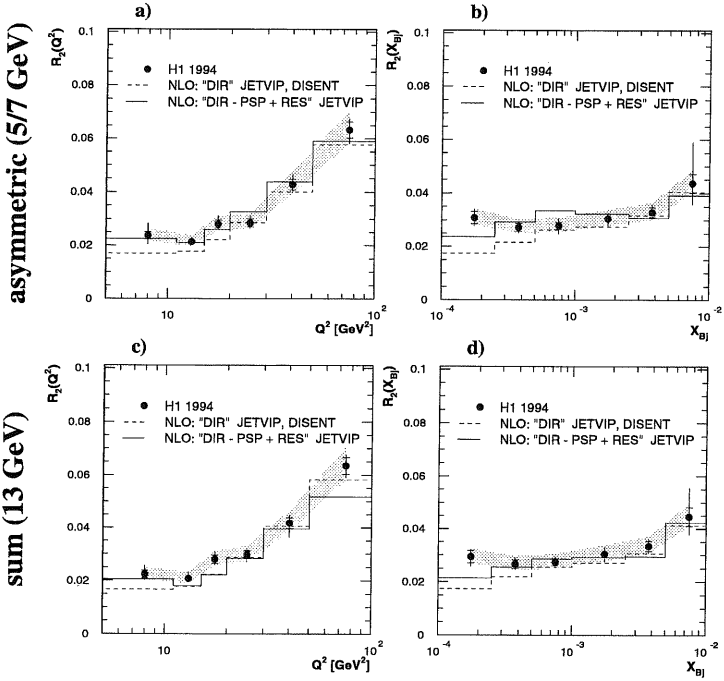

Figure 4.17: The di-jet rate as a function of Q^2 (a,c) and x_{Bj} (b,d) for the asymmetric and sum scenarios, compared to the NLO calculations by the DISENT and JETVIP programs.

4.8 Conclusions

The analysis of the di-jet rate has improved our knowledge of perturbative QCD and its limitations in deep inelastic scattering . We now know that the virtual photon cannot always be treated as a point-like object to be able to describe the data. The breaking of the strong ordering in the DGLAP evolution, introduced via the resolved photon mechanism, is similar to the situation of the CDM model. The introduction of an additional cut on the jet p_t in the NLO calculation makes the results reliable and leads to agreement between the prediction and data. In total, around 4% of the events in the kinematic region studied include the emission of two partons having transverse momenta of $p_t \geq 5$ GeV. This result is fully described by the Monte Carlo approaches that includes the possibility to break the ordering in the gluon chain. Adding further requirements on the p_t's of the jets in order to avoid divergency problems, data is also described by the NLO calculations as well as the different MC approaches.

Chapter 5

Jet Algorithm Analysis

In particle physics we are faced with the problem of comparing theoretical calculations, which reflects our understanding of the physics of highly energetic particle collisions, to actual measurements. At the present stage, in QCD there is no possibility of calculating, from first principles, the exact configuration of the multi-particle final state, event by event. The perturbative calculations of cross-sections become unstable in the limit of low energy, as the probability of emitting gluons (especially collinear and soft gluons) increases as the strong coupling constant α_s becomes large. Only for observables like the total cross section, these divergencies will cancel out in the perturbative calculations. Such observables, insensitive to whether particles split into two collinear particles, or emit soft particles at low energy (soft) scales, are called "infra-red" safe observables. An example of such a variable is a jet, which is defined as a collimated flow of particles in space. If a jet has a sufficient amount of transverse momentum (p_t) it becomes well defined as particles resulting from the hadronization of the original partons in the hard sub-process. The main property of the jet concept is that a measurement of

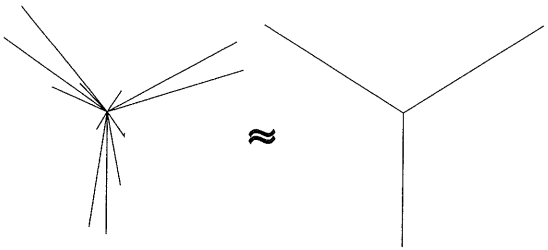

Figure 5.1: The approximate equivalence between the three jets as found by the infrared-safe measurement of jets, and the underlying partons of perturbative QCD.

physical particles (as manifested in the detector) will give approximately the same result as if we would replace the hadrons with the underlying partons as illustrated in fig. 5.1. This, i.e. the infra-red safety of the measurement of jets, is equivalent to the statement that the observable is independent of activity taking place long time after the underlying hard interaction [33].

The main aim of this chapter is to check, for the various reconstruction schemes, how well the reconstructed jets describe the properties of the underlying partons from the exact calculations of the first order QCD matrix elements. That a measurement of the parton and final state of hadrons will only give approximately the same result is because of smearing from the higher order QCD radiation and hadronization of partons into the final state particles. The size of the hadronization effect will be studied by comparing jets in the partonic final state (ME+PS) with those at hadron level. We require that the result of measurements on the hadronic and partonic final

state should not differ to much even though the color force in the fragmentation [18] effects the distribution and properties of the final state particles. Even if this pure hadronization correction is small, this does not exclude the possibility that the algorithm makes the same mistake at both levels, giving a false impression of the algorithms performance, why we also compare the final state jet properties with the matrix element partons.

A more rigorous description of the variables studied is presented in section 5.4. In short it can be said that the aim of this analysis is to investigate the errors introduced by the use of a jet algorithm.

Given the final state of particles, either at the level of hadrons (or partons), or at detector level, how do we reconstruct a jet? In section 5.1 the different jet reconstruction algorithms will be introduced. Readers familiar with DIS may skip section 5.2 where the basic physics of DIS will be introduced. In section 5.3 we discuss the way of selecting and generating the events used. Section 5.4 includes the definition of the variables used to investigate the properties of the jet reconstruction. In section 5.5 the essential results will be discussed, and conclusions will be drawn in section 5.6.

5.1 Jet Algorithms

The perhaps most obvious definition of particle jets is that used in the CONE concept [34]. The individual particle momenta inside a cone of radius R are vectorially added, and combined into one object (compare with fig. 5.1). The different approaches used in cluster-type algorithms such as the JADE algorithm [35], recombine pairs of particles with the smallest distance into a new object. The various jet algorithms of this type differ by the respective way of measuring the distance, and the recombination scheme, i.e. the procedure of joining the proto-jet four-momenta. The process is iterative and will continue until all remaining pairs of particles (objects) have an invariant mass larger than some cut-off scale. The concept of cluster algorithms has been refined, and several variants of algorithms have been developed and later adapted to DIS physics.

In general, all jet algorithms use of a cut-off parameter to separate the hard physics from the soft, ensuring the infra-red safety as discussed above. Changing this parameter will lead to an increase or decrease of the mean number of jets found.

We have selected five of these algorithms available for DIS physics for a more detailed investigation: the CDF-cone [24], the Inclusive k_t, [36], the DURHAM-k_t, [37], the JADE [35] and the LUCLUS [38] algorithms. In the following more rigorous description of the algorithms, the term "proto-jet" refers to any object in the algorithm procedure. This is basically a set of four-vectors and could be defined by either energy deposited in calorimeter cells, momenta of hadrons measured in the tracking system, or four-vectors from earlier steps in the iterative clustering procedure.

5.1.1 The CONE algorithm

In the CDF cone algorithm [24] a jet is defined as a set of particles within a cone of some fixed radius, R, defined in rapidity-phi (η,ϕ) space.

$$R = \sqrt{\Delta\eta^2 + \Delta\phi^2} \tag{5.1}$$

The central axis of the cone, defining the jet direction, is expected to coincide with the momentum sum of the particles included. The procedure is iterative, starting with all particles as seeds for jets, calculating the sum of transverse momenta inside a cone centered around each particle: If the jet direction found (the momentum center of gravity) is not the same as the direction of the seed, the procedure is iterated with the momentum sum direction as seed of a new cone. After reaching a stable configuration the resulting jet direction is added to a list of proto-jets. Sometimes two local maxima, separated by an angular distance between R and $2R$, could be identified as independent jets by mistake inside a broad highly energetic jet. To prevent this, the bisecting direction of these proto-jets is taken as seed for a possible proto-jet, and thus complete the list of proto-jets. Next, all proto-jets with transverse momenta less than some user defined cut-off are rejected. In the last step particles assigned to more than one proto-jet are reassigned so as to ensure that no particle is contained in more than one jet. This procedure [36] includes the rejection of low energy proto-jets partially included in higher energy proto-jets.

5.1.2 The JADE algorithm

The JADE algorithm [35, 39] is a typical example of an algorithm that uses the scheme of joining pairs of primary proto-jets to secondary proto-jets in an iterative manner. The classical scheme is to calculate a distance measure d_{ij} for every pair of proto-jets and then join the pair with the smallest d_{ij} into a single proto-jet recombining their four-momenta. In DIS the presence of the very energetic spectator beam-remnant jet is handled by the inclusion of a pseudo particle which takes the missing longitudinal momentum normally lost in the beam pipe. In each iterative step it is then tested whether a particle should be clustered into the pseudo-particle (beam-jet), or to any other proto-jet, by calculating the appropriate distance measure. In the JADE algorithm the measure of distance used is the approximated scaled invariant mass:

$$y_{ij} = \frac{d_{ij}^2}{W^2} = \frac{2E_iE_j}{W^2}(1 - \cos\theta_{ij}) \tag{5.2}$$

where E_i and E_j are the energies of proto-jets i and j and θ_{ij} is the angle between them. The normalization to the invariant mass of the hadronic final state is one of the main characteristics of the JADE algorithm. The pair of particles having the smallest distance measure is joined by simply adding their four-momenta, the so called E recombination scheme [40]. The

clustering procedure is stopped whenever the smallest distance between pairs of proto-jets is larger than some predefined cut-off scale y_{cut}. The remaining proto-jets are the final state jets found by the algorithm.

5.1.3 The LUCLUS algorithm

The LUCLUS algorithm [38] uses the method of the JADE algorithm described above, but with a different distance measure d_{join} defined by:

$$d^2_{join} = \frac{2(|\bar{p}_i||\bar{p}_j| - \bar{p}_i \cdot \bar{p}_j)|\bar{p}_i||\bar{p}_j|}{(|\bar{p}_i| + |\bar{p}_j|)^2} = \frac{2|\bar{p}_i|^2|\bar{p}_j|^2(1-\cos\theta_{ij})}{(|\bar{p}_i| + |\bar{p}_j|)^2} \tag{5.3}$$

where $\bar{p}_i$ and $\bar{p}_j$ are the 3-momenta of proto-jets i and j. In the region of small angles d_{join}, can be interpreted as the transverse momenta of proto-jet i or j with respect to the direction given by the sum of $\bar{p}_i$ and $\bar{p}_j$. One significant difference compared to the JADE algorithm is that the LUCLUS distance measure is not a dimensionless quantity. In LUCLUS there is also the possibility to reassign proto-jets that are closer to a different cluster than the one it was clustered into in the preceding step, and hence, after every binary joining, all particles in the event are reassigned to the closest proto-jet. In LUCLUS, the option of pre-clustering[1] of the particles is used, with a pre-clustering scale always much smaller than the d^2_{join} cut-off, why it will be of little significance to the outcome of the clustering procedure, other than speeding up the procedure.

5.1.4 The k_t algorithm

The $k_\perp$ (DURHAM) algorithm [37] for DIS is defined in the Breit frame[2] of the initial state hadron and the exchanged vector boson. The distance measure used is based on the relative transverse momenta of proto-jets.
For each proto-jet h_i in the event the scaled transverse momenta relative to the beam remnant particle, p, is calculated:

$$y_{ip} = \frac{2(1-\cos\theta_{ip})}{E_t^2} E_i^2 \tag{5.4}$$

For each pair of proto-jets h_i,h_j, the k_t of the least energetic proto-jet with respect to the other is computed:

$$y_{ij} = \frac{2(1-\cos\theta_{ij})}{E_t^2} \min(E_i^2, E_j^2) \tag{5.5}$$

where E_t^2 is a parameter to be defined by the user, tuning the number of jets found by the algorithm. If the smallest of the $\{y_{ij}, y_{ip}\}$ values is among the

[1] A "quick and dirty" method to speed up the jet finding.
[2] The frame in which the exchanged boson is at rest.

y_{ip}'s, and is larger than 1.0, the proto-jet h_i is included in the beam jet where it no longer takes part of the clustering procedure. If the smallest value is among the y_{ij}'s, h_i and h_j are clustered together into a proto-jet according to the E recombination scheme. This procedure is iterated until the minimum relative transverse momenta is smaller than E_t, or equivalently, all objects have $y_{ij}, y_{ip} > 1$. The resulting proto-jets (except the remnant jet as usual) define the final state jets found by the algorithm.

5.1.5 The Inclusive k_t algorithm

The so called *Inclusive* k_t algorithm is based on the principles suggested in [36] generalized with the inclusion of an R parameter, described below. For every proto-jet, the distance of a protojet to the proton remnant is defined as:

$$d_{ip} = p_{t_i}^2 \tag{5.6}$$

For each pair of proto-jets, the following distance is measured:

$$d_{ij} = \min(p_{ti}, p_{tj})^2 R_{ij}^2 / R^2 \tag{5.7}$$

$$R_{ij}^2 = (\eta_i - \eta_j)^2 + (\phi_i - \phi_j)^2 \tag{5.8}$$

where R_{ij}^2 is the radius in rapidity-azimuthal (η, ϕ) space, also used in the CONE algorithm described in section 5.1.1, and p_{ti} is the transverse momentum of proto-jet i. The value of $R = 1$ is fixed and we do not attempt to tune this parameter. The next step is to pick the smallest $\{d_{ip}, d_{ij}\}$. If this distance measure is in the d_{ij} sample, proto-jets i and j are merged according to the p_t-weighted scheme [36], where the p_t's of the protojets are summed and (η,ϕ) of the joined object is obtained as a p_t-weighted average of the protojet angles. If the minimum value is of the d_{ip} type then the proto-jet is closest in distance to the proton remnant, and will no longer take part of the clustering procedure. In this case it is removed from the list of proto-jets and added to the list of jets. This procedure continues until there are no proto-jets left, producing a list of jets with increasing p_t during the process. In the final step, jets with $p_t < p_{t,\min}$ are removed from the list of jets. The resulting jets are the final state event jets found by the algorithm.

5.2 Event Characteristics and Jet algorithms

The high energies at HERA probes the region of very low x_{Bj}, where a sharp rise of the proton structure function, $F_2(x, Q^2)$, is seen. This is successfully described by the conventional DGLAP scheme. However, at small x_{Bj} we expect to see the effects of new parton dynamics that can not be described by ordinary DGLAP. This effect may show up in the production of forward jets, where jets at relatively low p_t have to be reconstructed. It is of course of vital importance that these jets are reconstructed correctly, in order to establish the expected signal of new parton dynamics.

5.3 Event generation and selection

Since events with 2 jets are of primarial interest in QCD, being of first order in α_s (see fig. 2.11), we use events generated with hard partons according to the matrix element leading order calculations. The initial and final state QCD radiation is then added, and the partonic final state is hadronized leaving us with the final state of hadrons.

The matrix element calculations and the higher order QCD emissions [41] added according to the DGLAP formalism, is implemented in the Monte Carlo program RAPGAP [42] used in this analysis. RAPGAP has shown to describe DIS data at HERA to a high accuracy.

To explore the different phase space regions of interest we generated a sample of general DIS events with virtualities of $Q^2 > 5$ GeV^2 (low Q^2 sample), as well as one sample with $Q^2 > 200$ GeV^2 (high Q^2 sample). The aim of the analysis is to provide information which can be directly used in the analysis of jets in the H1 experiment. We define our phase space for the low Q^2 sample using the following cuts on the scattered electron:

- $E_e > 11\ GeV$
- $153° < \theta_e < 177.5°$
- $y_e > 0.05$

selecting electrons measured by the backward detector at H1 with a reasonable resolution in energy.

The factorization and renormalization scales were set to $Q^2 + p_t^2$ interpolating between the regions were Q^2 or p_t^2 is the dominant hard scale. Since the p_t's of the partons are larger than 2 GeV, at very low Q^2 the dominating scale in the process will be the transverse squared momentum of the parton (or jet). At higher values Q^2 will dominate since the p_t spectra of the partons is strongly peaked at the cut-off value. The Next to Leading Order (NLO) generator DISENT [25] was used to check the sensitivity of the three general types of algorithms with respect to changes of the in principle unknown factorization and renormalization scales. DISENT is not an event generator in terms of providing a full set of final state particles, but rather produces parton four-vectors to the order α_s^2. The additional effect of fragmentation is small ($\lesssim 20\%$), why even though this is not accounted for, a comparison to data and MC at hadron level is possible.

For comparison of jets on parton level and hadron level, we of course have to select events in which two jets were found on both levels. Comparing the jets on hadron level to the corresponding matrix element hard partons we use the sub-sample where two hadronic jets are reconstructed and in which two hard partons were generated. The individual jet corresponding to a certain hard parton is identified according to its value of rapidity, giving a jet which

is most forward[3] going, and the other being the most backward going. In this way we can study the behaviour of the algorithm in different hemispheres of rapidity. In some events the partons and jets are wrongly connected. To avoid this, the additional requirement is applied that the parton and jet should lie in the same ϕ-hemisphere. For low values of the parton p_t the perturbative calculations become unreliable as the matrix element calculations diverge. To take this into account we demand the reconstructed jets to have a p_t larger than the minimum p_t of the generated partons.

The only cut applied to account for the situation at a detector such as H1 used was a beam-pipe cut.

5.4 Quality Measurements

The quality of a jet algorithm is difficult to define. It depends on the specific analysis for which the algorithm is used. A jet algorithm can be applied on any set of four-vectors. In this analysis we look at jets reconstructed in the partonic and hadronic final states (see fig. 5.2). The partonic final state is defined as the partons after the radiation of initial and final state parton showers, and the hadronic final state are the resulting hadrons after fragmentation (hadronization). As discussed in the introduction, there should be a close relation between the basic jet observables and the corresponding quantities at the different levels of partons. Therefore the following criterion should be fulfilled:

1. A good reconstruction of the generated invariant mass of the hard subsystem at parton shower level.

2. A good correlation of the matrix element partons and the corresponding partonic and hadronic jet directions.

3. Small hadronization corrections on the jet directions and reconstructed invariant masses of the jets.

4. Small dependencies on the resolution parameters of the jet algorithm for the above measurements.

5. A low sensitivity to factorization and renormalization scales in NLO calculations.

The first three requirements in the list above are essential to ensure a reasonable alignment between the reconstructed jets and the underlying parton from the matrix element calculation. To investigate this, we study the mean of the absolute difference between jet quantities like the angles (η, ϕ), p_t and

[3]By definition the forward (large/positive rapidities) direction is the direction of the incident proton, and the backward (small/negative rapidities) direction is the direction of the incident electron.

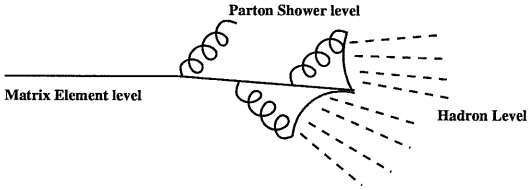

Figure 5.2: The different levels studied and compared. The matrix element partons from the perturbative calculations, the partonic final state, and the hadrons after fragmentation.

$\sqrt{\hat{s}}$, reconstructed in the partonic/hadronic final state, and the matrix element partons as seen in fig. 5.3. The results will be presented in terms of $< \Delta(\eta\phi) >$ and $< \Delta(p_t, \sqrt{\hat{s}}) >$ as defined below:

$$< \Delta(\eta\phi) >= \sqrt{< \Delta\eta >^2 + < \Delta\phi >^2} \tag{5.9}$$

$$< \Delta(p_t, \sqrt{\hat{s}}) >= \frac{< \Delta p_t > + < \Delta\sqrt{\hat{s}} >}{2} \tag{5.10}$$

where:

$$\Delta p_t = |(p_{t,parton} - p_{t,jet})/p_{t,parton}| \tag{5.11}$$

and the similar expressions for the other jet quantities (see fig. 5.3), with the exceptions that $\Delta\eta$ and $\Delta\phi$ are not normalized. The values of $< \Delta(\eta\phi) >$ and $< \Delta(p_t, \sqrt{\hat{s}}) >$ will be referred to as the ability of the algorithms to resolve the underlying structure of the events: the resolution of the algorithm. Small values of $< \Delta(\eta\phi) >$ and $< \Delta(p_t, \sqrt{\hat{s}}) >$ means a good resolution.

The systematic deviations are defined according to:

$$< \delta p_t >=< (p_{t,parton} - p_{t,jet})/p_{t,parton} > \tag{5.12}$$

and the similar expressions for the other algorithms, once again with the exceptions that $\delta\eta$ and $\delta\phi$ are not normalized. The systematic shifts in the different variables will be studied separately. An example of a systematic shift would be the effect of the color-force between the highly energetic proton remnant and the parton, pulling the jet forward.

Since these quantities exist for both jets[4] we studied them for the individual jets, but the presented result is the mean value of the two.

[4]Except for the $\sqrt{\hat{s}}$ which is a property of the pair of jets.

Setting	I	II	III	IV	V	VI	VII	VIII	IX	X
CONE	2.5	2.9	3.25	3.75	4.25	4.9	5.5	6.25	7.0	10.0
Incl. k_t	2.0	2.25	2.5	3.13	3.75	4.4	5.0	5.75	6.5	10.0
k_t	3.3	3.6	3.9	4.4	4.7	5.4	5.9	6.5	7.1	9.5
JADE	0.013	0.015	0.022	0.026	0.030	0.034	0.042	0.046	0.050	0.070
LUCLUS	4.0	4.25	4.5	5.0	5.5	6.3	7.0	7.75	8.5	10.0

Table 5.1: The different settings for the five algorithms. Higher settings gives a lower number of 2-jet events reconstructed. All resolution parameters but the dimensionless y_c parameter of the JADE algorithm are measured in GeV.

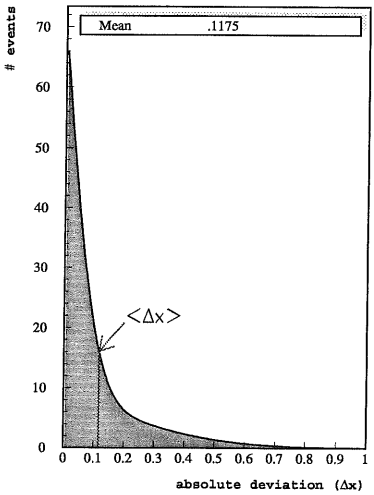

Figure 5.3: The absolute difference (Δx) between the jet quantity, x, compared on different levels. (x=p_t, $\sqrt{\hat{s}}$, η, ϕ)

We will now discuss the last two points (4-5) in the list of criterion. Due to the non perfect resolution of the detector, the values of observables measured (detector-level) will be smeared as compared to the hadron level. This smearing will introduce an additional systematic error if the algorithm is used in a region where the quality (resolution) of the jet reconstruction is strongly dependent of the cut-off parameter. An additional remark is needed concerning systematic errors when comparing data to Next to Leading Order calculations. For any finite order matrix element calculation we have to introduce the basic scales of factorization and renormalization. This could result in additional sources of systematic errors.

The requirements in the list above were studied for a wide range of the algorithm parameter settings (see table 5.1). The settings were chosen such that the 2+1 jet rates are similar for the different algorithms as shown in figure 5.4. The decrease of the 2+1 jet rate with higher settings is trivial and only reflects the increasing hardness of the jets. Evidently the ranges of parameter settings include those normally used in the algorithms.

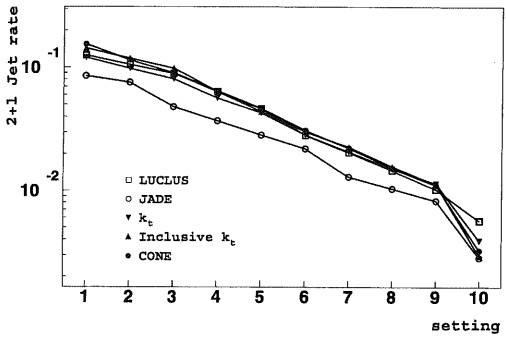

Figure 5.4: The 2+1 jet rate at hadron level as a function of the setting used in the algorithm seen in table 5.1. The settings were chosen to produce similar rates for the different algorithms. The definitions of the algorithms' different cut-off schemes can be found in sections 5.1.1-5.1.5.

5.5 Performance Results

Using the performance measures described in eq. (5.9, 5.10), we start with a study of the reconstruction of properties like invariant mass, described in points 1-3 in the list of the previous chapter. The values of these performance measures should be small, indicating a close relation between the measured jet quantities and the corresponding quantities of the underlying partons from the matrix elements. Section 5.5.1 presents the result of a study of reconstructed jet properties without hadronization effects. This will reveal effects caused by the algorithm itself. In section 5.5.2 we will include hadronization and compare the jet quantities reconstructed at hadron level with those reconstructed in the partonic final state. The fragmentation might effect the reconstruction of the jet direction. However, if we are interested in jets as a representation of the underlying partons, an algorithm which is less sensitive to the effects of hadronization is preferred, even if it will decrease the resolution of the jet algorithm compared to the resolution at parton level. In sections 5.5.3-5.5.4 we discuss the effects of detector smearing and the scale sensitivity in NLO calculations (points 4-5 in the list of chapter 5.4). First a general remark: In figure 5.5 the mean of the absolute deviation $< \Delta(p_t, \sqrt{\hat{s}}) >$, comparing the reconstructed jets at hadron level and the matrix element partons, is plotted as a function of the algorithm setting. Here we applied a cut on the p_t of the matrix element partons corresponding to the p_t cut for the jets applied in the CONE algorithm. As expected we see that the harder jets will have a higher resolution. However, the p_t cut

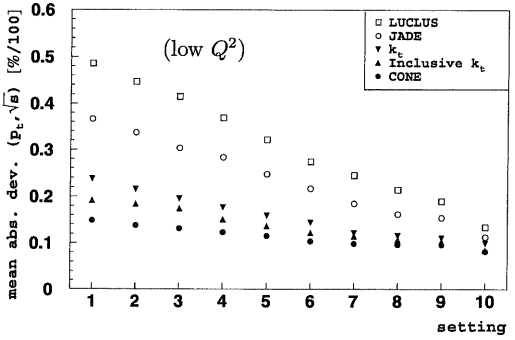

Figure 5.5: The mean absolute deviation between the matrix element partons and the corresponding jets at the hadron level for $(p_t, \sqrt{\hat{s}})$ at low Q^2, as a function of the setting used in the algorithm seen in table 5.1. Here the same cut is applied on the matrix element parton p_t as is the case for the CONE and Inclusive k_t algorithms. For the JADE, k_t and LUCLUS algorithms the p_t cuts of the CONE algorithm were used.

of the matrix element partons is not only unphysical, but cannot be applied to compare the partons with the jets from all the algorithms. Therefore this cut will not be applied in the rest of the analysis. This needs an additional remark about the results when comparing the jets to the matrix element partons. An event with two very soft matrix element partons ($p_t \gtrsim 2$ GeV) can, due to wrongly assigned partons from the showering process in the event (and also hadronization), be reconstructed as jets with significantly higher p_t. This will decrease the resolution at the higher settings, since the minimum p_t (or $\hat{s}$) of the jets increase at higher settings, while the p_t cut for the matrix element partons is constant as discussed above.

5.5.1 From Matrix Elements to Partons

The comparisons between the matrix element and the two jets found in the partonic final state can be seen as a check of the actual performance of the algorithm. Since there is no effect of hadronization involved, the partonic jets should be roughly aligned with the matrix elements partons, and the algorithms should be able to reconstruct the generated invariant mass of the underlying partons. In most cases there is only a small systematic shift (see sec. 5.4) of the jet quantities in the reconstruction, why the main contributor to the Δ measurements in equations (5.9-5.10) will be the spread (RMS) of the distributions. However there are examples, where the mean (non absolute) deviation, i.e.. the systematic shift, is large and in the order of

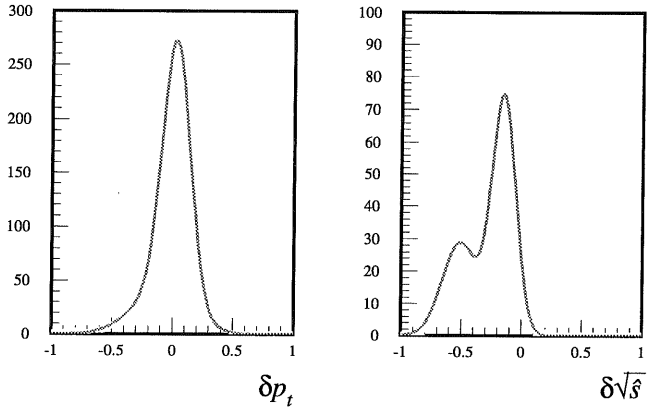

Figure 5.6: The δp_t and $\delta\sqrt{\hat{s}}$ distributions for the JADE algorithm with setting number II (see table 5.1), comparing jets at the hadron level with the matrix element partons, for the cut scenario used in fig. 5.5. The means of the distributions are the systematic shifts $< \delta p_t >$ and $< \delta\sqrt{\hat{s}} >$.

the spread. This will be noted in the text. If we apply the jet algorithm on the matrix element partons, without parton showers, we get a nearly perfect description by all algorithms. When including the full QCD cascade there is a certain probability that a parton from the initial state parton shower will be merged with matrix element partons, resulting in different directions and p_t's of the jets. In fig. 5.7 the mean of the absolute deviation $< \Delta(\eta\phi) >$ between the matrix element partons and the partonic final state jets is plotted as a function of the algorithm setting, with higher setting numbers corresponding to an increasing hardness of the jets. In (η, ϕ) space, the deviation amounts to $\gtrsim$ 0.2-0.3 units which is less than half of the cone radius (see section 5.1.1). We also see that the two k_t algorithms and the CONE reconstruct the jet direction best, while the JADE and LUCLUS algorithms generally have a worse resolution, corresponding to the higher values of $< \Delta(\eta\phi) >$ in fig. 5.7, even though there is no significant systematic shift in the direction of the jets. For $(p_t, \sqrt{\hat{s}})$ as seen in fig. 5.8, LUCLUS and JADE again gives the worst representation of the hard partons, deviating around 20%. The Inclusive k_t provides the best description, similar to that of the CONE and k_t algorithms, with a mean absolute deviation around 10-15% for the various settings. The problem of JADE and LUCLUS lies in the reconstructing of too large values

of $\hat{s}$ and p_t in the partonic final state. The low resolution in p_t is mostly due to a bad reconstruction of the forward jet, but the increased hardness of the cut for these algorithms (higher settings) increases the resolution of the invariant mass $\sqrt{\hat{s}}$ of the jets.

For high Q^2 the results can be seen in fig. 5.9 and 5.10. The algorithms generally perform better in the high Q^2 region, the JADE algorithm now providing a reconstruction comparable to that of the other algorithms. This might be due to the fact that at high Q^2 the jets are less forward than at low Q^2, and JADE has large problems with the forward jets at low Q^2. If the discrepancy between the matrix element partons and the jets in the partonic final state increases with the number of partons emitted, the better resolution at high Q^2 might partly be explained by the smaller phase space available for initial state radiation because of the larger x_{Bj}[5]. In short, when it comes to reconstructing the properties of the partons from perturbative QCD in the partonic final state, the Inclusive k_t algorithm is performing best in the low Q^2 regime. The performance of JADE and LUCLUS is poor. In the high Q^2 phase space all algorithms are similar in performance, the reconstructed jets giving a better description of the matrix element properties than at low Q^2. The effects are caused by the initial state radiation, and the difference in low/high Q^2 could be understood in terms of the different phase-space available for initial state QCD radiation. The fact that the resolution of all algorithms does not improve for the harder jets at the higher settings, is caused by soft matrix element partons being reconstructed as hard jets.

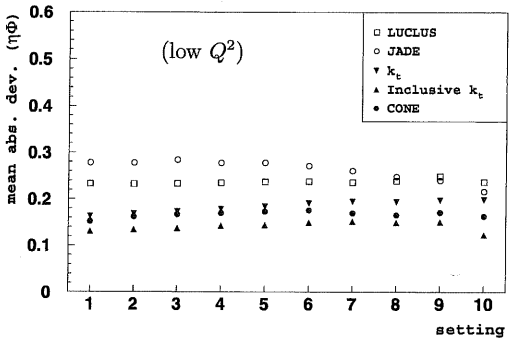

Figure 5.7: The mean absolute deviation between the matrix element partons and the corresponding jets at the parton shower level in (η, ϕ) space at low Q^2 as a function of the setting used in the algorithm seen in table 5.1.

[5] $x_{Bj} = Q^2/sy$

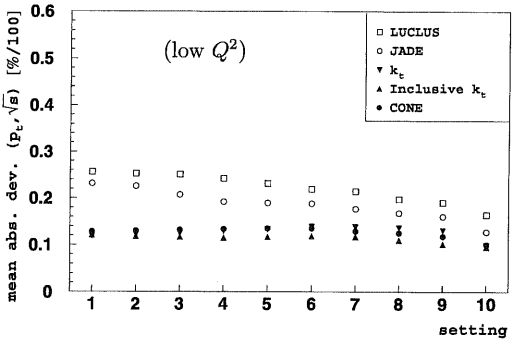

Figure 5.8: The mean absolute deviation between the matrix element partons and the corresponding jets at the parton shower level for $(p_t, \sqrt{\hat{s}})$ at low Q^2 as a function of the setting used in the algorithm seen in table 5.1.

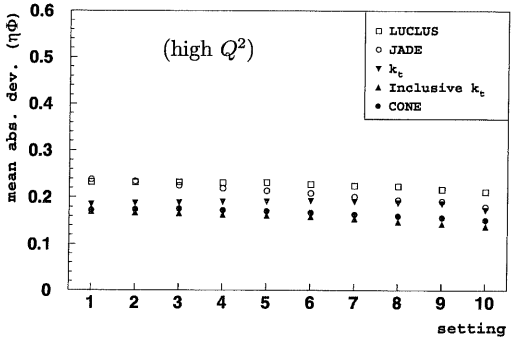

Figure 5.9: The mean absolute deviation between the matrix element partons and the corresponding jets at the parton shower level in (η, ϕ) space for the high Q^2 sample as a function of the setting used in the algorithm seen in table 5.1.

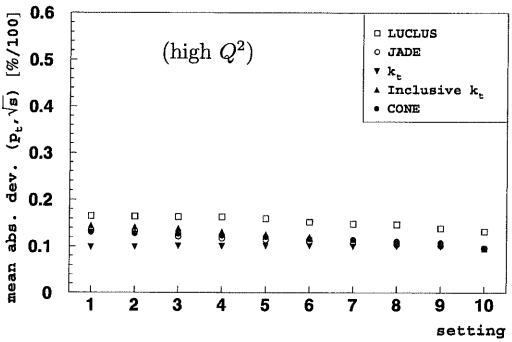

Figure 5.10: The mean absolute deviation between the matrix element partons and the corresponding jets at the parton shower level for $(p_t, \sqrt{\hat{s}})$ for the high Q^2 sample as a function of the setting used in the algorithm seen in table 5.1.

5.5.2 From Matrix Elements to Hadrons

Figs. 5.11-5.12 give a comparison of jets in the partonic and hadronic final states (where there is no demand for two hard partons). We observe a deviation for $(p_t, \sqrt{\hat{s}})$, as defined in eq. (5.10) around 15% for the lower settings, decreasing down to $5\% - 10\%$ using tighter cuts for all algorithms. At higher Q^2 these deviations are generally smaller. To see the effect of hadronization on the jets reconstructed in the partonic final state we let the partons fragment into hadrons in the MC program and require two jets being reconstructed on the hadron level. The combined influence of parton showers and fragmentation can be seen in figs. 5.13-5.14 for the low Q^2 region, and the corresponding plots for the high Q^2 sample are given in figs. 5.15-5.16. The figures show a comparison of the jet quantities for the matrix element partons and the jets in the hadronic final state. Generally there is no systematic change in the reconstruction of the ϕ angle due to hadronization, why the spread is the dominant factor in the mean absolute deviation of equation (5.9). At low Q^2 the algorithms deviate between 0.15-0.3 units, in (η, ϕ) space for all settings, with JADE having the worst resolution.

As seen in figs. 5.14 and 5.16, the situation for $(p_t, \sqrt{\hat{s}})$ is different. The hadronization effects for JADE and LUCLUS are very large, now deviating around 40-50% for low Q^2. Due to fragmentation a systematic shift in the reconstruction of p_t, and especially $\sqrt{\hat{s}}$, is introduced (similar to the shift for $\sqrt{\hat{s}}$ seen in fig. 5.6).

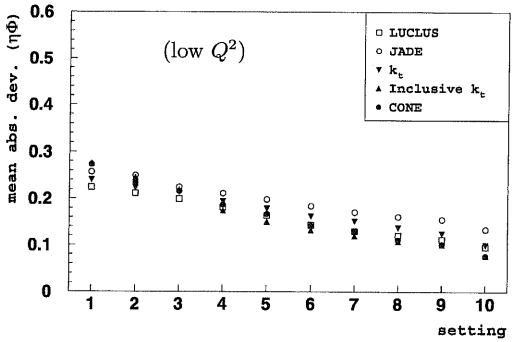

Figure 5.11: The hadronization correction comparing jets at parton and hadron level in (η, ϕ) at low Q^2 space as a function of the setting used in the algorithm seen in table 5.1.

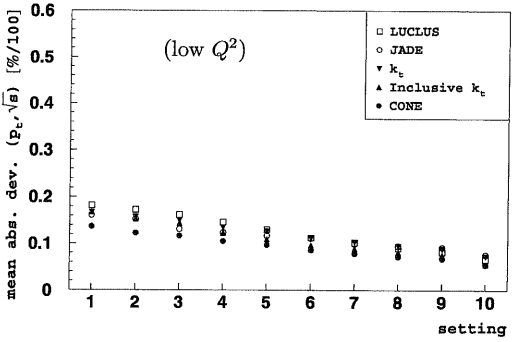

Figure 5.12: The hadronization correction comparing jets at parton and hadron level for $(p_t, \sqrt{\hat{s}})$ at low Q^2 as a function of the setting used in the algorithm seen in table 5.1.

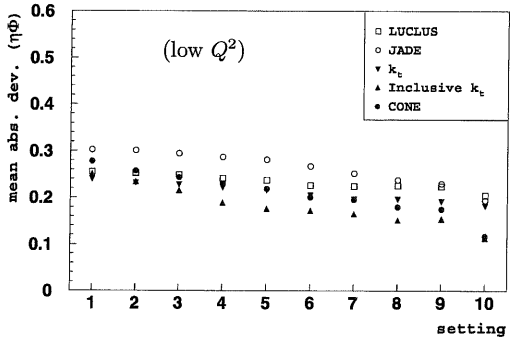

Figure 5.13: The mean absolute deviation between the matrix element partons and the corresponding jets at the hadron level in (η, ϕ) space at low Q^2 as a function of the setting used in the algorithm seen in table 5.1.

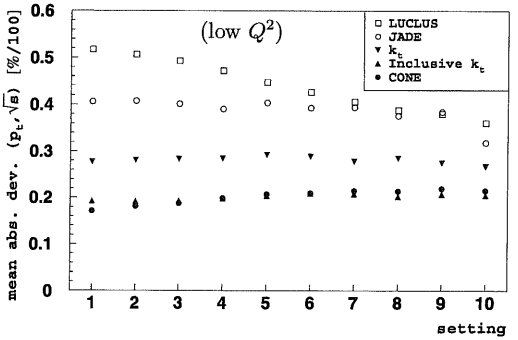

Figure 5.14: The mean absolute deviation between the matrix element partons and the corresponding jets at the hadron level for $(p_t, \sqrt{\hat{s}})$ at low Q^2 as a function of the setting used in the algorithm seen in table 5.1.

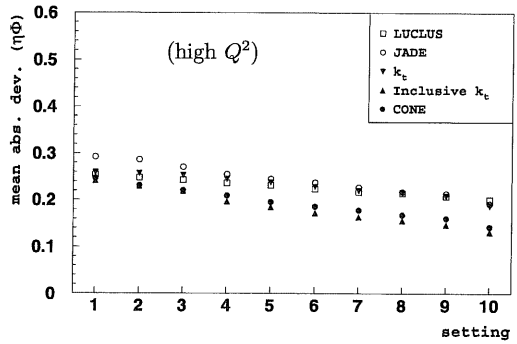

Figure 5.15: The mean absolute deviation between the matrix element partons and the corresponding jets at the hadron level in (η, ϕ) space for the high Q^2 sample, as a function of the setting used in the algorithm seen in table 5.1.

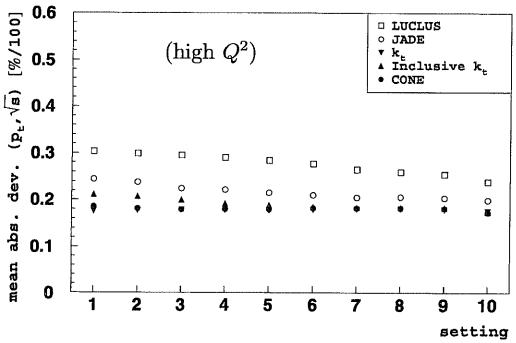

Figure 5.16: The mean absolute deviation between the matrix element partons and the corresponding jets at the hadron level for $(p_t, \sqrt{\hat{s}})$ for the high Q^2 sample, as a function of the setting used in the algorithm seen in table 5.1.

For LUCLUS and JADE the large shift might be caused by the inclusion of energetic particles (possibly with low p_t) close to the beam-remnant into the jet, with a large difference in angle compared to the rest of the jet particles. This effect is avoided in the Inclusive k_t, here deviating around 20%, where the parameter R in eq. (5.7) ensures a reasonably small space distance between the clustered particles. At higher Q^2 the effect of hadronization is smaller, but still relatively large. The (η, ϕ) resolution is similar for all algorithms, while the $(p_t, \sqrt{\hat{s}})$ resolution is still worse for JADE, and much worse for LUCLUS. The CONE algorithm is similar to the Inclusive k_t in performance. For the CONE and Inclusive k_t the deviation even increases slightly when demanding more p_t in the jets for the higher settings at low Q^2. In the reconstruction of rapidity, a systematic shift is introduced for the Inclusive k_t, and especially for the CONE algorithm at lower settings as illustrated in fig. 5.17. The fact that the reconstructed jets are shifted to the forward direction indicates that this might be connected to the string-fragmentation[6]. If this is the case, the effect in the different string configurations in BGF and QCD-compton events seen in fig. 2.11 should differ. Studying the effect for BGF and QCD compton events individually we see that it is larger for the BGF events. Since the high Q^2 region is dominated by QCD compton events the effect is smaller in this region of phase space.

In short, pure hadronization corrections decrease with increasing settings for all algorithms. The effect of hadronization on the jets reconstructed as two jets in the partonic final state generally decrease the algorithm resolution. The effect is most evident when it comes to the reconstruction of $\hat{s}$ and p_t for the clustering type algorithms. As discussed above this is due to the reconstruction of too hard jets, and the inclusion of particles close to the beam-pipe in events with soft matrix element partons. This reflects the effect of the parton shower partons and fragmentation. At high Q^2 the increased resolution can be explained by the decreasing phase space of initial state radiation and a higher separation of the jets and the proton remnant.

5.5.3 Performance sensitivity to the algorithm setting

If the setting used for a certain algorithm lies in a region where the reconstruction quality changes rapidly, there is a risk of imposing an error due to the finite resolution of the detector. If, for example, the p_t cut used in the CONE algorithm lies in a region where the systematic shift, $< \delta p_t >$, changes drastically, this will introduce an additional systematic error from the jet reconstruction. We therefore studied the variation of the systematic shift in the reconstruction of p_t as as the parameter setting changes. If this change is comparable in size to the resolution of the algorithm, comparing the matrix element partons with the hadron level jets, a systematic error is introduced. Typical values for the resolution of the backward and forward

[6]This will have to be studied in more detail using independent fragmentation.

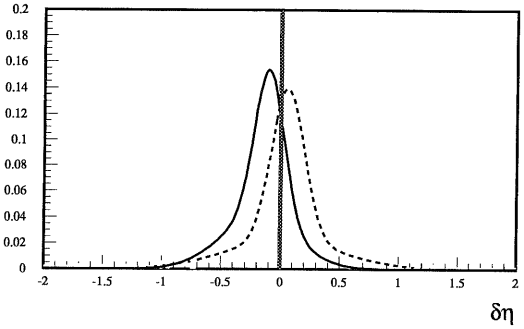

Figure 5.17: The systematic shift in η for the CONE (using setting II in table 5.1) forward jets at hadron level is seen in the $\delta\eta$ distribution. The full line shows $\delta\eta$ for the BGF sub-sample, which at low Q^2 is the dominant part. The hatched line shows $\delta\eta$ for the QCD-compton sub-sample. The histograms are normalized to unity. The distributions at high Q^2 are similar, but the relative fraction of QCD-compton events is higher.

jet of any algorithm are 20-30%. The changes in the systematic shift of the jet p_t reconstruction are in the order of a few percents and hence well below the resolution for all algorithms and all settings, as well as below any detector resolution. We also checked that the above statement is true for the reconstruction of $\sqrt{\hat{s}}$.

5.5.4 Next To Leading Order sensitivity

For the CONE, JADE and the Inclusive k_t algorithms, representing the three main types of algorithms, we studied the sensitivity to the in principle unknown renormalization and factorization scales in Next to Leading Order calculations of the jet rate for the low Q^2 region. The default scales of $Q^2 + 50$ GeV^2 were varied by a factor of four. The results are presented as a function of Q^2. The Next to Leading Order calculations are only reliable in the phase space of asymmetric p_t's of the jets [43], why we demand a minimum value of the sum of the jet p_t. We used two different settings for the algorithms, giving different jet rates. This will reveal the major differences in the behaviour of the algorithm at settings producing either high or low jet rates. The results are presented in fig. 5.18 and it can be seen that the JADE algorithm suffer from a large scale sensitivity.

The CONE and Inclusive k_t algorithms behave quite similarly with a change in the 2-jet rate of the order of 20%, varying the scales by a factor of four from the nominal value. Hence, the JADE algorithm should not be used in NLO calculations, since its predictive power is lower, compared to the CONE and Inclusive k_t, due to a large scale sensitivity.

The cross section sensitivity to the factorization and renormalization scales have been studied in more detail [44, 32] elsewhere.

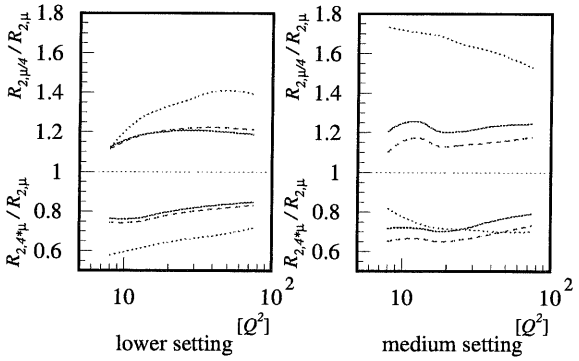

Figure 5.18: Changing the factorization an renormalization scales for three types of jet algorithms (JADE: dotted, CONE: full line, Inclusive k_t: hatched line.) Here we plot the relative change in the 2-jet rate, changing the renormalization and factorization scales. The left plot shows the the response to a change of the scales by a factor 4 (lower plots) and by a factor 1/4 (upper plots) for the scenario of lower settings, where the CONE and Inclusive k_t algorithm have a jet cut off of 3 GeV in p_t. The JADE used a $y_c = 0.02$. The sum of the jet p_t's had to be larger than 8 GeV. The right hand plots show the corresponding quantities using medium settings of the algorithms, a jet cut of of 5 GeV for CONE and Inclusive k_t and a $y_c = 0.04$ for JADE. The sum of the jet p_t's had to be larger than 13 GeV. The nominal scale, μ, is in both cases $Q^2 + p_t^2$.

5.6 Conclusions

The ability to reconstruct the properties of the hard partons from the matrix element process, using different jet reconstruction algorithms has been investigated. The effect of parton showers on the reconstructed jets is largest for the clustering algorithms JADE and LUCLUS. The pure effect of hadronization is similar, and reasonable in size for all algorithms. However, this does not reveal if the same errors in the jet reconstruction are made by the algorithms on both levels. Therefore we studied the accumulative effect of the QCD radiation and hadronization which revealed relatively large errors for the pure clustering algorithms JADE and LUCLUS at lower Q^2. At high Q^2 the resolution of the algorithms generally improves compared to lower Q^2, and the JADE algorithm now show a performance similar to that of the two variants the of k_t and the CONE algorithms. The overall best description of the matrix element properties, at both high and low Q^2, we get from the CONE and the Inclusive k_t algorithms.

The resolution sensitivity to the parameter setting used in the algorithms has been investigated and the results show that this will not lead to additional systematic errors in case of a low detector resolution. In next to leading order calculations of the 2-jet rate, the JADE algorithm shows a large sensitivity to the, in principle unknown, factorization and renormalization scales of QCD.

Part II

Parton Dynamics in Deep Inelastic Scattering

Chapter 6

Parton Dynamics In DIS

As was discussed in the first part of this thesis, the higher order QCD processes are important for the understanding of the full features of Deep Inelastic Scattering events. The question is what kind of parton dynamics is responsible for the gluon radiation? We saw that to describe the jet-rate of hard processes we needed to break the k_t ordering in the evolution to gain phase space for the matrix element sub-process. This can be accomplished in the DGLAP scheme if we are allowed to resolve the photon, or in terms of the, non-ordered (BFKL-like) emissions in the Color Dipole Model. To study the actual nature of these emissions several observables can be studied.

The (expected) type of parton dynamics for higher order QCD radiation differs in different regions of phase space as discussed in section 2.2.3. Since we expect the effects of the new BFKL-type of dynamics to set in at low-x_{Bj}, in the region $x_{Bj} < 0.0005$ (limited by kinematic constraints of the HERA machine and the acceptance of the H1 detector) properties like the k_t ordering of the propagator parton and ϕ-correlations in the initial state radiation that are expected to differ for different kinds of dynamics will be studied and compared to the region of $x_{Bj} > 0.0005$. We also studied a subset of events containing a highly energetic jet in the forward direction. This selection was designed to enhance the BFKL type of parton dynamics, at the same time suppressing the DGLAP type of evolution. Also here the sample was divided into two regions of x_{Bj}, larger or smaller then 0.0015 respectively, each containing approximately the same cross-section.

In the following section the kinematics of the initial state cascade will be discussed with emphasis on the reconstruction of the propagator parton (predominantly a gluon at low-x), followed by an introduction to the observables studied, and the results.

6.1 Kinematics of the Initial Cascade

The basis of this analysis is the reconstruction of the emitted gluons in the initial state QCD-cascade as jets, using the Inclusive k_t algorithm (see section

5.1.5). Using the notations in fig. 2.6 the transverse momentum of the propagator gluon k_t in the hadronic center of mass frame[1] can be written as:

$$\bar{k}_{tj} = \sum_{i \leq j} p_{t_i} \tag{6.1}$$

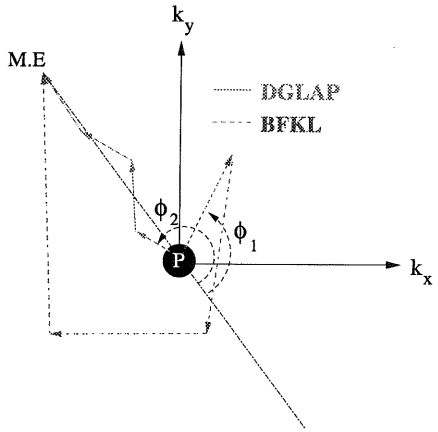

Figure 6.1: The path of the propagator gluon transverse momentum depends on the properties of the emitted gluons which differs from different types of parton dynamics. The arrows denote the emitted partons, and their (negative) sum equals the $\bar{k}_t$ according to eq. (6.1).

The $\bar{k}_t$ of the propagator gluon is hence solely determined from the emitted gluons in the cascade. In the laboratory frame the $\bar{k}_t$ of the photon also has to be taken into account. In the plane of transverse momentum, the "k_t-plane", the "path" of the propagator gluon can be described as in fig. 6.1, where the arrows denote the emitted gluon transverse momentum, p_{ti}. The Parton Evolution equations that govern the k_t of the propagator gluon will lead to different paths of the propagator parton. To illustrate this we recollect the implications of the different parton evolution equations on the propagator gluon from section 2.2.3.

- **DGLAP:** The k_t, denoting the length of the transverse momentum vector $\bar{k}_t$, is strongly ordered $k_{tn} \ll .. \ll k_{t2} \ll k_{t1}$. As seen in fig. 6.1 this demand implies that the emitted gluons will tend to be emitted in a narrow region of ϕ. The transverse momentum of the quark-box is compensated by the entire chain of emitted gluons. The correlations between partons in the DGLAP scenario can thus be said to be long-range.

- **BFKL:** The non-ordered k_t leads to a "random-walk" by the propagator gluon. This implies that the emitted gluons are less aligned since

[1] Or any frame differing from the hadronic center of mass frame only by a longitudinal boost.

after each emission the k_t need not to be increased. Sometimes this is expressed as the propagator gluon "forgetting" its history of emissions. We also recollect that the CDM based Monte Carlo generator ARIADNE generates gluon emissions corresponding to a non-ordered propagator parton.

6.2 Observables

To distinguish between the different types of parton dynamics, several observables can be studied. A common property is that they are not necessarily measurements of cross-sections, the traditional observable measured in DIS. Instead they involve correlations between partons (jets) revealing more exclusive properties about the underlying partons and the evolution equations governing them.

We focused on two main properties of the set of emitted partons which differ between the DGLAP and BFKL type of evolution.

6.2.1 k_t ordering

The observable $< \Delta k_t >$ measures the mean decrease in k_t per event as a function of the distance (in rapidity) measured from the quark-box towards the proton direction (see figure 2.6):

$$< \Delta k_t > = < k_{t_i} - k_{t_{i+1}} > \tag{6.2}$$

Negative values point towards the DGLAP type of evolution, i.e. the (average) k_t increases towards the photon side, while values around zero point towards the BFKL type of dynamics with random emissions in the k_t-plane.

6.2.2 ϕ-correlations

The second selected variable measures the angular, ϕ, correlations between the $\overline{k}_t$ of the gluon entering the hard sub-process (k_{t1} in fig. 2.6, corresponding to the sum of the quark-box p_t) and the p_t of the emitted gluons:

$$< \cos\phi > = \left\langle \frac{k_{t1} \cdot p_{ti}}{|k_{t1}||p_{ti}|} \right\rangle \tag{6.3}$$

In the DGLAP type of parton dynamics we expect this observable to be clearly negative also for emissions far from the quark-box due to the alignment of the emitted partons (see fig. 6.1) corresponding to long range correlations. In the BFKL type of parton dynamics most of the accumulated k_t from the quarks will be compensated by nearby emissions, leading to values of $< \cos\phi > \lesssim 0$ at large distances.

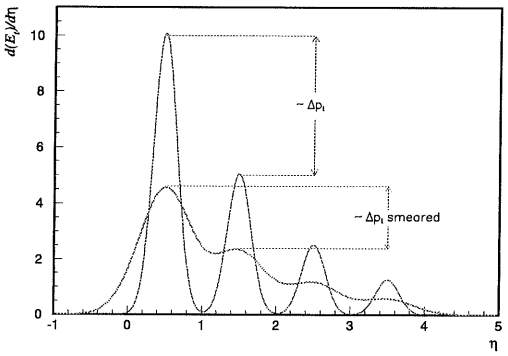

Figure 6.2: Illustration of the smearing of the particle (energy) flow caused by the detector as a function of rapidity. The upper curve shows the unsmeared particle flow, while the lower curve shows the flow after detector smearing. Note that the difference in p_t decreases as will any ordering in k_t, eq. (6.1)

6.2.3 Method

As stated above, the basis of this analysis is the reconstruction of the four-momentum of the emitted gluons and quarks seen in fig. 2.6. This is equivalent to the reconstruction of the k_t of the propagator gluon as understood from eq. (6.1). Using the Inclusive k_t algorithm without any p_t-cut, all particles will be included in the jets. The algorithm is suitable for the reconstruction of soft jets from the initial state QCD radiation.

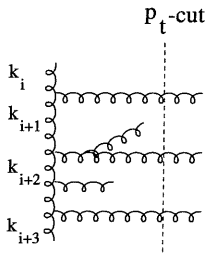

Figure 6.3: The number of segments of the propagator parton (compare with fig. 2.6) is not defined by the total set of jets found, but by the sub-set passing a certain p_t-cut.

It is clear that the effects of hadronisation and the limited resolution of the detector will smear the energy carried by the emitted partons. This will in general lead to a decrease in the signal measured in this analysis. If the propagator gluon is k_t ordered, due to the limited resolution, the smearing from the detector will tend to decrease the signal as illustrated in fig. 6.2. In a similar fashion, ϕ-correlations between emitted partons tend to decrease. The limited acceptance of the detector also tends to decrease the measured sig-

nal, as does detector induced noise. It can be shown that the major part of the decrease in signal due to the detector comes from the limited energy resolution (see section 6.6). According to the definition of k_t, as seen in eq. (6.1), the number of emissions defines the number of sections of the propagator gluon. Due to hadronisation and detector effects this number could in principle be very large, as the jet-algorithm tend to reconstruct on average a larger number of jets on detector level compared to the number of jets on hadron level, or to the number of partons. To restore the infrared safety, a "post-clustering" method is used by applying a p_t-cut of 1.5 GeV, as illustrated in fig. 6.3. It should be stressed that even though the segments of the propagator gluon are defined by the jets passing the p_t-cut, all the four-momentum in the event (including the information from the jets with $p_t < p_t$-cut) is used when calculating the k_t.

6.3 Data Selection

The DIS phase space considered in this analysis is defined by:

$5\ \text{GeV}^2 < Q^2 < 75\ \text{GeV}^2$

$y > 0.1$

$\text{E}_{el} > 10\ \text{GeV}$

$156^o < \theta_{el} < 175^o$

The data used were selected from the $\sim$15 pb^{-1} collected in the 1997 data running period. Only runs taken during stable running conditions were used. The trigger used was s0. During 1997 s0 triggered on events with a cluster in the SPACAL backward calorimeter with $\text{E}_{el} > 6$ GeV, and the arrival time of the electron inside the proper time window. Certain regions in the SPACAL suffered from inefficiencies of s0 [45]. These regions were either removed from the analysis, or the event sample was rescaled to account for this effect (see Appendix C). The basics of the H1 triggering system is explained in section 3.2.4. In 1997 the large data volume taken required down-scaling of soft physics such as low-Q^2 events due to their large cross-section. Thus only a fraction of these events were saved, with a PRESCALE corresponding to the down-scaling factor at the different trigger levels. These factors were then applied as weights ≥ 1 for the event. At the lowest trigger level (L1), large parts of the low-Q^2 events were not saved. The down-scale factor has been defined at the time of data taking, based on the current running conditions. A similar procedure was performed at trigger-level four (L4), where the down-scaling factor was increased with decreasing Q^2. At the last level (L5) the events were classified according to predefined physics classes. These classes were used to make a preselection of data, where the classes corresponding to SPACAL-electron (low/medium-Q^2) and jet events were selected. Also on L5, low-scale physics was down-scaled.

6.3.1 Background Suppression

The suppression of background (apart from the selection/rejection on the different trigger levels) was done in a similar way as for the analysis of 1994 data presented in Part I.

Control Quantities

In figures 6.4 the basic quantities for the electron and the kinematic variables are shown for 1997 data compared to the simulated Monte-Carlo from RAPGAP without the resolved photon option, and ARIADNE. A close to perfect agreement is observed.

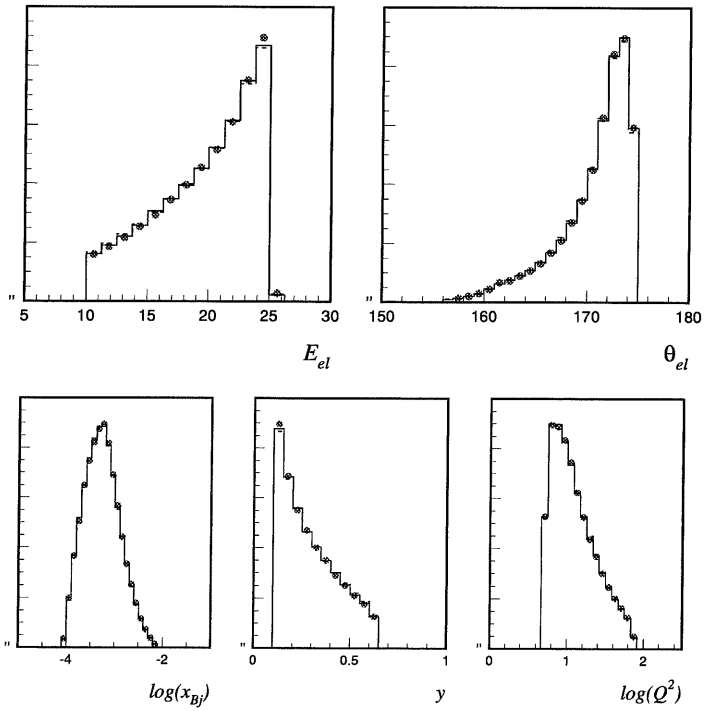

Figure 6.4: The energy and polar angle of the electron (top) and the kinematic variables x_{Bj}, y and Q^2 for the 1997 data sample (points) compared to the Monte-Carlo results from ARIADNE (dashed) and RAPGAP (solid). All plots are shape normalized.

6.4 Forward Jet Selection

The concept of Forward Jets in DIS, and how to detect and to measure their cross-section has been described in detail in [46], and published in [47]. The cuts defining a forward jet are the following:

$$p_t > 3.5 \text{ GeV}$$

$$7^o < \theta_{jet} < 20^o$$

$$x_{jet} = E_{jet}/E_p > 0.035$$

$$0.5 < p_t^2/Q^2 < 2$$

The main idea behind selecting events with a highly energetic jet in the forward region is to enhance the BFKL type of parton dynamics in the initial QCD cascade, and at the same time suppress the DGLAP type of parton evolution. Recollecting the evolution properties for the two characteristic kinds of evolution equations; DGLAP: $k_{t1}^2 \gg k_{t2}^2 \gg .. \gg k_{tn}^2$, BFKL: $x_1 \ll x_2 \ll .. \ll x_n$, where the notations are explained in fig. 2.6, it is easily understood that the presence of a forward jet leads both to a large value of the propagator virtuality, k_n^2, in the forward region, narrowing the k^2 range for further emissions, as well as ensuring a large value of x_n, enhancing the range in x for the BFKL type of dynamics, particularly so at low values of x_{Bj}.

The cut in x_{jet} ensures the large range for evolution in x, while the p_t^2/Q^2 cut suppresses the range for DGLAP evolution. The high p_t for the forward jet naturally decreases the forward jet cross-section. To decrease the statistical errors one would therefore like to keep this p_t cut as low as possible. The cost of a low p_t cut is a less well defined jet-structure as the relative importance of the detector induced background becomes larger, and as the separation from the remnant becomes more difficult. In [47] the CONE algorithm was used for the jet finding, compared to the Inclusive k_t algorithm used in this analysis. The two algorithms are similar in performance and results, why for consistency the Inclusive k_t was used for all jet-finding in this analysis, including the forward-jet selection.

6.5 Detector Level Results

In the following subsections the results on detector level will be presented for the inclusive DIS sample, as well as for the sub-sample containing a forward jet event collected with H1 in 1997. All errors are purely statistical. The results for data are compared to a sample of detector simulated RAPGAP (DGLAP) files generated without the contributions from resolved photons, as well as to a detector simulated sample generated using the ARIADNE (CDM) program.

6.5.1 Propagator gluon k_t ordering

Shown in figure 6.5 are the $< \Delta k_t >$ results as a function of the rapidity distance from the matrix element, $\Delta\eta$, for the inclusive DIS sample, as well as for the sub-sample containing a forward-jet at low and medium x_{Bj}. Negative values mean a decrease in k_t, when moving from the photon side towards the proton side of the reaction. One sees that the DGLAP evolution in RAPGAP describes the size and shape of the $< \Delta k_t >$ as a function of $\Delta\eta$ better than the CDM based parton emissions in ARIADNE in case of inclusive DIS, where the data even suggests a larger k_t ordering than the prediction from RAPGAP. Selecting events containing a forward jet, the data instead tend to lie between the predictions from the two Monte Carlo programs, moving towards the CDM prediction. The comparison of the absolute size of $< \Delta k_t >$ between different event samples is not trivial since $< \Delta k_t >$ depends on the energy scale in the event which differs in different parts of phase space.

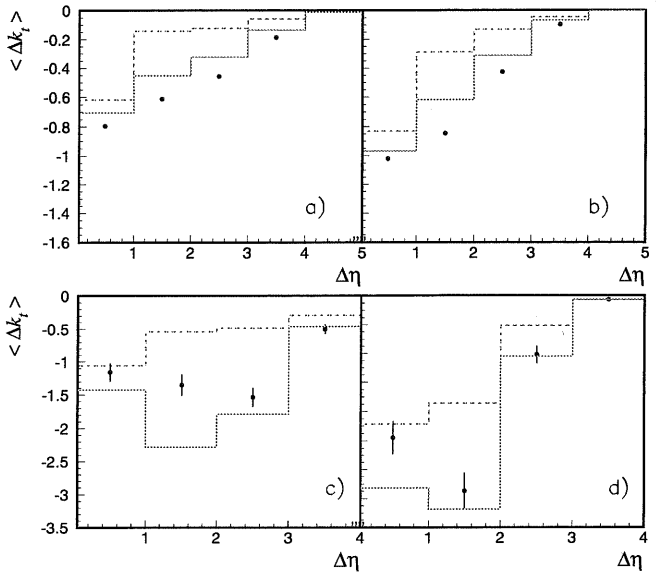

Figure 6.5: The mean decrease in k_t at low a), c) and medium b), d) x_{Bj} in bins of $\Delta\eta$ as measured from the quark-box seen in figure 2.6 for the inclusive DIS sample on detector level (top), and for the sub-sample containing a forward-jet (bottom). The dotted curve shows the prediction from the CDM based ARIADNE Monte Carlo, while the solid curve shows the same quantity for the DGLAP based RAPGAP program. The points are the values for 1997 H1 data with statistical errors.

6.5.2 ϕ-correlations

In figure 6.6 $< \cos\phi >$ as a function of $\Delta\eta$ on detector level is shown for the inclusive sample, as well as for the sub-sample containing a forward-jet. It is quite clear that, for the inclusive DIS sample, the DGLAP based QCD emissions from the RAPGAP Monte Carlo better describes the correlation between the partons across the range in η compared to ARIADNE. The larger negative values at higher values of $\Delta\eta$ for data and RAPGAP show that the correlations are of longer range, in agreement with the expectation from a DGLAP type of parton dynamics. The significantly larger negative values of $< \cos\phi >$ for the large-x sample points towards a more DGLAP like cascade compared to lox-x. When selecting the events containing a forward jet, the data lies in between the predictions from the two Monte Carlo programs. At low-x the effect is clearly significant, and the data points are well described by the prediction from CDM.

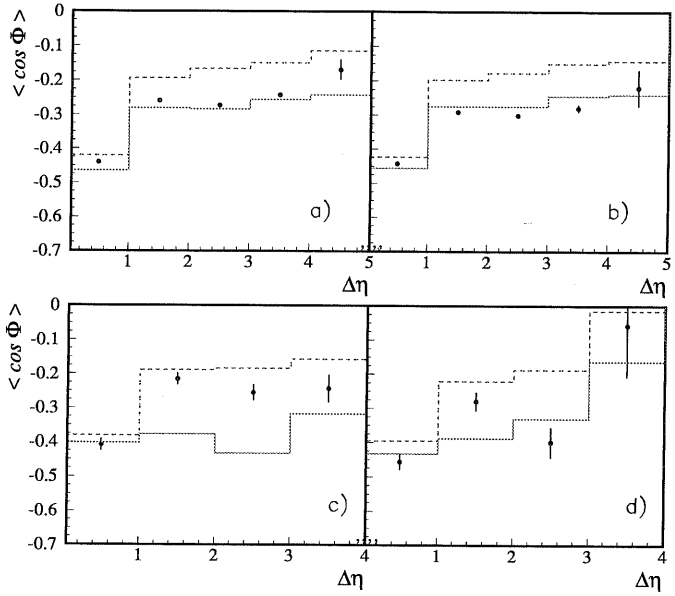

Figure 6.6: $< \cos\phi >$ as a function of $\Delta\eta$ with ϕ being the angle (see figure 6.1) between the k_t of the gluon coupling to the matrix element and the emitted gluons measured as jets at detector level for inclusive DIS a), b), and the sub-sample containing a forward-jet c), d). In a), c) for low-x_{Bj}, and for medium x_{Bj} in b), d). Full curve: RAPGAP, dashed curve: CDM, points: H1 1997 data with statistical errors.

6.6 Correction to Hadron Level

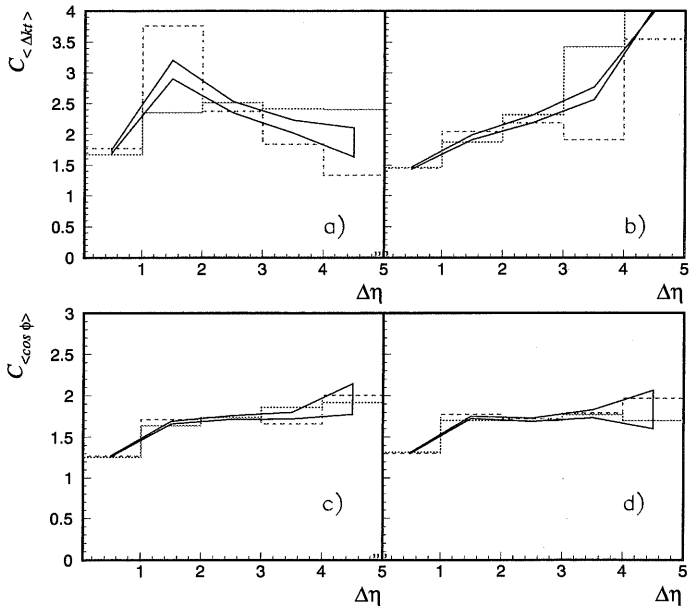

Figure 6.7: Correction factors, C, see eq. (6.4), for $< \Delta k_t >$ a), b) and $< \cos\phi >$ c), d) from ARIADNE (dashed line) and RAPGAP (full line). In a), c) for low-x_{Bj} and in b), d) for larger x_{Bj}. The applied correction is the mean value from the two Monte-Carlos, here shown as the mid-points in the statistical error-band.

Motivated by the differences at detector level, one would like to compare the data corrected to hadron level, with the different Monte Carlo model predictions. The procedure to correct for the effects of the detector and the QED radiation is similar to the one used for the jet-rate analysis in Part I. However, in this analysis, it should be stressed that the main observables are not simple cross-sections, why the concept of a bin-by-bin correction is not as straight-forward as was the case of the jet rate analysis. The correction factor used is as follows:[2]

$$C_X = \frac{< X >_{MC-had,nrad}}{< X >_{MC-det,rad}}, \tag{6.4}$$

[2]Here the notations: "had, det, rad, nrad" stands for hadron level, detector level, generated with QED radiation, and generated with no QED radiation.

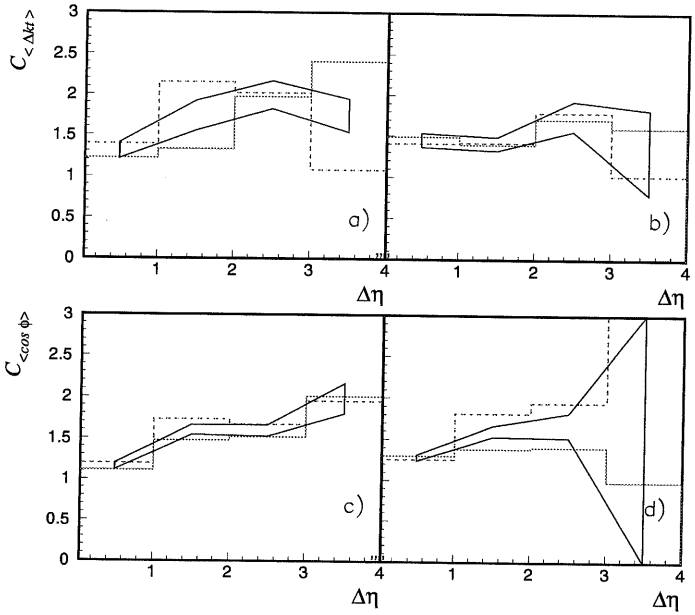

Figure 6.8: Correction factors, C see eq. (6.4), selecting the forward-jet subsample for $< \Delta k_t >$ a), b) and $< \cos\phi >$ c), d) from ARIADNE (dashed line) and RAPGAP (full line). In a), c) for low-x_{Bj} and in b), d) for larger x_{Bj}. The applied correction is the mean value from the two Monte-Carlos, here shown as the mid-points in the statistical error-band.

with X being either Δk_t or $\cos\phi$. C_X is multiplied with the raw data $< X >_{Raw.Data}$ to get the result corrected to hadron level:
$< X >_{Corr.Data} = C_X \cdot < X >_{Raw.data}$. The purity and efficiency for the reconstruction of jets with $p_t > 1.5$ GeV, as seen in figure 6.9, shows that there is a clear correlation between the jets at hadron and detector level, indicating that a bin-by-bin correction is reasonable. This is supported by the relatively small model dependence of the corrections as seen in figures 6.7,6.8. In section 6.6.1 we discuss how the main part of the relatively large correction of $< \Delta k_t >$ from hadron to detector level can be understood in terms of smearing induced by the limited resolution of the detector.

6.6.1 The large Correction - Detector Smearing

The size of the bin-by-bin corrections for the observables are in some cases comparable to the observable values. The detector smearing, as illustrated

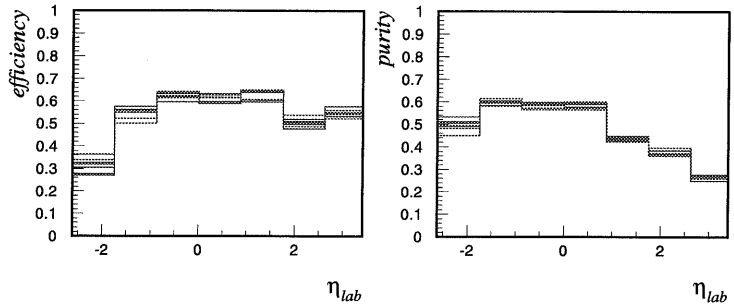

Figure 6.9: Efficiency and purity for of the reconstruction of jets with $p_t > 1.5$ GeV for ARIADNE. The different histograms shows the values for different slices of ϕ.

in fig. 6.2, is the main contributor to the large difference between the results at hadron and detector level. This can be shown at hadron level by smearing the four-momentum of the individual particles in the hadronic final state according to the resolution of the central and forward part of the detector. The results closely resembles those found on detector level, where also the acceptance effects and the full information on dead material corrections have to be taken into account to regain the exact detector level results.

6.7 Systematic Errors

The main systematic errors in jet cross-section measurements usually come from the uncertainty in the calibration of the LAr calorimeter. The cluster energy measured is only known to within around $\pm 4\%$. Reproducing the results changing the calibration of the clusters by $\pm 4\%$ will thus give an estimate on the size of the systematic shift induced by this uncertainty. In our case the uncertainty from the LAr energy scale is relatively small and is of the same order of magnitude as the systematic error caused by the erroneous simulation of the full features of the H1 detector in 1997 (see section 6.7.2). The systematic errors from the model dependence of the correction procedure and the erroneous tracker simulation are added in quadrature to the statistical error.

6.7.1 LAr Energy Scale

The results of shifting the LAr energy scale by ±4% can be seen in table 6.1. Since the differences between the values in the different $\Delta\eta$ bins are statistically insignificant the values in table 6.1 were taken from fits to the actual distributions. The relatively small values are explained by the construction of the observables not being simple cross-section measurements.

Systematic Errors from LAr energy scale ±4%

low/high-x_{Bj} $< \Delta k_t >$	low/high-x_{Bj} $< \cos\phi >$
±2% / ±2%	±3% / ±4%

Table 6.1: The systematic errors due to the uncertainty in the LAr energy scale. The values were taken from fits to the actual distributions.

6.7.2 Phi Asymmetry of Tracker Efficiency

In 1997, the central tracker suffered from inefficiency in a specific region of ϕ. Normally this would be taken into account in the detector simulation why the effect would be accounted for in the correction procedure. Since this was not the case, we studied the effect of the inefficient particle identification on hadron level. The effect is similar to that of bad resolution, decreasing the measured values of the observables leading to a one sided systematic error as seen in table 6.2.

Systematic Errors from Tracker Inefficiency

low/high-x_{Bj} $< \Delta k_t >$	low/high-x_{Bj} $< \cos\phi >$
-4% / -4%	-2% / -2%

Table 6.2: The systematic shift induced by the inefficient region in the central tracker.

6.7.3 Model Dependence - Systematic Error

Ideally the detector correction is independent of the Monte-Carlo model used. The difference between the applied correction factor and the individual correction factors from the two Monte-Carlos, as seen in figures 6.7,6.8 are applied as an estimate of the model dependence in the correction procedure.

6.8 Corrected Results

In figure 6.10 the distributions in $< \Delta k_t >$ and $< \cos\phi >$ as functions of $\Delta\eta$ corrected to hadron level are shown for the inclusive DIS sample. It is quite clear that the DGLAP type of parton evolution best describes the data,

both for $< \Delta k_t >$ and $< \cos\phi >$. For $< \cos\phi >$ it is also worth noticing the difference between the results in the two bins of x_{Bj}: for the lower x_{Bj} bin the result tends to lie closer to the CDM prediction (compared to the values for higher x_{Bj}) as expected from a more BFKL like type of parton dynamics. In figure 6.11, the results, selecting the sub-sample containing a forward jet with $p_t > 3.5$ GeV, corrected to hadron level are shown. For statistical reasons the number of bins are reduced. For both $< \Delta k_t >$ and $< \cos\phi >$, compared to inclusive DIS, the data moved towards the predictions from the CDM emissions from ARIADNE. For $< \cos\phi >$ at low x_{Bj}, the data points are clearly better described by ARIADNE.

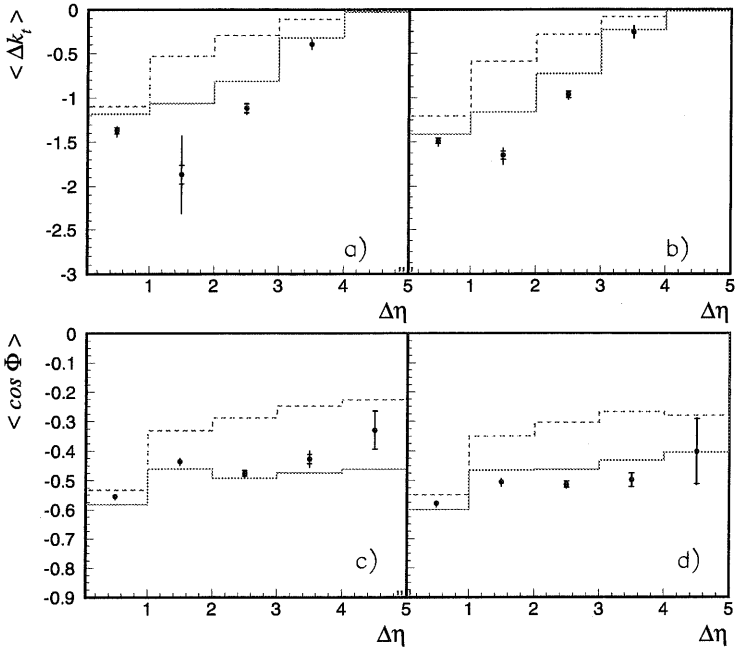

Figure 6.10: $< \Delta k_t >$ (top) and $< \cos\phi >$ (bottom) corrected to hadron level (points), compared to the hadron level predictions from ARIADNE (dashed line) and RAPGAP (full line). In a) for low-x_{Bj} inclusive DIS and for medium x_{Bj} inclusive DIS in b). The inner error bars show the statistical errors, and the full error is the quadratic sum of the statistical and systematic errors.

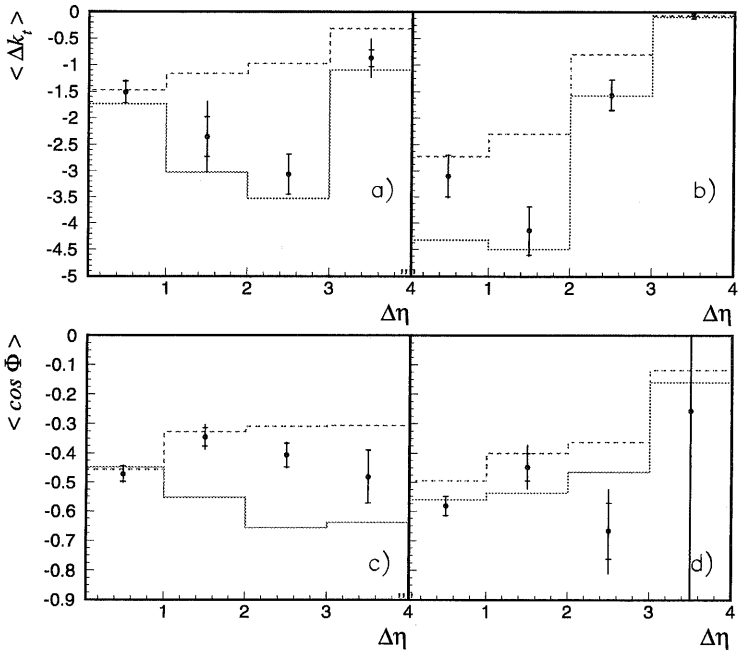

Figure 6.11: $< \Delta k_t >$ (top) and $< \cos\phi >$ (bottom) corrected to hadron level (points) selecting the sub-sample containing a forward jet compared to the hadron level predictions from ARIADNE (dashed line) and RAPGAP (full line). In a) for low-x_{Bj} and in b) for larger x_{Bj}

6.9 Conclusions and Outlook

In this analysis we have shown, for the first time, that a difference between the models for the parton dynamics can be seen comparing data in different regions of phase-space with Monte Carlo predictions built around the k_t ordered DGLAP evolution equations, and the non k_t ordered CDM for the higher order QCD radiation.

The differences seen between the inclusive sample and the sub-sample containing a forward-jet are in line with what we would expect from the onset of a BFKL type of parton dynamics. The inclusive DIS sample clearly favors the DGLAP type of parton dynamics. Selecting the sub-sample containing a forward jet, especially at low-x the results now tend to lie in between what is predicted from the CDM and DGLAP type of parton emissions.

The inclusion of new data in a future analysis would make a more detailed analysis possible, decreasing the errors which would be important especially when it comes to the forward-jet selection. A further extension of this analysis would be to measure the unintegrated gluon density, especially looking at diffractive scattering. It would also be interesting to study other observables of the same kind as studied here, e.g. the dispersion of k_t as presented in [48], as well as differential mini-jet cross sections.

Bibliography

[1] C. Jacobsson, phD Thesis , Jet Azimuthal Angle Asymmetries in Deep Inelastic Scattering as a test of QCD.

[2] F. Halzen, A. Martin, *Quarks and Leptons* (J. Wiley & Sons, Inc., 1984).

[3] V. Gribov, L. Lipatov, *Sov. J. Nucl. Phys.* **15** (1972) 438 and 675.

[4] L. Lipatov, *Sov. J. Nucl. Phys.* **20** (1975) 94.

[5] G. Altarelli, G. Parisi, *Nucl. Phys.* **B 126** (1977) 298.

[6] Y. Dokshitser, *Sov. Phys. JETP* **46** (1977) 641.

[7] H. Jung, L. Lonnblad, (2001).

[8] E. Kuraev, L. Lipatov, V. Fadin, *Sov. Phys. JETP* **44** (1976) 443.

[9] E. Kuraev, L. Lipatov, V. Fadin, *Sov. Phys. JETP* **45** (1977) 199.

[10] Y. Balitskii, L. Lipatov, *Sov. J. Nucl. Phys.* **28** (1978) 822.

[11] M. Ciafaloni, *Nucl. Phys.* **B 296** (1988) 49.

[12] S. Catani, F. Fiorani, G. Marchesini, *Phys. Lett.* **B 234** (1990) 339.

[13] S. Catani, F. Fiorani, G. Marchesini, *Nucl. Phys.* **B 336** (1990) 18.

[14] G. Marchesini, *Nucl. Phys.* **B 445** (1995) 49.

[15] H. Jung, G. P. Salam, (2000).

[16] L. Lönnblad, *Comp. Phys. Comm.* **71** (1992) 15.

[17] L. Lönnblad, The Color dipole cascade model and the Ariadne program, presented at MC91 Workshop on Detector and Event Simulation in High Energy Physics, Amsterdam, Netherlands, Apr 8-12, 1991.

[18] B. Andersson, The Lund Model, 1998, iSBN 0 521 42094 6.

[19] B. Andersson, G. Gustafson, C. Peterson, *Zeit. Phys.* **C1** (1979) 105.

[20] H. Collaboration, The H1 detector at HERA, 1997, nucl. Instr. and Meth. in Phys. Res. A 386.

[21] J. Ban et al., *Nucl. Instrum. Meth.* **A372** (1996) 399.

[22] J. Spiekermann, Die Messung der Rate von 2-Jet-Ereig-nissen in tiefinelastischer Streuung bei HERA, pHD theses.

[23] H1 Collaboration, T. Ahmed et al., Dijet Event Rates in Deep Inelastic Scattering at HERA, DESY 98-076 and hep-ex/9806029.

[24] F. Abe et al., *Phys. Rev.* **D45** (1992) 1448.

[25] S. Catani, M. H. Seymour, *Acta Phys. Polon.* **B28** (1997) 863.

[26] B. P. otter, Report DESY 98-071, 1998, [hep-ph/9806437].

[27] S. Frixione, G. Ridolfi, *Nucl. Phys.* **B 507** (1997) 315.

[28] R. Engel, *Z. Phys.* **C66** (1995) 203.

[29] M. Bengtsson, T. Sjöstrand, *Z. Phys.* **C 37** (1988) 465.

[30] L. Lönnblad, *Comp. Phys. Comm.* **71** (1992) 15.

[31] K. Charchula, G. A. Schuler, H. Spiesberger, *Comput. Phys. Commun.* **81** (1994) 381.

[32] T. Carli, Renormalization scale dependencies in dijet production at HERA, 1998, hep-ph/9906541.

[33] D. E. Soper, Basics of QCD perturbation theory, 1996, hep-ph/9702203.

[34] G. Sterman, S. Weinberg, *Phys. Rev. Lett.* **39** (1977) 1436.

[35] W. Bartel et al., *Z. Phys.* **C33** (1986) 23.

[36] S. Catani, Y. L. Dokshitzer, M. H. Seymour, B. R. Webber, *Nucl. Phys.* **B406** (1993) 187.

[37] S. Catani, Y. L. Dokshitzer, B. R. Webber, *Phys. Lett.* **B285** (1992) 291.

[38] T. Sjostrand, *Comput. Phys. Commun.* **28** (1983) 229.

[39] S. Bethke et al., *Phys. Lett.* **B213** (1988) 235.

[40] S. Catani, Y. Dokshitzer, B. Webber, *Phys. Lett.* **B 285** (1992) 291.

[41] T. Sjostrand, *Phys. Lett.* **157B** (1985) 321.

[42] H. Jung, *Comp. Phys. Comm.* **86** (1995) 147.

[43] H1 Collaboration, T. Ahmed et al., Dijet Event Rates in Deep Inelastic Scattering at HERA, DESY 98-076 and hep-ex/9806029.

[44] M. Wobisch, T. Wengler, Hadronization corrections to jet cross-sections in deep inelastic scattering, 1998.

[45] R. Poeschl, Measurement of the Double Differential Dijet Rate in Deep Inelastic Scattering at HERA and Comparison to NLO QCD Calculations, pHD theses.

[46] E. Lobodzinska, phD Thesis , Measurement of the forward jet cross-section in the low-xB region at HERA as a signature of BFKL dynamics.

[47] H1 Collaboration, C. Adloff et al., *Nucl. Phys.* **B 538** (1999) 3, DESY 98-143.

[48] E. A. D. Wolf, P. V. Mechelen, (1998) .

[49] T. Carli, private communications 1997 (unpublished).

Appendix A

Di-jet event Rates

DESY 98-076
June 1998

ISSN 0418-9833

Di-jet Event Rates in Deep-Inelastic Scattering at HERA

H1 Collaboration

Abstract: Di-jet event rates have been measured for deep-inelastic scattering in the kinematic domain $5 \lesssim Q^2 \lesssim 100$ GeV^2 and $10^{-4} \lesssim x_{Bj} \lesssim 10^{-2}$, and for jet transverse momenta squared $p_t^{*2} \gtrsim Q^2$. The analysis is based on data collected with the H1 detector at HERA in 1994 corresponding to an integrated luminosity of about 2 pb^{-1}. Jets are defined using a cone algorithm in the photon-proton centre of mass system requiring jet transverse momenta of at least 5 GeV. The di-jet event rates are shown as a function of Q^2 and x_{Bj}. Leading order models of point-like interacting photons fail to describe the data. Models which add resolved interacting photons or which implement the colour dipole model give a good description of the di-jet event rate. This is also the case for next-to-leading order calculations including contributions from direct and resolved photons.

Submitted to the European Physical Journal

C. Adloff[35], S. Aid[13], M. Anderson[23], V. Andreev[26], B. Andrieu[29], V. Arkadov[36], C. Arndt[11], I. Ayyaz[30], A. Babaev[25], J. Bähr[36], J. Bán[18], P. Baranov[26], E. Barrelet[30], R. Barschke[11], W. Bartel[11], U. Bassler[30], M. Beck[14], H.-J. Behrend[11], C. Beier[16], A. Belousov[26], Ch. Berger[1], G. Bernardi[30], G. Bertrand-Coremans[4], R. Beyer[11], P. Biddulph[23], J.C. Bizot[28], K. Borras[8], V. Boudry[29], S. Bourov[25], A. Braemer[15], W. Braunschweig[1], V. Brisson[28], D.P. Brown[23], W. Brückner[14], P. Bruel[29], D. Bruncko[18], C. Brune[16], J. Bürger[11], F.W. Büsser[13], A. Buniatian[4], S. Burke[19], G. Buschhorn[27], D. Calvet[24], A.J. Campbell[11], T. Carli[27], M. Charlet[11], D. Clarke[5], B. Clerbaux[4], S. Cocks[20], J.G. Contreras[8], C. Cormack[20], J.A. Coughlan[5], M.-C. Cousinou[24], B.E. Cox[23], G. Cozzika[9], J. Cvach[31], J.B. Dainton[20], W.D. Dau[17], K. Daum[40], M. David[9], M. Davidsson[22], A. De Roeck[11], E.A. De Wolf[4], B. Delcourt[28], M. Dirkmann[8], P. Dixon[19], W. Dlugosz[7], K.T. Donovan[21], J.D. Dowell[3], A. Droutskoi[25], J. Ebert[35], T.R. Ebert[20], G. Eckerlin[11], V. Efremenko[25], S. Egli[38], R. Eichler[37], F. Eisele[15], E. Eisenhandler[21], E. Elsen[11], M. Erdmann[15], A.B. Fahr[13], L. Favart[28], A. Fedotov[25], R. Felst[11], J. Feltesse[9], J. Ferencei[18], F. Ferrarotto[33], K. Flamm[11], M. Fleischer[8], M. Flieser[27], G. Flügge[2], A. Fomenko[26], J. Formánek[32], J.M. Foster[23], G. Franke[11], E. Gabathuler[20], K. Gabathuler[34], F. Gaede[27], J. Garvey[3], J. Gayler[11], M. Gebauer[36], R. Gerhards[11], A. Glazov[36], L. Goerlich[6], N. Gogitidze[26], M. Goldberg[30], I. Gorelov[25], C. Grab[37], H. Grässler[2], T. Greenshaw[20], R.K. Griffiths[21], G. Grindhammer[27], A. Gruber[27], C. Gruber[17], T. Hadig[1], D. Haidt[11], L. Hajduk[6], T. Haller[14], M. Hampel[1], W.J. Haynes[5], B. Heinemann[11], G. Heinzelmann[13], R.C.W. Henderson[19], S. Hengstmann[38], H. Henschel[36], R. Heremans[4], I. Herynek[31], K. Hewitt[3], K.H. Hiller[36], C.D. Hilton[23], J. Hladký[31], M. Höppner[8], D. Hoffmann[11], T. Holtom[20], R. Horisberger[34], V.L. Hudgson[3], M. Hütte[8], M. Ibbotson[23], Ç. İşsever[8], H. Itterbeck[1], M. Jacquet[28], M. Jaffre[28], J. Janoth[16], D.M. Jansen[14], L. Jönsson[22], D.P. Johnson[4], H. Jung[22], P.I.P. Kalmus[21], M. Kander[11], D. Kant[21], M. Karlsson[22], U. Kathage[17], J. Katzy[15], H.H. Kaufmann[36], O. Kaufmann[15], M. Kausch[11], S. Kazarian[11], I.R. Kenyon[3], S. Kermiche[24], C. Keuker[1], C. Kiesling[27], M. Klein[36], C. Kleinwort[11], G. Knies[11], J.H. Köhne[27], H. Kolanoski[39], S.D. Kolya[23], V. Korbel[11], P. Kostka[36], S.K. Kotelnikov[26], T. Krämerkämper[8], M.W. Krasny[6,30], H. Krehbiel[11], D. Krücker[27], A. Küpper[35], H. Küster[22], M. Kuhlen[27], T. Kurča[36], B. Laforge[9], R. Lahmann[11], M.P.J. Landon[21], W. Lange[36], U. Langenegger[37], A. Lebedev[26], F. Lehner[11], V. Lemaitre[11], S. Levonian[29], M. Lindstroem[22], J. Lipinski[11], B. List[11], G. Lobo[28], G.C. Lopez[12], V. Lubimov[25], D. Lüke[8,11], L. Lytkin[14], N. Magnussen[35], H. Mahlke-Krüger[11], E. Malinovski[26], R. Maraček[18], P. Marage[4], J. Marks[15], R. Marshall[23], J. Martens[35], G. Martin[13], R. Martin[20], H.-U. Martyn[1], J. Martyniak[6], S.J. Maxfield[20], S.J. McMahon[20], A. Mehta[5], K. Meier[16], P. Merkel[11], F. Metlica[14], A. Meyer[13], A. Meyer[11], H. Meyer[35], J. Meyer[11], P.-O. Meyer[2], A. Migliori[29], S. Mikocki[6], D. Milstead[20], J. Moeck[27], F. Moreau[29], J.V. Morris[5],

E. Mroczko[6], D. Müller[38], K. Müller[11], P. Murín[18], V. Nagovizin[25], R. Nahnhauer[36], B. Naroska[13], Th. Naumann[36], I. Négri[24], P.R. Newman[3], D. Newton[19], H.K. Nguyen[30], T.C. Nicholls[3], F. Niebergall[13], C. Niebuhr[11], Ch. Niedzballa[1], H. Niggli[37], G. Nowak[6], T. Nunnemann[14], H. Oberlack[27], J.E. Olsson[11], D. Ozerov[25], P. Palmen[2], E. Panaro[11], A. Panitch[4], C. Pascaud[28], S. Passaggio[37], G.D. Patel[20], H. Pawletta[2], E. Peppel[36], E. Perez[9], J.P. Phillips[20], A. Pieuchot[24], D. Pitzl[37], R. Pöschl[8], G. Pope[7], B. Povh[14], K. Rabbertz[1], P. Reimer[31], H. Rick[8], S. Riess[13], E. Rizvi[11], P. Robmann[38], R. Roosen[4], K. Rosenbauer[1], A. Rostovtsev[30], F. Rouse[7], C. Royon[9], K. Rüter[27], S. Rusakov[26], K. Rybicki[6], D.P.C. Sankey[5], P. Schacht[27], J. Scheins[1], S. Schiek[11], S. Schleif[16], W. von Schlippe[21], D. Schmidt[35], G. Schmidt[11], L. Schoeffel[9], A. Schöning[11], V. Schröder[11], E. Schuhmann[27], H.-C. Schultz-Coulon[11], B. Schwab[15], F. Sefkow[38], A. Semenov[25], V. Shekelyan[11], I. Sheviakov[26], L.N. Shtarkov[26], G. Siegmon[17], U. Siewert[17], Y. Sirois[29], I.O. Skillicorn[10], T. Sloan[19], P. Smirnov[26], M. Smith[20], V. Solochenko[25], Y. Soloviev[26], A. Specka[29], J. Spiekermann[8], S. Spielman[29], H. Spitzer[13], F. Squinabol[28], P. Steffen[11], R. Steinberg[2], J. Steinhart[13], B. Stella[33], A. Stellberger[16], J. Stiewe[16], K. Stolze[36], U. Straumann[15], W. Struczinski[2], J.P. Sutton[3], M. Swart[16], S. Tapprogge[16], M. Taševský[32], V. Tchernyshov[25], S. Tchetchelnitski[25], J. Theissen[2], G. Thompson[21], P.D. Thompson[3], N. Tobien[11], R. Todenhagen[14], P. Truöl[38], J. Zálešák[32], G. Tsipolitis[37], J. Turnau[6], E. Tzamariudaki[11], P. Uelkes[2], A. Usik[26], S. Valkár[32], A. Valkárová[32], C. Vallée[24], P. Van Esch[4], P. Van Mechelen[4], D. Vandenplas[29], Y. Vazdik[26], P. Verrecchia[9], G. Villet[9], K. Wacker[8], A. Wagener[2], M. Wagener[34], R. Wallny[15], T. Walter[38], B. Waugh[23], G. Weber[13], M. Weber[16], D. Wegener[8], A. Wegner[27], T. Wengler[15], M. Werner[15], L.R. West[3], S. Wiesand[35], T. Wilksen[11], S. Willard[7], M. Winde[36], G.-G. Winter[11], C. Wittek[13], M. Wobisch[2], H. Wollatz[11], E. Wünsch[11], J. Žáček[32], D. Zarbock[12], Z. Zhang[28], A. Zhokin[25], P. Zini[30], F. Zomer[28], J. Zsembery[9], and M. zurNedden[38],

[1] I. Physikalisches Institut der RWTH, Aachen, Germany[a]
[2] III. Physikalisches Institut der RWTH, Aachen, Germany[a]
[3] School of Physics and Space Research, University of Birmingham, Birmingham, UK[b]
[4] Inter-University Institute for High Energies ULB-VUB, Brussels; Universitaire Instelling Antwerpen, Wilrijk; Belgium[c]
[5] Rutherford Appleton Laboratory, Chilton, Didcot, UK[b]
[6] Institute for Nuclear Physics, Cracow, Poland[d]
[7] Physics Department and IIRPA, University of California, Davis, California, USA[e]
[8] Institut für Physik, Universität Dortmund, Dortmund, Germany[a]
[9] DSM/DAPNIA, CEA/Saclay, Gif-sur-Yvette, France
[10] Department of Physics and Astronomy, University of Glasgow, Glasgow, UK[b]

[11] DESY, Hamburg, Germany[a]
[12] I. Institut für Experimentalphysik, Universität Hamburg, Hamburg, Germany[a]
[13] II. Institut für Experimentalphysik, Universität Hamburg, Hamburg, Germany[a]
[14] Max-Planck-Institut für Kernphysik, Heidelberg, Germany[a]
[15] Physikalisches Institut, Universität Heidelberg, Heidelberg, Germany[a]
[16] Institut für Hochenergiephysik, Universität Heidelberg, Heidelberg, Germany[a]
[17] Institut für Reine und Angewandte Kernphysik, Universität Kiel, Kiel, Germany[a]
[18] Institute of Experimental Physics, Slovak Academy of Sciences, Košice, Slovak Republic[f,j]
[19] School of Physics and Chemistry, University of Lancaster, Lancaster, UK[b]
[20] Department of Physics, University of Liverpool, Liverpool, UK[b]
[21] Queen Mary and Westfield College, London, UK[b]
[22] Physics Department, University of Lund, Lund, Sweden[g]
[23] Physics Department, University of Manchester, Manchester, UK[b]
[24] CPPM, Université d'Aix-Marseille II, IN2P3-CNRS, Marseille, France
[25] Institute for Theoretical and Experimental Physics, Moscow, Russia
[26] Lebedev Physical Institute, Moscow, Russia[f,k]
[27] Max-Planck-Institut für Physik, München, Germany[a]
[28] LAL, Université de Paris-Sud, IN2P3-CNRS, Orsay, France
[29] LPNHE, Ecole Polytechnique, IN2P3-CNRS, Palaiseau, France
[30] LPNHE, Universités Paris VI and VII, IN2P3-CNRS, Paris, France
[31] Institute of Physics, Czech Academy of Sciences of the Czech Republic, Praha, Czech Republic[f,h]
[32] Nuclear Center, Charles University, Praha, Czech Republic[f,h]
[33] INFN Roma 1 and Dipartimento di Fisica, Università Roma 3, Roma, Italy
[34] Paul Scherrer Institut, Villigen, Switzerland
[35] Fachbereich Physik, Bergische Universität Gesamthochschule Wuppertal, Wuppertal, Germany[a]
[36] DESY, Institut für Hochenergiephysik, Zeuthen, Germany[a]
[37] Institut für Teilchenphysik, ETH, Zürich, Switzerland[i]
[38] Physik-Institut der Universität Zürich, Zürich, Switzerland[i]
[39] Institut für Physik, Humboldt-Universität, Berlin, Germany[a]
[40] Rechenzentrum, Bergische Universität Gesamthochschule Wuppertal, Wuppertal, Germany[a]

[a] Supported by the Bundesministerium für Bildung, Wissenschaft, Forschung und Technologie, FRG, under contract numbers 7AC17P, 7AC47P, 7DO55P, 7HH17I, 7HH27P, 7HD17P, 7HD27P, 7KI17I, 6MP17I and 7WT87P
[b] Supported by the UK Particle Physics and Astronomy Research Council,

and formerly by the UK Science and Engineering Research Council
[c] Supported by FNRS-NFWO, IISN-IIKW
[d] Partially supported by the Polish State Committee for Scientific Research, grant no. 115/E-343/SPUB/P03/002/97 and grant no. 2P03B 055 13
[e] Supported in part by US DOE grant DE F603 91ER40674
[f] Supported by the Deutsche Forschungsgemeinschaft
[g] Supported by the Swedish Natural Science Research Council
[h] Supported by GA ČR grant no. 202/96/0214, GA AV ČR grant no. A1010619 and GA UK grant no. 177
[i] Supported by the Swiss National Science Foundation
[j] Supported by VEGA SR grant no. 2/1325/96
[k] Supported by Russian Foundation for Basic Researches grant no. 96-02-00019

A.1 Introduction

The study of jets in deep-inelastic lepton-proton scattering (DIS) provides a testing ground for perturbative QCD. Partons emerging from the scattering process manifest themselves as jets of collimated hadrons which are observable in the experiment.

In the naive quark parton model, the virtual photon is absorbed by a single quark (antiquark) of the proton resulting in one jet from the struck quark and one from the proton remnant. Both jets have no transverse momentum in the photon-proton centre of mass frame (cms), when neglecting the intrinsic motion of the partons inside the proton. To first order in α_s, the leading order (LO) for di-jet production, two jets with balanced transverse momenta in the photon-proton cms are produced in the hard scattering process, in addition to the proton remnant jet. The hard scattering can either be the quark initiated QCD-Compton (QCDC) or the gluon initiated photon-gluon fusion (BGF) process.

In this analysis we present a measurement of the fraction R_2 of di-jet events in all DIS events, referred to as the di-jet rate. It is presented as a function of the Bjorken scaling variable x_{Bj}, integrated over the virtuality of the exchanged photon Q^2, and of Q^2, integrated over x_{Bj}. Jets are defined using a cone algorithm in the photon-proton cms requiring jet transverse momenta of at least 5 GeV. The measured jet rates are corrected for detector effects.

Previous measurements of jet rates at HERA [1] used the JADE jet algorithm at photon virtualities Q^2 large compared to the squared jet transverse momenta p_t^{*2}.[1] The present analysis probes a region of jet phase space characterized by jet transverse momenta squared of similar size or larger than the photon virtuality, $p_t^{*2}/Q^2 \gtrsim 1$. It has significantly better precision and has its emphasis on higher Q^2 compared to a previous study of single inclusive jet production [2]. There the data were found to be in good agreement with LO QCD models which included a resolved partonic structure of the virtual photon that evolves with Q^2.

In this study we investigate whether the di-jet rate can be described by LO QCD models with just point-like (direct) interactions of the virtual photon and with models with additional contributions from resolved photons, which may be considered as an effective description of higher order QCD effects. We also consider the colour dipole model. Finally our measurements are compared to next-to-leading order (NLO) QCD calculations which include either only direct or direct and resolved virtual photons.

The measurement was performed using data taken in 1994 with the H1 detector at the HERA storage ring, where 27.5 GeV positrons were collided with 820 GeV protons.

[1] Variables measured in the photon-proton cms are marked by a *. The positive z direction is defined to be along the incident proton direction.

A.2 The H1 Detector

A detailed description of the H1 apparatus is given elsewhere [3]. The parts of the detector which are essential for this measurement are the liquid argon (LAr) calorimeter [4], the backward lead-scintillator calorimeter (BEMC) [5], and the tracking chamber system.

The energy of the scattered positron is measured in the BEMC which covers the range in polar angle[2], θ, from 151° to 176°. It consists of stacks of lead and scintillator plates with a total of 21.7 radiation lengths. The BEMC is laterally segmented into square modules of $16 \times 16\,\mathrm{cm}^2$, with smaller modules at the inner and outer radii. The scintillation light is read out with photodiodes via wave length shifters along two opposite sides of each module. The absolute energy scale was determined to a precision of 1% [6]. The energy resolution is given by $\sigma_E/E = 39\%/E \oplus 10\%/\sqrt{E} \oplus 1.7\%$ (E in GeV) [5].

A cluster energy deposition exceeding a threshold of $\approx$ 7 GeV in the BEMC was the primary trigger condition for events used in this analysis.

The position of the scattered positron is measured with the backward proportional chamber (BPC) located in front of the BEMC covering the angular range $155° < \theta < 174.5°$. The BPC consists of four layers of wires strung vertically, horizontally, and at $\pm 45°$. The position resolution is $\sigma_{x,y} = 1.5\,\mathrm{mm}$.

Hadronic energy is detected in the highly segmented ($\approx$ 45000 channels) LAr calorimeter which extends from $4° < \theta < 154°$. The depth of the LAr calorimeter varies between 4.5 and 8 hadronic interaction lengths in the region $4° < \theta < 128°$. The uncertainty of the energy scale for hadrons is 4%. The hadronic energy resolution is $\sigma_E/E = 50\%/\sqrt{E} \oplus 2\%$ (E in GeV), as measured with test beams [7].

Charged tracks in the central region ($25° < \theta < 155°$) are measured with the central drift chamber system. Two jet chambers with wires in the z-direction allow measurements of track positions in the r-ϕ-plane to a precision of $\sigma_{r\phi} = 170\,\mu\mathrm{m}$. The z coordinate is measured to a precision of $\sigma_z = 320\,\mu\mathrm{m}$ using drift chambers with wires forming approximate circles around the beam. The momentum resolution is $\sigma_{p_t}/p_t^2 < 1\%\ \mathrm{GeV}^{-1}$.

The forward tracking detector covers $7° < \theta < 25°$ and consists of drift chambers with alternating planes of parallel wires and others with wires in the radial direction. It allows the measurement of track segments to a precision of $\sigma_{x,y} \leq 200\,\mu\mathrm{m}$.

Two electromagnetic calorimeters located downstream in the positron beam direction measure positrons and photons from the bremsstrahlung process $ep \to ep\gamma$ for the purpose of luminosity determination.

[2]The polar angle θ is defined with respect to the positive z-axis, the proton beam direction.

A.3 Data Selection

The data sample used for the present analysis corresponds to an integrated luminosity of 1.97 pb^{-1} taken during the 1994 run period. The phase space region of DIS events considered in this analysis is defined as follows:

$$\begin{aligned} 156^\circ < \quad \theta_e \quad &< 173^\circ \\ E' \quad &> 11\,\mathrm{GeV} \\ y \quad &> 0.05 \end{aligned} \tag{A.1}$$

Here, θ_e is the polar angle of the scattered positron and E' is its energy. The variables x_{Bj}, Q^2 and y (the inelasticity variable) are all determined from the 4-vector of the scattered positron. This selection ensures that the scattered positron is well inside the acceptance region of the BEMC, that the trigger efficiency is high, that the kinematic variables are well reconstructed, and that photoproduction background and radiative corrections are small. Photoproduction events, where the scattered positron is not detected in the backward direction, form a background if a particle from the hadronic final state entering the BEMC is misidentified as the scattered positron.

Additional cuts are applied for the identification of the scattered positron and to further suppress the influence of QED radiation and photoproduction background [6, 8]:

- The event must have a reconstructed vertex with a z position within $\pm 30\,\mathrm{cm}$ of the nominal position.
- The candidate positron shower is required to have a small lateral spread by applying the cut $r_{\mathrm{clust}} < 5\,\mathrm{cm}$, where r_{clust} is the energy-weighted mean transverse distance from the shower centre of gravity of each energy deposition sampled by the photodiodes.
- There must be a BPC signal within 5 cm of the straight line connecting the shower centre with the event vertex.
- The quantity $\sum_i (E_i - p_{z,i})$, where the sum is over all calorimeter energy depositions in the final state, is expected to be equal to twice the positron beam energy. An undetected positron in a photoproduction event or initial state photon radiation will decrease the value of this observable. For this analysis, $35 < \sum_i (E_i - p_{z,i}) < 70\,\mathrm{GeV}$ is required.

A.4 Jet Reconstruction and Selection

Jets are reconstructed using clusters of energy [3] measured in the LAr calorimeter. Cluster energies are corrected for the difference in response to hadronic and electromagnetic energy deposition and for losses due to dead

material and cracks. The cluster energy and the direction from the interaction point to the cluster centre are used to construct a massless four-vector.

The calorimetric energy measurement can be improved for low energy particles by using in addition to the energy the measured momentum of each charged particle track. To avoid double counting of energy each track was allowed to contribute at most 300 MeV. The value of 300 MeV was found to be optimal for reconstructing the transverse momenta of jets in simulated events [8].

Jets are defined in this analysis using a cone algorithm [9]. A cone is defined by a circular area of radius R in the $\eta^* - \phi^*$ plane, where η^* and ϕ^* are the pseudo-rapidity[3] and azimuthal angle in the photon-proton cms. A jet candidate consists of all objects (clusters and tracks) whose massless four vectors fall inside a cone. The jet transverse momentum $p^*_{t,\mathrm{jet}}$ is calculated as the scalar sum of the transverse momenta p^*_t of the jet objects. The jet η^* and ϕ^* (jet direction) are calculated as the p^*_t-weighted averages of the η^* and ϕ^* of the objects. This way of calculating the jet parameters is usually called the "p_t"-scheme [10]. An iterative procedure is used to find the jets of an event. Initially, every object in turn is used to define the cone centre of a candidate jet. The jet directions of the candidate jets[4] are then used as the cone centres for the next iteration. This is repeated until the resulting jet directions are identical to the cone centres. Then, also the midpoint in the $\eta^* - \phi^*$ plane of each pair of jets is considered as a candidate jet centre, and the procedure is repeated. Jets which have more than a fraction f of their $p^*_{t,\mathrm{jet}}$ contained in a higher transverse momentum jet are discarded. Finally, $p^*_{t,\mathrm{jet}}$ is required to exceed a minimum value $p^*_{t,\mathrm{min}}$.

In this analysis, the following parameters were chosen:

$$R = 1, \quad p^*_{t,\mathrm{min}} = 5\,\mathrm{GeV}, \quad \text{and } f = 0.75. \tag{A.2}$$

Exactly two jets per event fulfilling these criteria are demanded. In addition, the pseudo-rapidity difference $\Delta\eta^*$ of the two jets is required to be in the range

$$|\Delta\eta^*| < 2. \tag{A.3}$$

In leading order this cut is equivalent to requiring $|\cos\hat{\theta}| < 0.76$, where $\hat{\theta}$ is the polar angle between the emerging and incoming partons in the parton-parton or gamma-parton cms. It separates the jets from the proton remnant. The resolution in jet transverse momentum $\Delta p^*_t/p^*_t$ is approximately 20% at $p^*_t \sim 5$ GeV.

The number of di-jet events found is 4 957 while the total number of DIS events selected amounts to 112 806. To obtain the di-jet rate R_2, the number of di-jet events is divided by the total number of events in the same region of x_{Bj} and Q^2. R_2 is measured in bins of x_{Bj}, integrated over Q^2, and in bins of Q^2, integrated over x_{Bj}.

[3]The pseudo-rapidity η^* is given by $-\ln\tan(\theta^*/2)$.

[4]Several initial cone centres may result in the same candidate jet.

A.5 Data Correction

The residual background from photoproduction processes was determined using the PHOJET Monte Carlo (MC) generator [11] and was separately subtracted from the total number of events and the di-jet events as a function of Q^2 and x_{Bj}. This generator has been proven to give a good description of photoproduction background [6]. The correction for this background as well as the other corrections described below were obtained using MC events which were processed by the H1 detector simulation, reconstruction, and analysis chain. The largest subtraction of the photoproduction background occurs in the lowest x_{Bj} and Q^2 bins, where it amounts to 14% and 9% of the total event sample respectively, and to 3% and 1% of the di-jet sample. It is below 5% in the total sample and negligible in the di-jet sample in all other bins. For the di-jet rate, the correction is only significant in the lowest x_{Bj} and Q^2 bins where it increases the rate by $\approx 10\%$.

Radiation of photons from the incoming or outgoing positron leads to values of x_{Bj}, Q^2, and y, as determined from the scattered positron, which differ from the true kinematics of the photon-proton interaction.[5] These effects are different for the total and the di-jet sample. They were corrected using the DJANGO MC generator [12]. The correction factor on the di-jet rate was found to be 1.08, independent of x_{Bj} and Q^2.

The correction of the di-jet rate for detector acceptance and efficiencies was performed with two MC models, LEPTO [13] and ARIADNE [14], which will be discussed in section 7. They were used with two sets of parton density parameterizations, MRS-H [15] and GRV-94 HO [16] as implemented in PDFLIB [17]. The average prediction of these models was used to obtain bin-wise correction factors $c = \mathrm{R}_2^{\mathrm{MC,hadrons}}/\mathrm{R}_2^{\mathrm{MC,recon.}}$ for the di-jet rate R_2. This procedure is justified since the observables of the jet events, which are sensitive to detector effects, are well described by the Monte Carlo simulations. Critical observables in this sense are the energy flow within and around the jets, the η^* and p_t^* distribution of the two jets and the pseudo-rapidity difference $|\Delta\eta^*|$ between them.

Fig. A.1 shows a comparison of the experimental distributions with the two MC models. Only the curves obtained with the MRS-H parton density are shown, the curves with GRV-94 HO are very similar. There is good agreement between data and simulated events except for the η^* distribution of the jets. On top of the bin-wise correction, which ignores this small discrepancy, an additional correction for this effect was applied [8]. It takes into account the fact that on average the η^* of the jets for data is higher than for MC which leads to an overestimation of the correction factors c, as the jet reconstruction efficiency depends on η^*. This correction reduces R_2 by 10% in the lowest and by 1% in the uppermost bins of Q^2 and x_{Bj}. The combined

[5] In the outgoing positron case, this only applies if the angle between the radiated photon and the outgoing positron is large.

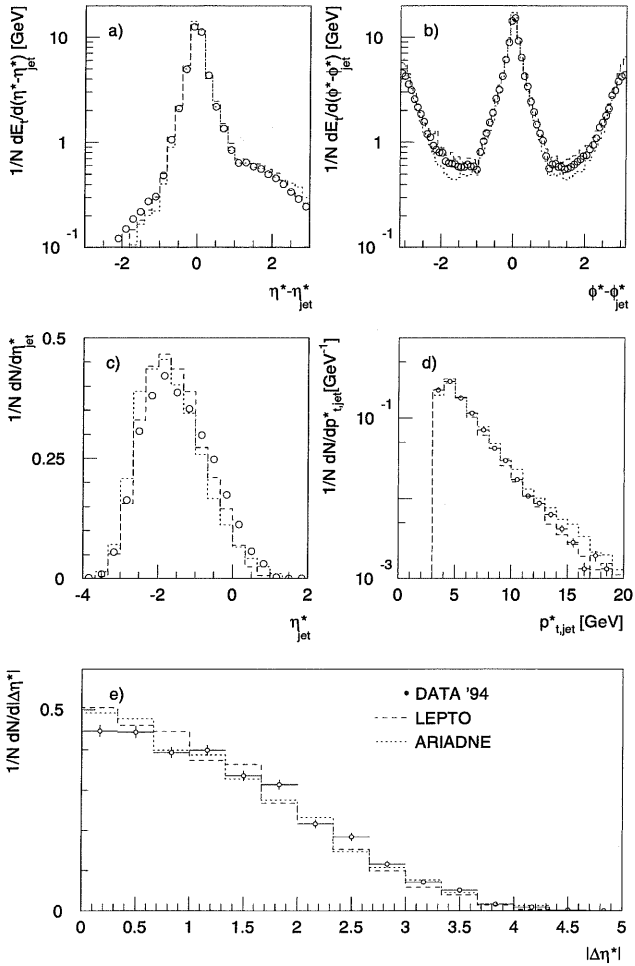

Figure A.1: *Transverse energy flow with respect to the jet axis, a) versus* $\eta^* - \eta^*_{\rm jet}$ *in a slice defined by* $|\phi^* - \phi^*_{\rm jet}| < 1$, *b) versus* $\phi^* - \phi^*_{\rm jet}$ *in a slice defined by* $|\eta^* - \eta^*_{\rm jet}| < 1$. *In the Figs. c) and d) the* η^* *and* p^*_t *spectra of the jets are shown. In Fig. e) the* $|\Delta\eta^*|$ *distribution is displayed. Points denote data, the histograms indicate the distributions obtained from LEPTO (dashed) and ARIADNE (dotted). The curves are normalized to the number N of entries; there are two entries per di-jet event in Figs. a)–d) and one in Fig. e). For Fig. d),* $p^*_{t,\rm min}$ *(Eqn. A.2) was lowered to 3.5 GeV and for Fig. e), the cut on* $|\Delta\eta^*|$ *(Eqn. A.3) was omitted.*

correction factors vary between 1.0 for low x_{Bj} and Q^2 values and 1.2 for high values.

A.6 Systematic Errors

Several sources of systematic uncertainties were investigated. A change in the hadronic energy scale of the LAr calorimeter by its estimated precision of $\pm 4\%$ results in a global change of the di-jet rates by $^{+9\%}_{-7\%}$. The correction for radiative effects has a global uncertainty of $\pm 3\%$ based on Monte Carlo statistics. These two errors were added in quadrature to give an overall systematic error of $^{+10\%}_{-8\%}$.

Changing the energy scale of the positron measurement in the BEMC within its $\pm 1\%$ uncertainty results in a change of R_2 by $\pm 2\%$ in all Q^2 bins. In the x_{Bj} bins, the change varies between $\pm 1\%$ for the lowest and $\pm 9\%$ for the highest bin. The systematic errors on the corrections for acceptance and efficiency were obtained by using the maximal variation of the correction factor for any particular model compared to the mean in each bin. They are of the order of 10%. The additional corrections for the difference in the mean values of η^* between experiment and simulation have a systematic error of the order of 2%. These errors were added in quadrature to give a bin by bin systematic error. It varies between 5% and 19%.

A.7 QCD Calculation of Di-jet Rates

Scattering processes involving the production of high p_T partons (hard scattering processes) are expected to be well described by perturbative QCD. In this analysis hard collisions are selected by requiring two jets with transverse momentum above 5 GeV. We consider three different QCD inspired models labeled DIR (direct), DIR+RES (direct + resolved), CDM (colour dipole model), and NLO QCD calculations at the parton level for comparison with experimental data. We briefly describe their most important features.

DIR: The LO QCD matrix elements (BGF and QCDC) are convoluted with the parton densities in the proton. Only direct interactions of the photon are considered as indicated in Fig. A.2a. For this model we have used the LEPTO [13] and RAPGAP [18] MC programs. The latter has been used without generating diffractive (rapidity gap) processes. RAPGAP and LEPTO give results consistent with each other to better than 10%.

DIR+RES: In addition to the direct contribution discussed above, a contribution from quarks and gluons inside the photon is considered, as shown in Fig. A.2b. This resolved photon contribution is assumed to

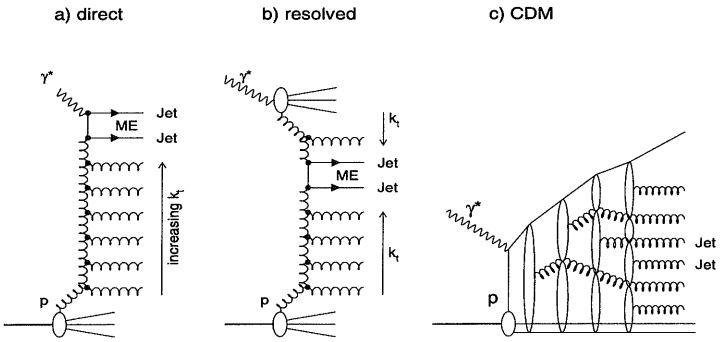

Figure A.2: *Generic diagrams of initial state parton emission in ep scattering (a,b). In the direct process (a) the hardest emission given by the QCD matrix element occurs at the top of the ladder. Emissions down the ladder are ordered with decreasing transverse momenta k_t. In the resolved process (b) the hardest emission given by the QCD matrix element may occur anywhere in the ladder with increasingly soft emissions along the ladder towards the proton and the photon. In the colour dipole model (c) gluon emissions are not ordered in transverse momentum k_t.*

set in only for scales of the hard subprocess $\gtrsim Q^2$. For the virtual photon parton densities the SaS-1D parameterization [19] was used. For this set of parton densities, the scale of the onset of the anomalous contribution in the virtual photon $P_0^2 = \max(Q_0^2, Q^2)$ was chosen, where $Q_0^2 = 0.36$ GeV^2 is the starting point of the Q^2 evolution[6]. The LO resolved photon contribution is implemented in the RAPGAP program. The contribution from longitudinal virtual photons is neglected.

In both the DIR and DIR+RES models we have used for the renormalization and factorization scale $\mu^2 = Q^2 + p_t^2$ as it provides a smooth transition between the DIS and photoproduction regimes. Additional emissions in the initial and final state are generated by parton showers [20] in the leading log DGLAP [21] approximation. In this approximation the radiated partons in the initial state are strongly ordered in transverse momentum k_t[7], with the hardest emission in the ladder occurring next to the hard matrix element (Figs. A.2a and A.2b).

CDM: In the colour dipole model [22], as implemented in the MC generator ARIADNE [14], gluon emission originates from a colour dipole stretched between the scattered quark and the proton remnant. Each emission of a gluon leads to two dipoles which may radiate further, generating a cascade of independently radiating dipoles (Fig. A.2c). These gluons are not ordered in k_t. A similar feature is found in the BFKL [23] evolution scheme.

The colour charge of the proton remnant (a di-quark in the simplest case) is assumed not to be point-like, leading to a phenomenological suppression of gluon radiation [14] in the direction of the remnant. This suppression occurs for hard gluons with wavelengths smaller than the size of the remnant. In addition, the colour charge of the scattered quark is taken to be extended, depending on the virtuality Q^2 of the photon (photon size suppression). This in turn leads to a suppression of radiation in the direction of the scattered quark [14, 24].

The QCDC component of the di-jet rate depends in the CDM model on the size of the colour charge while for the DIR model it depends on the parton densities of the proton. At low x_{Bj} this results in a considerably enhanced di-jet rate for CDM compared to DIR [25]. The photon-gluon fusion process, which is not naturally described by the CDM, is treated similarly as in the DIR approach discussed above.

In the DIR, DIR+RES, and CDM models, hadronization was performed with the Lund string fragmentation scheme as implemented in JETSET [26].

[6] this corresponds to the SaSgam parameter IP2=2

[7] k_t is the transverse momentum relative to the proton and photon axis in the photon-proton cms.

NLO: Finally, we consider two calculations in next to leading order (NLO) in the strong coupling constant α_s as implemented in the Monte Carlo integration programs DISENT [27] and JETVIP [28]. These programs provide cross sections for partons rather than a full hadronic final state. DISENT takes the soft and collinear divergencies arising in any NLO QCD calculation into account by using the subtraction method while JETVIP relies on the phase space slicing method. Both DISENT and JETVIP calculate NLO cross sections assuming a direct interacting photon. In addition, JETVIP provides a consistent calculation in NLO of direct *and* resolved interacting photons using parameterizations of the virtual photon structure functions. For the latter, the SaS-1D parameterization [19] (transformed to $\overline{MS}$) was used. For both the DISENT and JETVIP calculations the factorization and renormalization scales were chosen to be $\mu^2 = Q^2 + 50$ GeV^2, where 50 GeV^2 represents a good estimate of the average transverse momentum squared of the jets in the hadronic cms for the selection described before.

For comparing the corrected di-jet rate with models and parton level calculations, we have used the CTEQ4M parameterization [29] of parton densities inside the proton with the corresponding $\Lambda^{(5)}_{\overline{MS}}$ of 202 MeV (different parton density parameterizations were used in the models used to correct for detector effects, c.f. section 5). The DIR, RES, and CDM models implement the one loop expression for the calculation of α_s and in the DISENT and JETVIP programs the two loop expression was used.

A.8 Results and Discussion

The di-jet rate R_2 is shown in Figs. A.3a and A.3b as a function of Q^2 and x_{Bj} respectively. The data have been corrected for detector effects to the hadron level. The results correspond to the phase space region defined by Eqs. A.1–A.3. The data show a jet rate rising with Q^2 and flat in x_{Bj} except for the highest x_{Bj}-value.

For reasons to be explained later, two further scenarios have been investigated, where in addition to our basic requirement of $p_t^* > 5$ GeV for each jet (symmetric scenario), we demand either at least 7 GeV for the jet with the highest p_t^* (asymmetric scenario) or at least 13 GeV for the sum of the absolute values of the jet transverse momenta (sum scenario). The results for R_2 for the asymmetric scenario are given in Figs. A.3c,d and for the sum scenario in Figs. A.3e,f. Table 1 in the appendix summarizes the di-jet rates for the three different scenarios.

A.8.1 Comparison of data with LO QCD models

The results for the three different selections of jet phase space are compared to predictions from MC models based on perturbative QCD (see previous

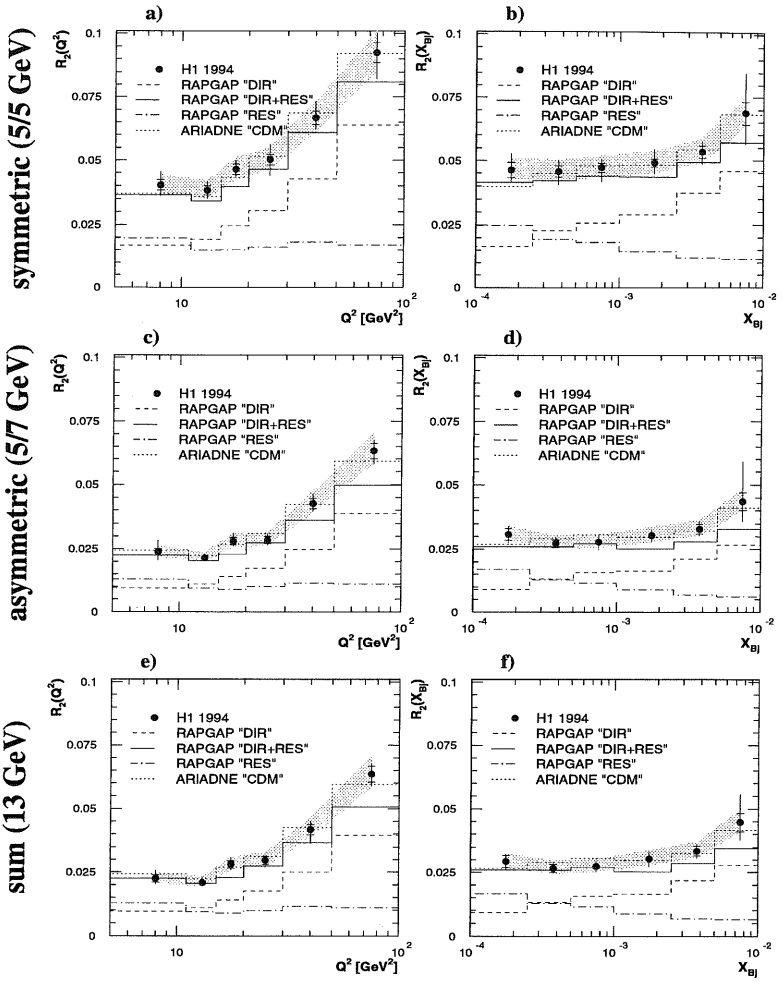

Figure A.3: *Di-jet rate* R_2 *as a function of* Q^2 *(a,c,e), integrated over* x_{Bj}*, and as a function of* x_{Bj} *(b,d,f), integrated over* Q^2 *for the symmetric (a,b), asymmetric (c,d), and sum (e,f) cut scenario on the* p_t^* *of the two jets. The data are corrected to the hadron level. The inner bars give the statistical errors, the full error bars include the bin by bin systematic errors. The grey band shows the overall systematic uncertainty due to the hadronic energy scale of the calorimeter and the uncertainty of the radiative correction. Also indicated are the predictions from MC models. Their statistical errors are smaller than the statistical errors of the data.*

section). The LO DIR model fails to describe the data as demonstrated in Figs. A.3a to A.3f with RAPGAP. In particular in the region of small Q^2 and x_{Bj} the DIR model underestimates the data by a factor 2–3.

Choosing $\mu^2 = Q^2$ for the hard scale does not change the results considerably. Using different parton density parameterizations (CTEQ4L, CTEQ4A4, CTEQ4HJ, MRSR1, and MRSR2) leads to variations in R_2 of up to 10% in the lowest and the highest Q^2 and x_{Bj} bins when compared to CTEQ4M, our default. The world average value of $\alpha_s(M_Z^2) = 0.118$ corresponds to $\Lambda^{(5)}_{\overline{MS}} = 209^{+39}_{-33}$ MeV [30], very close to the fit value of 202 MeV for CTEQ4M. With the CTEQ4M parton densities but with $\Lambda^{(5)}_{\overline{MS}} = 250$ MeV (an increase of about one standard deviation), R_2 increases by less than 10% in the lowest Q^2 and x_{Bj} bins.

We conclude that a LO matrix element calculation assuming only direct interactions of the virtual photon in combination with DGLAP parton showers as an approximation to higher order effects is not able to account for the observed di-jet rates.

Adding a significant contribution to the di-jet cross section from resolving the structure of the virtual photon, as predicted by the DIR+RES model as implemented in RAPGAP, gives a good description of the data. It should be noted, however, that considerable freedom exists in tuning the model to data, in particular by varying the choice of the hard scale, and the parton densities in the virtual photon.

The CDM model, as implemented in ARIADNE, is also able to describe the di-jet rate well, both in absolute value and in the Q^2 and x_{Bj} dependence. We used a parameter setting which had been tuned to give a good description of transverse energy flows and particle spectra [31]. Here too, it should be remarked that by varying the parameters for the proton and photon size suppression (see section 2) within sensible limits[8], the predictions of this model can be changed by up to 40% in the lowest bin and about 20% in the highest bin in Q^2 and x_{Bj}.

A.8.2 Comparison of data with NLO QCD calculations

We now investigate whether a NLO QCD calculation is able to describe the data. For this purpose we have used results from the programs DISENT and JETVIP [28]. For the calculation of R_2 for the direct or point-like coupling of the photon to the partons in the proton, the two programs agree to better than 5%. As mentioned in section 7, JETVIP can also calculate the direct and resolved photon contribution in NLO. Both programs provide parton level cross sections rather than a full hadronic final state. However, the DIR and CDM models suggest that the hadronization effects are small for jet transverse momenta above 5 GeV. The di-jet rate at the parton level was

[8]PARA(10) and PARA(15), default 1.0 [14]; we used 1.5 and 0.5 respectively and varied them independently between 0.5 and 1.5.

found to be for LEPTO (ARIADNE) typically 9% (20%) and not more than 12% (25%) higher than the rate at the hadron level.

Figs. 4a,b show the hadron level di-jet rate R_2 versus Q^2 and x_{Bj} for the asymmetric scenario, and in Figs. 4c,d for the sum scenario, compared to the NLO QCD calculation of the direct contribution (labeled DIR in the figures) by JETVIP and DISENT. Good agreement is observed between data and the direct NLO QCD calculation, except for the lowest Q^2 and x_{Bj} bin.

The sensitivity to variations of the parton density parameterizations is similar to the LO DIR case discussed above. Varying the factorization and renormalization scale μ^2 by factors of 4 results in cross section variations of less than 20%. Choosing $\mu^2 = Q^2$ as the scale enhances the cross section in the lowest x_{Bj} and Q^2 bins by up to 30%, improving the agreement with data. At the same time this introduces however a large sensitivity to scale variations (up to 50% and 65% in the lowest Q^2 and x_{Bj} bins). This indicates, as one might expect, that Q^2 is not the proper scale to use in a kinematic domain where $Q^2 \ll p_t^{*2}$.

The agreement with data at low x_{Bj} and Q^2 is improved when contributions from resolving the virtual photon structure are included in NLO (labeled DIR-PSP+RES in the figure). In order to avoid double counting in the full NLO QCD calculation it is necessary to subtract the contribution from the virtual photon splitting into $q\bar{q}$, where one of the quarks subsequently interacts with a parton from the proton to produce two high p_t jets, since this contribution is part of the parameterization of the virtual photon structure function [19]. We refer to this perturbatively calculated contribution from photon splitting as defined in [28] as PSP and the contribution from resolving the photon structure as RES.

Two interesting observations can be made. First, at large Q^2 the difference between the NLO direct part (DIR) and the full calculation (DIR-PSP+RES) is found to be rather small, which implies that the NLO resolved part (RES) is saturated by the contribution from virtual photon splitting (PSP). Second, the full NLO calculation is close to the LO RAPGAP DIR+RES prediction shown as the full line in Figs. 3c to 3f. This suggests, together with the first observation, that the large resolved contribution needed in LO to describe the data for the larger Q^2 bins is included in the NLO DIR cross section.

It should be noted that in NLO the RES contribution depends less on the choice of the hard scale and the parton densities in the virtual photon than in LO. This is due to the subtraction procedure and because it is a NLO calculation [28]. Of course the uncertainty due to the rather poorly known parton density of the virtual photon remains.

A comparison of the data on R_2 and the NLO QCD calculation for the symmetric scenario is not shown, because the calculation for this case is not reliable although the measurement is valid and infrared safe. The calculations from both DISENT and JETVIP underestimate the data and give different predictions. This can be understood as a feature of any fixed order calculation

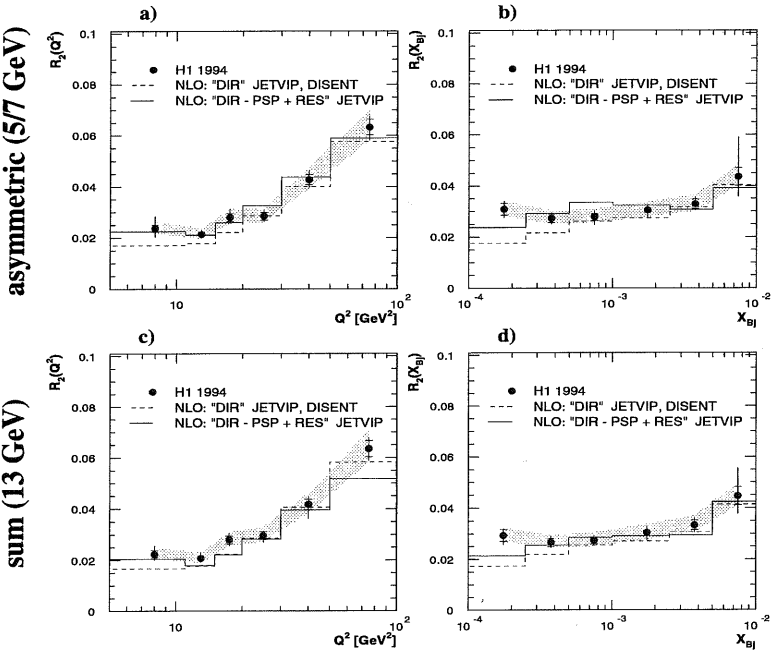

Figure A.4: *Di-jet rate* R_2 *as a function of* Q^2 *(a,c), integrated over* x_{Bj}*, and as a function of* x_{Bj} *(b,d), integrated over* Q^2*. The data (corrected to the hadron level) for the asymmetric (a,b) and the sum scenario (c,d) are compared to different NLO calculations (at the parton level). The data are the same as those shown in Figs. 3c to 3f. The statistical errors of the NLO calculations are smaller than the statistical errors of the data.*

which gives large negative cross sections in the phase space region where both jets have almost identical transverse momenta. The problem in the prediction of di-jet rates for symmetric cuts on the jet transverse momenta has been noted in the framework of the phase space slicing method [32] and discussed in detail for this and the subtraction method in [33]. A correct treatment of this phase space region would need a resummation to all orders [33, 34].

A.8.3 Event topology

The conclusions of the underlying picture derived above can be checked by a study of the event topology. In the DIR+RES model the hardest emission leading to the observed jets may occur anywhere in the ladder, as depicted in Fig. A.2b. In this case, additional hadronic activity is expected from the virtual photon "remnant" and additional parton emission from the top part of the ladder.

This activity is expected in the direction of the virtual photon which corresponds to the backward region of the detector. Similar hadronic activity in the backward region can also be expected from the CDM model due to the absence of k_t ordering between the photon and the proton vertex (see section 2). Both models predict a Q^2 dependence of this effect which increases as Q^2 approaches zero.

We define an observable which is sensitive to additional energy flow in the photon direction:

$$x_\gamma^{\text{obs}} = \frac{\sum_{\text{jets}} (E^* - p_z^*)}{\sum_{\text{had. final state}} (E^* - p_z^*)} \tag{A.4}$$

In the limit $Q^2 \to 0$ and in LO this corresponds to the fractional momentum of the parton from the photon entering the hard subprocess and giving rise to the observed jet system. In this picture $1 - x_\gamma^{\text{obs}}$ corresponds to the fractional energy of the photon remnant.

Fig. A.5a shows the uncorrected distribution of x_γ^{obs} for data in three different ranges of Q^2. The MC events which were used for comparison in Fig. A.5 have been subject to a detailed simulation of the H1 detector. In the data an increase at low x_γ^{obs} is noticed as Q^2 decreases. No such effect is seen for the DIR model as represented by RAPGAP (full line in Figs. A.5b to A.5d). The DIR+RES model of RAPGAP is able to give a reasonable description of both shape and Q^2 dependence (dashed line in Figs. A.5b to A.5d). The CDM model shows a similar Q^2 dependence but fails to describe the shape of the distribution (dotted line in Figs. A.5b to A.5d).

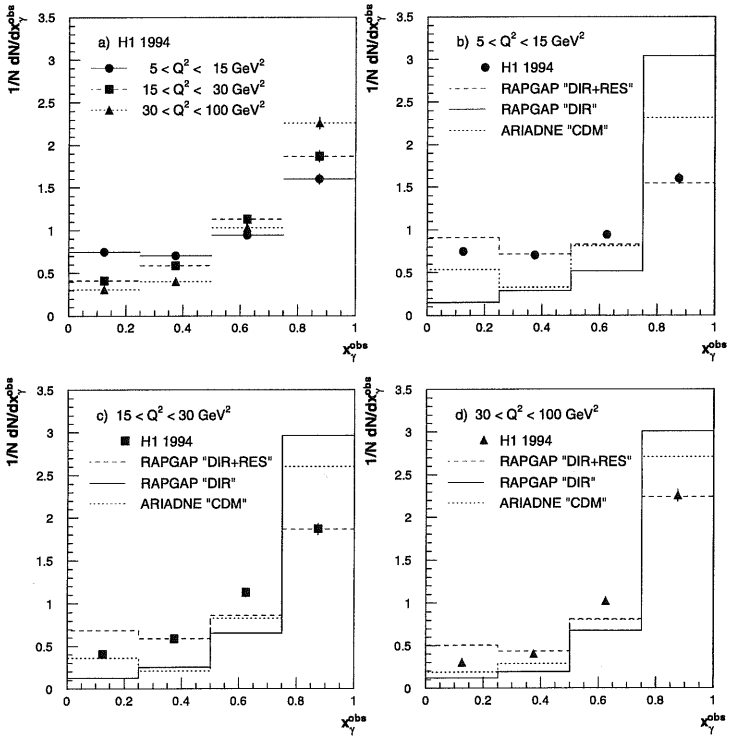

Figure A.5: *Uncorrected distribution of $x_\gamma^{\rm obs}$ in three different Q^2 bins (a). In b) to d) the data are compared for each bin in Q^2 to the DIR model and the DIR+RES model as given by RAPGAP, and the CDM model as implemented by ARIADNE. The figures are normalized to the number N of di-jet events. The error bars indicate the statistical error only.*

A.9 Conclusions

Di-jet event rates have been measured in deep-inelastic scattering at small x_{Bj} ($10^{-4} \lesssim x_{Bj} \lesssim 10^{-2}$) and moderate Q^2 ($5 \lesssim Q^2 \lesssim 100$ GeV^2). Three different scenarios of cuts on the transverse momenta of the jets have been investigated: the basic symmetric requirement ($p^*_{t,\min} \geq 5$ GeV for both jets), and additionally the asymmetric ($p^*_{t,\min} \geq 5$ and 7 GeV) and sum p^*_t ($\geq$ 13 GeV) requirements. The analysis was performed in the hadronic centre of mass frame. The data have been corrected for detector and QED radiative effects. This analysis probes a region in jet phase space of small x_{Bj} and jet transverse momenta squared of similar size or larger than the photon virtuality ($p^{*2}_t/Q^2 \gtrsim 1$).

Assuming a direct or point-like photon, leading order matrix element calculations in combination with parton showers as an approximation of higher order effects fail completely to describe the data.

Adding to the leading order model additional contributions from resolving the partons inside the virtual photon (RAPGAP) appear to give an effective description of higher order effects leading to good agreement with the data for all three scenarios. A similarly good agreement with the di-jet event rates is observed for the colour dipole model (ARIADNE) with its features of gluon emission.

Next-to-leading order calculations in α_s assuming a point-like virtual photon provide a good description of the data for the scenarios with the asymmetric and the sum p^*_t cut, except for the lowest bin in Q^2 and x_{Bj}. This is improved by a NLO calculation which also considers contributions from resolving virtual photon structure.

Acknowledgements

We are grateful to the HERA machine group whose outstanding efforts have made and continue to make this experiment possible. We thank the engineers and technicians for their work in constructing and now maintaining the H1 detector, our funding agencies for financial support, the DESY technical staff for continual assistance, and the DESY directorate for the hospitality which they extend to the non-DESY members of the collaboration. We gratefully acknowledge fruitful discussions with S. Frixione, G. Kramer, L. Lönnblad, B. Pötter, and J. Rathsman.

Appendix

	symmetric (5/5 GeV)			asymmetric (5/7 GeV)			sum (13 GeV)		
Q^2 [GeV^2]	R_2	σ_{stat}	σ_{syst}	R_2	σ_{stat}	σ_{syst}	R_2	σ_{stat}	σ_{syst}
5 – 11	0.040	±0.002	$^{+0.005}_{-0.004}$	0.024	±0.001	$^{+0.004}_{-0.003}$	0.022	±0.001	$^{+0.003}_{-0.002}$
11 – 15	0.038	±0.002	$^{+0.003}_{-0.002}$	0.021	±0.001	$^{+0.001}_{-0.001}$	0.021	±0.001	$^{+0.002}_{-0.001}$
15 – 20	0.046	±0.002	$^{+0.003}_{-0.002}$	0.028	±0.002	$^{+0.003}_{-0.001}$	0.028	±0.002	$^{+0.002}_{-0.002}$
20 – 30	0.050	±0.002	$^{+0.006}_{-0.006}$	0.028	±0.001	$^{+0.002}_{-0.002}$	0.030	±0.002	$^{+0.001}_{-0.002}$
30 – 50	0.067	±0.003	$^{+0.006}_{-0.004}$	0.043	±0.002	$^{+0.003}_{-0.002}$	0.042	±0.002	$^{+0.003}_{-0.005}$
50 – 100	0.093	±0.004	$^{+0.006}_{-0.010}$	0.063	±0.003	$^{+0.003}_{-0.004}$	0.063	±0.003	$^{+0.003}_{-0.003}$

	symmetric (5/5 GeV)			asymmetric (5/7 GeV)			sum (13 GeV)		
x_{Bj}	R_2	σ_{stat}	σ_{syst}	R_2	σ_{stat}	σ_{syst}	R_2	σ_{stat}	σ_{syst}
$10^{-4} - 2.5 \cdot 10^{-4}$	0.046	±0.003	$^{+0.006}_{-0.004}$	0.031	±0.002	$^{+0.002}_{-0.002}$	0.029	±0.002	$^{+0.001}_{-0.003}$
$2.5 \cdot 10^{-4} - 5.0 \cdot 10^{-4}$	0.046	±0.002	$^{+0.004}_{-0.005}$	0.027	±0.002	$^{+0.002}_{-0.001}$	0.027	±0.002	$^{+0.002}_{-0.001}$
$5.0 \cdot 10^{-4} - 10^{-3}$	0.047	±0.002	$^{+0.003}_{-0.005}$	0.028	±0.001	$^{+0.002}_{-0.003}$	0.027	±0.001	$^{+0.002}_{-0.002}$
$10^{-3} - 2.5 \cdot 10^{-3}$	0.049	±0.002	$^{+0.005}_{-0.004}$	0.030	±0.001	$^{+0.002}_{-0.002}$	0.030	±0.001	$^{+0.002}_{-0.003}$
$2.5 \cdot 10^{-3} - 5.0 \cdot 10^{-3}$	0.053	±0.002	$^{+0.003}_{-0.004}$	0.033	±0.002	$^{+0.002}_{-0.002}$	0.033	±0.002	$^{+0.002}_{-0.002}$
$5.0 \cdot 10^{-3} - 10^{-2}$	0.069	±0.005	$^{+0.016}_{-0.011}$	0.044	±0.003	$^{+0.015}_{-0.007}$	0.045	±0.004	$^{+0.010}_{-0.006}$

Table 1: *Di-jet rate in bins of Q^2 and x_{Bj}, and statistical and systematic errors for the symmetric, the asymmetric, and the sum cut scenario on the p_t^* of the two jets. The overall systematic error of $^{+10\%}_{-8\%}$ for the symmetric scenario and $^{+11\%}_{-8\%}$ for the asymmetric and sum scenario, arising from the uncertainty of the hadronic energy scale of the calorimeter and the uncertainty of the radiative QED corrections, is not included.*

Bibliography

[1] H1 Collaboration, I. Abt et al.,Z. Phys. C61 (1994) 59;
ZEUS Collaboration, M. Derrick et al., Z. Phys. C67 (1995) 81.

[2] H1 Collaboration, C. Adloff et al., Phys. Lett. B415 (1997) 418.

[3] H1 Collaboration, I. Abt et al., Nucl. Instr. and Meth. A386 (1997) 310 and 348.

[4] H1 Calorimeter Group, B. Andrieu et al., Nucl. Instr. and Meth. A336 (1993) 460.

[5] H1 BEMC Group, J. Ban et al., Nucl. Instr. and Meth. A372 (1996) 399.

[6] H1 Collaboration, S. Aid et al., Nucl. Phys. B470 (1996) 3.

[7] H1 Calorimeter Group, B. Andrieu et al., Nucl. Instr. and Meth. A336 (1993) 499.

[8] J. Spiekermann, Ph.D. Thesis, University of Dortmund (1997).

[9] M. H. Seymour, Z. Phys. C62 (1994), 127.

[10] M. H. Seymour, Nucl. Phys. B421 (1994) 545.

[11] R. Engel, Z. Phys. C 66 (1995) 203;
R. Engel and J. Ranft, Phys. Rev. D54 (1996) 4244.

[12] K. Charchula, G. A. Schuler, and H. Spiesberger, Comput. Phys. Commun. 81 (1994) 381.
We used the program version 6.2.

[13] G. Ingelman, in Proc. Workshop on Physics at HERA, Hamburg, October 1991, eds. W. Buchmüller and G. Ingelman, vol. 3 (1992) 1366;
G. Ingelman, A. Edin, J. Rathsman, Comput. Phys. Comm. 101 (1997) 108.
We used the program versions 6.4 and 6.5.

[14] L. Lönnblad, Comput. Phys. Comm. 71 (1992) 15;
L. Lönnblad, Z. Phys. C65 (1995) 285.
We used the program version 4.08.

[15] A.D. Martin, W.J. Stirling, and R.G. Roberts, in Proc. Workshop on Quantum Field Theory and Theoretical Aspects of High Energy Physics, Bad Frankenhausen, Germany, 1993, eds. B. Geyer and E.M. Ilgenfritz, (1993) 11.

[16] M. Glück, E. Reya, and A. Vogt, Z. Phys. C67 (1995) 433.

[17] H. Plothow-Besch, Int. J. Mod. Phys. A10 (1995) 2901.
We used the library version 7.09.

[18] H. Jung, Comput. Phys. Commun. 86 (1995) 147.
We used the program version 2.06.

[19] G. A. Schuler and T. Sjöstrand, Z. Phys. C68 (1995) 607, Phys. Lett. B376 (1996) 193.

[20] M. Bengtsson and T. Sjöstrand, Z. Phys. C37 (1988) 465.

[21] V. N. Gribov and L. N. Lipatov, Sov. J. Nucl. Phys. 15 (1972) 438;
G. Altarelli and G. Parisi, Nucl. Phys. B126 (1977) 298;
Yu. L. Dokshitzer, Sov. Phys. JETP 46 (1977) 641.

[22] G. Gustafson, Phys. Lett. B175 (1986) 453;
G. Gustafson and U. Petterson, Nucl. Phys. B306 (1988) 746;
B. Andersson, G. Gustafson, L. Lönnblad, and U. Petterson, Z. Phys. C43 (1989) 625.

[23] E. A. Kuraev, L. N. Lipatov, and V. S. Fadin, Sov. Phys. JETP 45 (1977) 199;
Ya. Ya. Balitsky and L. N. Lipatov, Sov. J. Nucl. Phys. 28 (1978) 822;
J. Bartels and H. Lotter, Phys. Lett. B309 (1993) 400.

[24] L. Lönnblad, M. H. Seymour, et al., Proc. Physics at LEP 2 Workshop, eds. G. Altarelli, T. Sjöstrand, and F. Zwirner, CERN/96-01, Vol. 2, (1996) 187.

[25] J. Rathsman, Phys. Lett. B393 (1997) 181.

[26] T. Sjöstrand, Comp. Phys. Comm. 82 (1994) 74;
T. Sjöstrand, Pythia 5.7 and Jetset 7.4 physics and manual, CERN-TH 7112/93, Dec. 1993 (revised Aug. 1994).

[27] S. Catani and M. H. Seymour, Acta Phys. Polon. B28 (1997) 863.

[28] B. Pötter, Report DESY 98–071, [hep-ph/9806437];
G. Kramer and B. Pötter, Report DESY 98–046, [hep-ph/9804352].
The numerical results were provided for us by B. Pötter.

[29] H. L. Lai et al., Phys. Rev. D55 (1997) 1280.

[30] R.M. Barnett et al., Phys. Rev. D54 (1996) 1.

[31] N. Brook et al., in Proc. Workshop on Future Physics at HERA, Hamburg, September 1996, eds. G. Ingelman, A. De Roeck, R. Klanner, vol. 1 (1996) 613.

[32] M. Klasen and G. Kramer, Phys. Lett. B366 (1996) 385.

[33] S. Frixione and G. Ridolfi, Nucl. Phys. B507 (1997) 315.

[34] S. Catani and B. Webber, JHEP 10 (1997) 005.

Appendix B

From k^2 to k_t ordering

To see how to get from ordering in k^2, to ordering in k_t, we look at a general $2 \rightarrow 2$ process, using the Mandelstam variables:

$$\begin{aligned} \hat{t} &= -x\hat{s} \\ \hat{u} &= (x-1)\hat{s} \end{aligned} \tag{B.1}$$

It can now be shown that the transverse momentum of the emitted parton can be written as [?]:

$$p_t^2 = \frac{\hat{s}\hat{t}\hat{u}}{(\hat{s}+Q^2)^2} \tag{B.2}$$

Requiring the incoming propagator parton to be on-shell, $Q^2 = 0$, we get:

$$p_t^2 = \frac{\hat{t}\hat{u}}{\hat{s}} = (1-x)(-t) = (1-x)|k^2| \tag{B.3}$$

If the incoming parton is on-shell ($m^2 = 0$), in a frame with, $m_t^2 = 0$, then this implies that, $k_t = -p_t$, and hence we get the desired relation:

$$k_t^2 = (1-x)|k^2| \tag{B.4}$$

Ordering in $|k^2|$ thus imply $|k_t|$ ordering (since $x > 0$), but not vice verse.

Appendix C

SPACAL fiducial cuts

Here are the regions, defined in the (x, y) plane of the SPACAL, that were either removed from the analysis, or rescaled in terms of the data, due to inefficiencies in the s0 sub-trigger.

The following regions were removed from the analysis:

```
      if (x.gt.-16.2.and.x.lt.8.1.and.y.gt.-8.1.and.y.lt.
     &       16.2) skipevt = 1

      if (x.lt.-20.5.and.x.gt.-25.0)
     &       .and.(y.lt.-33.0.and.y.gt.-37.5) skipevt = 1

      if  (x.gt.-16.25.and.x.lt.-12.5)
     &       .and.(y.gt.-21.0.and. y.lt.-16.0) skipevt = 1

      if  (x.lt.-25.5.and.x.gt.-31.5)
     &       .and.(y.lt. 39.1.and.y.gt. 33.1) skipevt = 1

      if  (x.lt.38.1.and.x.gt.27.0)
     &       .and.(y.lt.-27.0.and.y.gt.-38.0) skipevt = 1

      if (clx.lt.-46.1.and.x.gt.-48.0)
     &       .and.(y.lt.-25.0.and.y.gt.-28.0) skipevt = 1
```

In two run-ranges in 1997 the s0 suffered from inefficiencies. This was accounted for by rescaling the data [49] according to the below procedure:

```
     if (irun.ge.191339.and.irun.le.193780) then
       teffel = 1.
       if (atan2(y,x).gt.-1.4
     &       .and.atan2(y,x).lt.0.58) then
         teffel=0.85
```

```
      endif
      datweigh = datweigh*(1/teffel)
    endif


    if (irun.ge.195668 .and. irun.le.196360 ) then
      teffel=1.
      if((x.gt.-16.and.x.lt.7.5)
     &       .and.(y.gt.-16.and.y.lt.-7.5)  ) then
        teffel=0.75
      endif
      datweigh = datweigh*(1/teffel)
    endif
```